DIAGNOSTIC AND MODELING STUDIES OF CLIMATE VARIATIONS OVER WEST AFRICA AND NORTH AMERICA

A Dissertation

Presented to the Faculty of the Graduate School

of Cornell University

In Partial Fulfillment of the Requirements for the Degree of

Doctor of Philosophy

by

Bing Pu

January 2011

DIAGNOSTIC AND MODELING STUDIES OF CLIMATE VARIATIONS OVER WEST AFRICA AND NORTH AMERICA

Bing Pu, Ph. D.

Cornell University 2011

The West African westerly jet (WAWJ) is a low-level (~ 925 hPa) feature of the summer climatology that transports moisture from the eastern Atlantic onto the African continent at 8-11°N. Here the dynamics of the jet's formation and its role in Sahel precipitation variations are examined.

Horizontal momentum budgets analysis shows that the jet forms when a region of westerly acceleration is generated by the superposition of the Atlantic Intertropical Convergence Zone (ITCZ) and the westward extension of the continental thermal low, which is associated with the formation of an offshore low related to seasonal sea surface temperature (SST) warming at 6°-18°N along the coast.

Variations of the westerly jet are significantly positively correlated to precipitation variations over the Sahel (10°-20°N, 18°W-30°E) on both interannual and decadal time scales. In wet periods of 1958-1971 and 1988-2009 (dry period of 1972-1987), enhanced (decreased) westerly moisture fluxes associated with a strong (weak) jet increase (decrease) the low-level moisture content over the Sahel, decreasing (enhancing) the stability of the atmosphere.

While variations of the jet are closely associated with variations of the Atlantic marine ITCZ between 20°W and 30°W, regional model simulations suggest that decadal SST variations in the eastern Atlantic do not force the observed decadal variations in the jet.

Climate response over North America to a hypothetical shutdown of the Atlantic meridional overturning circulation in the context of global warming is investigated using a regional climate model.

The model predicates precipitation decreases in most of the United States and Mexico from April to September, except over the eastern U.S. where rainfall increases in April, May, June, and September.

Moisture budgets analysis shows that precipitation variations over the eastern and western U.S and Mexico are mainly due to changes in moisture convergence associated with large-scale circulation changes, e.g., the westward extension of the North Atlantic subtropical high and the formation of an anomalous high over the eastern Pacific and the Gulf of Mexico.

Variations in land surface temperature are dominated by greenhouse gas warming, which is magnified by local hydrological changes in the summer. More extreme warm temperatures and dry spells occur.

BIOGRAPHICAL SKETCH

Born in East China, Bing Pu completed her elementary and high school education in her hometown, Suzhou. From 2000-2004, Bing Pu pursed undergraduate studies in Information Management & Information System in the Department of Atmospheric Sciences at Nanjing University of Information Science and Technology (once named Nanjing Institution of Meteorology in 1960-2004). It was there that she developed an interest in Atmospheric Sciences.

In August 2004, Bing Pu was enrolled in a master's program in the Department of Atmospheric Sciences in Peking University. She worked with Professor Shaowu Wang and Professor Jinhong Zhu on climate variations over the eastern China. In July 2007, Bing Pu was graduated from Peking University with a M.S. degree in Meteorology.

In August 2007, Bing Pu began doctoral studies in Atmospheric Sciences at Cornell University, working with Professor Kerry H. Cook. During her two-year stay in Ithaca campus Bing Pu completed course requirements and passed Ph.D. Candidacy exam in May 2009. Bing Pu has been a visiting student at The University of Texas at Austin since July 2009, where she continues working with Professor Kerry H. Cook on climate dynamics.

ACKNOWLEDGMENTS

Invaluable instruction from my advisor, Professor Kerry H. Cook, is gratefully acknowledged and sincerely appreciated. None of this work would have been achieved without her support.

I would also like to acknowledge the support and help from my research group members, Dr. Edward K. Vizy, Dr. Christina M. Patricola, Dr. Emily E. Riddle, Naresh Neupane, Meredith Brown, and Jamie Favors, during the course of my studies. Special thanks to Dr. Edward K. Vizy who conducted the simulations used in the last chapter.

Co-chair of my Special Committee, Professor Stephen J. Colucci, and other members, Professor Peter Hess and Professor Todd Walter, are deeply acknowledged for their invaluable support and instruction. Insightful and constructive comments from Professor Peter Hess and Stephen J. Colucci on the last chapter are gratefully appreciated.

Many thanks to those people who helped me during my stay at Cornell University and the University of Texas at Austin. Special thanks to Pamela M. Vitale, Brian Belcher, Heather E. Routt, and Ty Lehman for their help and technical support before and during my dissertation defense. Financial support from Department of Energy's Abrupt Climate Change Program is also acknowledged.

Finally, I would like to thank my family and dearest friends in China and the United States. It is your love and encouragement that carry me through the difficulties I have encountered.

TABLE OF CONTENTS

LIST OF FIGURES

LIST OF TABLES

CHAPTER 1

DYNAMICS OF THE WEST AFRICAN WESTERLY JET[1]

1.1 Introduction

It has long been recognized that the eastern tropical Atlantic is an important moisture source for West Africa, and that low-level westerlies transport moisture onto the continent in boreal summer (Lamb 1983; Koster et al. 1986; Cadet and Nnoli 1987; Druyan and Koster 1989; Grist and Nicholson 2001; Fontaine et al. 2003). The westerly flow near 10°N along the West African coast was identified as a jet in satellite-based observations by Grodsky et al. (2003). Here we refer to this feature as the West African westerly jet (WAWJ), and study its dynamics.

West Africa is known to have especially strong atmosphere-ocean-land surface interactions. The association between the WAWJ and moisture transport onto the continent suggests that the jet plays an important role in the coupled system. In this paper we investigate the basic dynamics of the WAWJ's formation and maintenance. The jet's climatological structure, seasonality, and diurnal cycle are documented, and the processes that cause it to form and persist are investigated. In particular, we clearly distinguish the WAWJ from the westerly monsoon flow.

Studies of the low-level westerly flow over West Africa are reviewed in the following section. Section 1.3 is a description of the datasets and methods used to investigate the WAWJ dynamics. In section 1.4, climatological features of the WAWJ in the reanalyses are presented, and the jet dynamics is diagnosed in section 1.5. The last section contains the main conclusions.

---

[1] Pu, B., and K. H. Cook, 2010: Dynamics of the West African westerly jet. *J. Climate*, 23, 6263-6276.

1.2 Background

Low-level jets are known to be important sources of moisture for low-latitude precipitation systems. They are often related to orographic features, such as the Great Plains, South American, and Somali low-level jets, but not necessarily, as in the Caribbean low-level jet.

Based on the QuikSCAT scatterometer wind data, Grodsky et al. (2003) find that the surface westerlies embedded within the Atlantic ITCZ at about 7°N-12°N near the West African coast form a jet that persists from May to September, with a maximum wind speed exceeding 7 m s^{-1} in late boreal summer. In strong jet years, e.g., 1999, they report surface westerly wind speeds in excess of 15 m s^{-1} at some locations. Grodsky et al. (2003) find that a linear three-term (pressure gradient, Rayleigh friction, and Coriolis force) momentum balance provides a reasonable description of the zonal winds. They conclude that the jet is in near-geostrophic balance, and the meridional pressure gradient is generated by a westward extension of the continental thermal low over the eastern Atlantic.

Grodsky et al. (2003) also discuss how the ocean responds to the WAWJ. They find that both observations and GCM simulations suggest that the jet cools the SST by ~ 0.3 K through entrainment and latent heat loss. The Ekman pumping associated with the jet causes cooling and shallowing of the ocean mixed layer to the north and warming and deepening to the south. The resulting strengthened meridional gradient of sea surface height between 10°N and the equator could intensify the North Equatorial Counter Current transport by 15%.

Several factors inspired us to pursue further study of the WAWJ. One is results from a study of the African Humid Period (AHP), which occurred 6-8,000 years ago at a time of high surface moisture across the Sahel and Sahara caused by greater summertime insolation. Atmospheric GCMs typically under-predict AHP rainfall

(Braconnot et al. 2000). Patricola and Cook (2007) used a regional climate model (atmosphere only) to show that one can capture a reasonable simulation of the AHP if the changed conditions of the land surface (most notably, soil moisture) are specified in the model in addition to the increased summer insolation. The monsoon flow across the Guinean coast does not change between the present day and AHP simulations, but the WAWJ strengthens and deepens considerably and is the primary source of moisture for the northward expansion of the monsoon. This response, combined with the elimination of the African easterly jet along with its role in transporting moisture off the continent (Cook 1999), explains the increased wetness of the AHP climate. The failure of coarser-resolution models to resolve this jet may be one reason atmospheric GCMs under-predict AHP rainfall.

Another regional modeling study also exposed a crucial role for the WAWJ in West Africa climate change and variability. Patricola and Cook (2008) used a coupled atmosphere/vegetation regional model to generalize the results from the AHP study described above and understand the implications for potential abrupt climate change over northern Africa. Idealized simulations were conducted to test the dependence of the northern Africa climate on the initial conditions specified for vegetation. When the coupled model is initialized with the Sahara desert border placed anywhere south of 17.9°N, the coupled model equilibrates to a climate similar to today's climate. In contrast, when the coupled model is initialized with the Sahara border at or north of 17.9°N, a "green Sahara" solution results. This green Sahara solution occurs because the initial conditions place higher levels of soil moisture at the latitude of the thermal low. Initially fueled by moisture evaporated from the surface, the thermal low deepens and replaces the dry, shallow thermal low/Saharan high system of the present day climate. Again, the WAWJ is the agent that sustains a strong moisture flux into northern Africa; the southerly monsoon flow across the Guinean coast is unchanged.

These studies demonstrate that the westerly flow onto the continent — nominally the WAWJ — can vary independently of the southwesterly monsoon flow. There are two distinct low-level westerly flow regimes important for transporting moisture to the West Africa continent in summer months. One is the westerly component of the monsoon flow which results from the Coriolis acceleration acting on the southerly flow across the Guinean coast driven most fundamentally by land/sea contrast. The other is the WAWJ.

Previous studies have examined the westerly flow onto northern African's west coast and documented its importance in bringing moisture onto the African continent without identifying the flow as a jet. Gu and Adler (2004) find that the formation of strong low-level westerly flow between 10°W and 10°E at 850 hPa is coincident with the development of rain along 10°N over West Africa in June and July. During boreal summer, when moisture transport from the Gulf of Guinea is reduced due to the development of the Atlantic cold tongue, transport by westerly winds can be very important. Sijikumar et al. (2006) find that both in a regional model and the ERA40 reanalysis the onset of the West African monsoon is characterized by an enhanced westerly flow at 10°-15°N between the eastern Atlantic and the continent.

Previous studies also demonstrate the importance of the westerly flow in the region's variability, but without distinguishing between the WAWJ and the monsoon westerlies. Grist and Nicholson (2001) find differences in the westerly flow between 10°W and 20°E between wet and dry years in the Sahel, with westerly flow anomalously strong and deep during wet years. Nicholson and Grist (2003) suggest that the westerlies are best developed from July through September, especially between 10°W and 10°E in association with Coriolis acceleration of the southeasterly trades. Tomas and Webster (1997) indicate that inertial instability adds to this westerly acceleration. Jury et al. (2002) demonstrate a link between the zonal wind in the

central Atlantic (10°S–5°N, 40°W–0°E) and African rainfall. Fontaine et al. (2003) find that the near surface (1000-925 hPa) westerly moisture flux is enhanced in wet years. Using a regional climate model, Hagos and Cook (2008) find that, in response to Atlantic and Indian Ocean warming in the 1990s, anomalous westerly flow brings moisture onto the West Africa continent to support the Sahel rainfall recovery of that period.

In summary, previous work suggests that this small feature—the WAWJ—is important for understanding climate—including its variability and change—in Sahelian Africa.

1.3 Methodology

The 6-hourly ERA40 reanalysis (Uppala et al. 2005; UCAR/NCAR/CISL/DSS and ECMWF, 2005) at T106 resolution (equivalent to about 1.125° latitude by 1.125° longitude on the Gaussian grid) from 1958 to August 2002 is used to create the climatological daily and 6-hourly variables used in this study. This reanalysis is chosen as the primary source because of its relatively high spatial resolution and long time coverage. We choose not to extend the analysis past August 2002 because the ERA40 reanalysis is sufficiently long to provide a climatology. This is preferable to avoid issues that would arise if we extended the record by matching with a different reanalysis.

In regions with a sparse observing network such as West Africa, any reanalysis product relies heavily on model simulation. So we also compare the ERA40 reanalysis to the monthly NCEP/NCAR reanalysis (NCEP1; Kalnay et al. 1996) from 1958 to 2001 and the NCEP/DOE AMIP-II reanalysis (NCEP2; Kanamitsu et al. 2002) daily reanalysis from 1979 to 2001. These products have a coarser resolution than the ERA40 reanalysis, at 2.5° latitude and longitude. Since satellite observations are not

available before 1979, we compared the jet climatologies for 1958-1987 and 1979-2001. For the years after 2001, we also examined the ERA-Interim reanalysis climatology (Simmons et al. 2007a, b) for 1989-2008 and the ECMWF AMMA operational analysis climatology (http://bddamma.ipsl.polytechnique.fr/available-datasets-4.html) for 1999-2007.

The QuikSCAT SeaWind observations used by Grodsky et al. (2003) have higher resolution (25 km by 25 km) than the ERA40 reanalysis. However, the time coverage of this wind dataset is shorter (June 1999-present) and is, therefore, not suitable for a study of the climatological jet.

To understand the formation and maintenance of the WAWJ, terms in the horizontal momentum balance are analyzed in the following vector form:

$$\frac{d\vec{V}}{dt} = -\nabla\Phi - f\vec{k}\times\vec{V} + \vec{F}_h, \tag{1.1}$$

where the Lagrangian acceleration is defined by

$$\frac{d}{dt} = (\frac{\partial}{\partial t})_p + \cdot(u\frac{\partial}{\partial x} + v\frac{\partial}{\partial y})_p + \omega\frac{\partial}{\partial p}\ . \tag{1.2}$$

$\vec{V} \equiv (u,v)$ is the horizontal velocity vector, in which u is the zonal wind and v is the meridional wind. ω is the vertical p-velocity. The first term on the right side of Eq. 1.1 is the acceleration due to horizontal geopotential height gradients, where Φ is geopotential height. The second term is the horizontal Coriolis acceleration, where $f \equiv 2\Omega\sin\varphi$ is the Coriolis parameter, Ω is the angular speed of rotation of the earth $=7.292\times10^{-5}$ rad s^{-1}, and φ is latitude. The third term represents horizontal friction, which is calculated as a residual in the analysis and so contains error due to the estimation of derivatives by finite differencing.

The component equations of Eq. 1.1 are also used in the analysis as follows:

$$\frac{du}{dt} = -\frac{\partial\Phi}{\partial x} + fv + R_x \tag{1.3}$$

and

$$\frac{dv}{dt} = -\frac{\partial \Phi}{\partial y} - fu + R_y \tag{1.4}$$

where R_x and R_y are the residual terms mentioned above.

The ageostrophic zonal wind is also examined, defined by

$$u_a = u - u_g = u + \frac{1}{f}\frac{\partial \Phi}{\partial y} = -\frac{1}{f}\left(\frac{dv}{dt} - R_y\right). \tag{1.5}$$

The 6-hourly ERA40 reanalysis and forecast surface variables are used to derive climatological (1958-2001) daily values for the surface heat budget analysis in section 1.5. Assuming that there are no horizontal or vertical heat fluxes out of or into the atmosphere/ocean column, the net surface heating is calculated based on the following equation:

$$Q_{net} = Q_{sw} + Q_{lw} + Q_{sh} + Q_{lh}, \tag{1.6}$$

where Q_{net} is the net surface heating, and Q_{sw}, Q_{lw}, Q_{sh}, and Q_{lh} are the net downward solar radiation, net upward longwave radiation, upward sensible heat flux, and upward latent heat flux, respectively.

1.4 The WAWJ in the Reanalyses

Figures 1.1a and b display the 1958-2001 July-September climatology of winds and geopotential heights at 925 hPa over West Africa in the ERA40 and NCEP1 reanalyses, respectively. In the ERA40 reanalysis (Fig. 1.1a), the WAWJ is located off the African west coast between 8°N and 11°N, clearly distinguished from the southwesterly monsoon flow maximum over the continent between 0°E and 5°E. The jet is not well captured in the lower-resolution NCEP1 reanalysis (Fig. 1.1b), but the two reanalysis products are in general agreement about the large-scale flow and geopotential height distribution. An examination of the other reanalysis products listed in section 3 also produce WAWJ features that are consistent with those in the ERA40

climatology (not shown), justifying the use of the ERA40 reanalysis for this investigation.

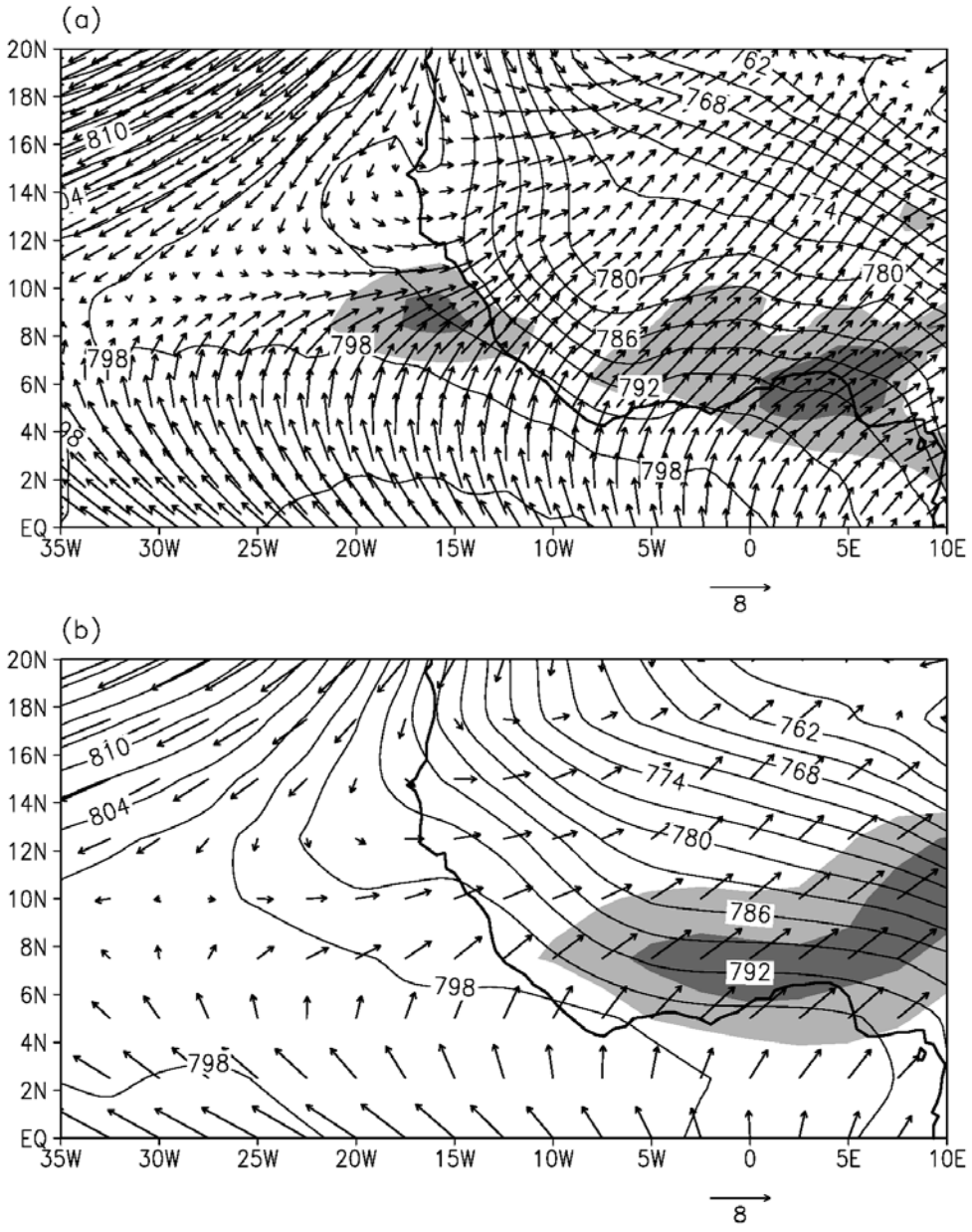

Figure 1.1 925 hPa winds (m s^{-1}) and geopotential heights (gpm) in the (a) ERA 40 and (b) NCEP1 reanalysis climatologies (1958-2001), averaged from July to September. Zonal wind speeds above 4 m s^{-1} are shaded with light gray, and above 5 m s^{-1} with dark gray. Contour intervals are 3 gpm.

Daily climatological variables are used to study the structure and seasonal cycle of the WAWJ. Based on zonal wind velocities at 925 hPa between 8°N and 11°N off the west coast, five stages of jet development are defined. In Stages 1 and 5, when the jet forms and terminates, the core zonal wind speed is between 1.5 m s^{-1} and 3 m s^{-1}. In Stages 2 and 4, when the jet intensifies and weakens, the zonal wind is between 3 m s^{-1} and 5 m s^{-1}, and in Stage 3, when the jet reaches its maximum, the westerly wind is greater than 5 m s^{-1}. Figures 1.2a-e display wind vectors, zonal wind shading, and geopotential height contours for each stage.

Stage 1 (Fig. 1.2a) lasts from June 7th until June 27th. Westerly winds develop in the jet region during this stage, with flow down the geopotential height gradient toward land. From June 28th until July 21st, defined as Stage 2, the low-level jet intensifies. As shown in Fig. 1.2b, the thermal low (e.g., the 800 gpm contour) extends westward over the ocean during this time. This forms an offshore low (marked with an "X") which is related to the dynamics of the jet formation discussed below. Note that there is evidence of the low's formation as a region of offshore cyclonic winds in Stage 1 (Fig. 1.2a). The WAWJ extends westward to 22°W and strengthens, with a zonal wind maximum of 4 m s^{-1} at 8°-10°N. Over land, the zonal wind at 14°-18°N is also stronger than in Stage 1 as the monsoon flow expands northward to about 19°N over West Africa.

The jet reaches peak intensity in Stage 3 (Fig. 1.2c). From July 22nd until September 5th, it extends from 13°W to 30°W, and the offshore low extends to about 34°W. At 8°-10°N, zonal wind speeds reach 5 m s^{-1}. When the jet expands eastward across the coast, the winds become northwesterly, pointing down the geopotential height gradient toward the continental thermal low.

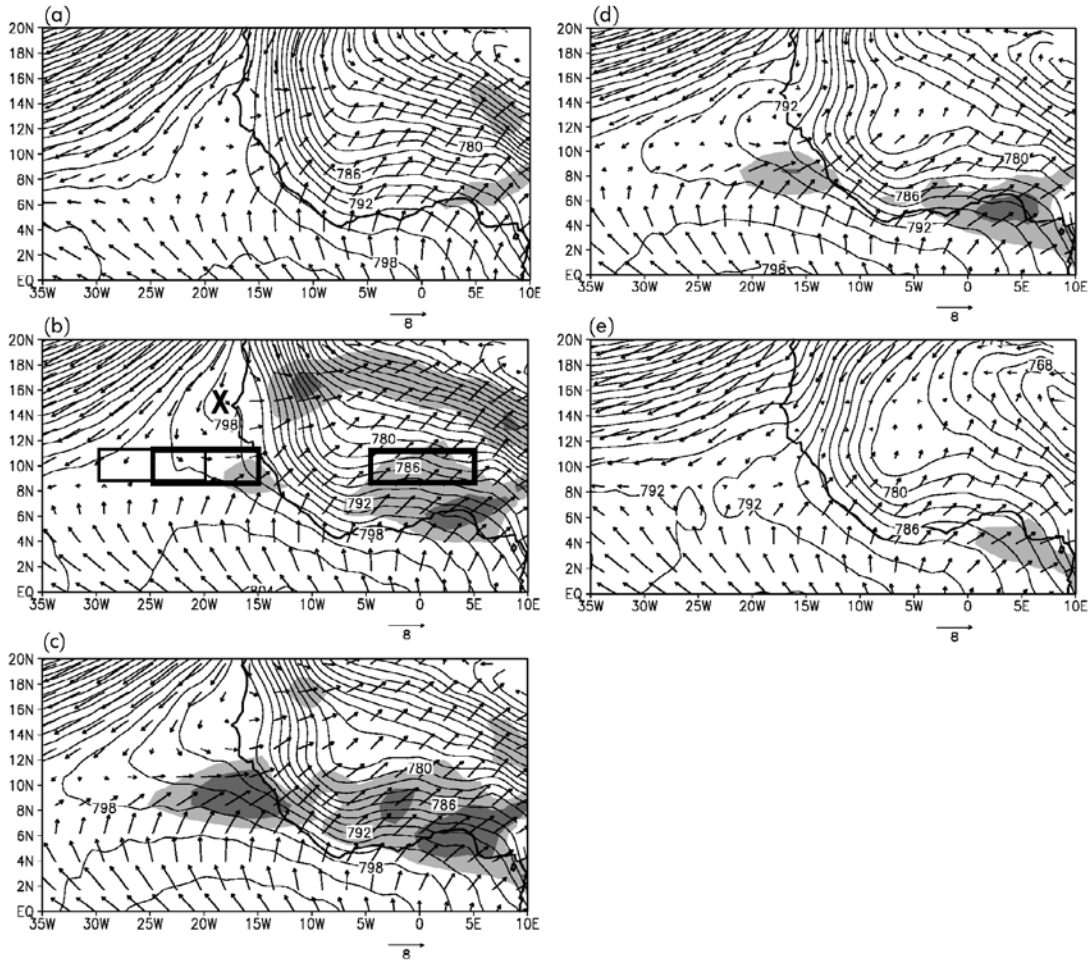

Figure 1.2 Same as Figure 1.1 but for the five stages of jet development in the ERA40 analysis (see text). Only one in two wind vectors are plotted for clarity. In Fig. 1.2b, the black thin box (9.5°-10.6°N, 20°-30°W) represents the jet acceleration region. The thick boxes over the Atlantic (9.5°-10.6°N, 15°-25°W) and over western Africa (9.5°-10.6°N, 5°W-5°E) are the WAWJ averaging region and the monsoon averaging region, respectively. Topography is masked out.

In Stage 4 (Fig. 1.2d), from September 6th to September 19th, the westerly jet weakens to about 4 m s^{-1}, and the offshore low moves southward to 8°-14°N. The jet dissipates in Stage 5 (Fig. 1.2e). From September 20th to October 18th, the westerly winds over the ocean diminish to 1-2 m s^{-1} and the low moves southward to 5°-10°N.

Figure 1.3a displays a latitude-height cross-section of the zonal wind speed averaged from 15°W to 25°W during the jet maximum (Stage 3). The jet core is located at 925 hPa between 8°N and 10°N. Westerly flow extends up to 700 hPa, embedded in the large-scale easterlies. The African easterly jet core is located above (600-700 hPa) and north (17°N) of the WAWJ. The tropical easterly jet core is located to the south, near 5°N, at about 250 hPa.

Figure 1.3b shows a longitude-height cross section at 9.5°N, also for Stage 3. (Note that the streamlines intersect the 1000 hPa surface vertically in both Figs. 1.3a and b in regions with relatively strong vertical velocity because of the 10^3 scaling used. The physical surface over the ocean is at about 1013-1014 hPa.) Below about 750 hPa, the flow is mostly westerly from 35°W to 20°E. The WAWJ maximum is located between 15W° and 18°W, with a magnitude of 6 m s^{-1} at 925 hPa. Again, the WAWJ is distinguished from the maxima in the westerly flow over land, which is located at 2°W and 6°-15°E between 900 hPa and 800 hPa.

Compared with the results of Grodsky et al. (2003), the monthly mean westerly wind speed in the jet region is 1 m s^{-1} weaker in the ERA40 reanalysis climatology. This may be due to the lower resolution of the ERA40 reanalysis compared with the QuikSCAT data, or to differences in the averaging periods.

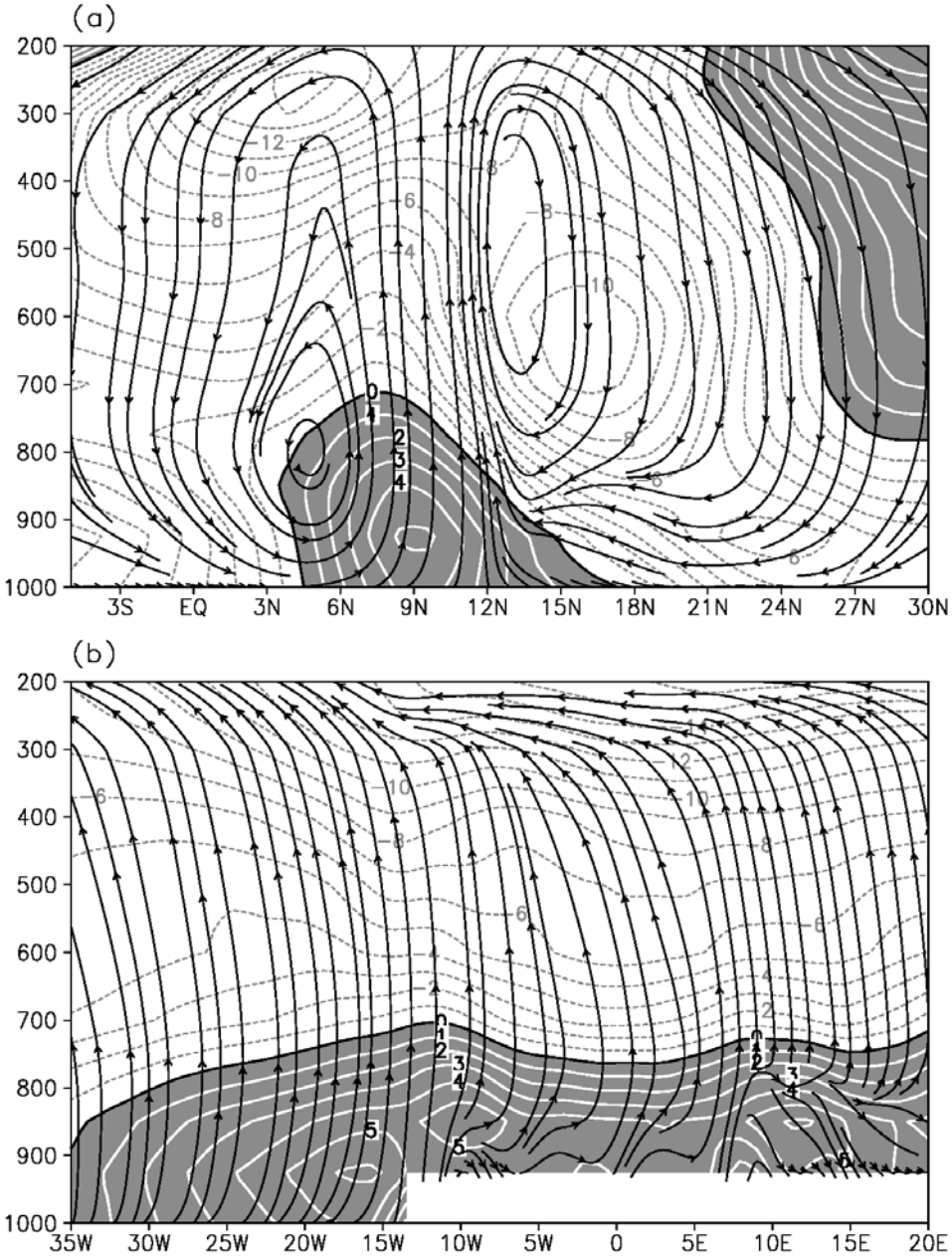

Figure 1.3 Cross-sections of zonal wind speed (m s^{-1}; westerlies shaded) in the ERA40 reanalysis with (a) streamlines of meridional and vertical winds (scaled by 10^3) averaged between 15°W and 25°W and (b) streamlines of zonal and vertical winds at 9.5 °N, averaged from July 22nd to September 5th. Topography is masked out.

To understand the diurnal and seasonal cycles of the WAWJ and compare them with the monsoon flow, two averaging regions are chosen. For the WAWJ, the averaging region is 9.5°-10.6°N and 15°-25°W, and for the monsoon region it is 9.5°-10.6°N and 5°W-5°E (see Fig. 1.2b). The averaging region for the WAWJ was chosen as the area over which the jet is best defined as purely westerly, and it captures the maximum westerly wind speed. The averaging region for the monsoon flow is located over the same latitude range, and has the same longitudinal extent centered on the Greenwich meridian. A "jet acceleration" region to the west of the jet maximum is also defined (9.5°-10.6°N and 20°-30°W). The results presented below are not strongly dependent on the exact location of the averaging regions.

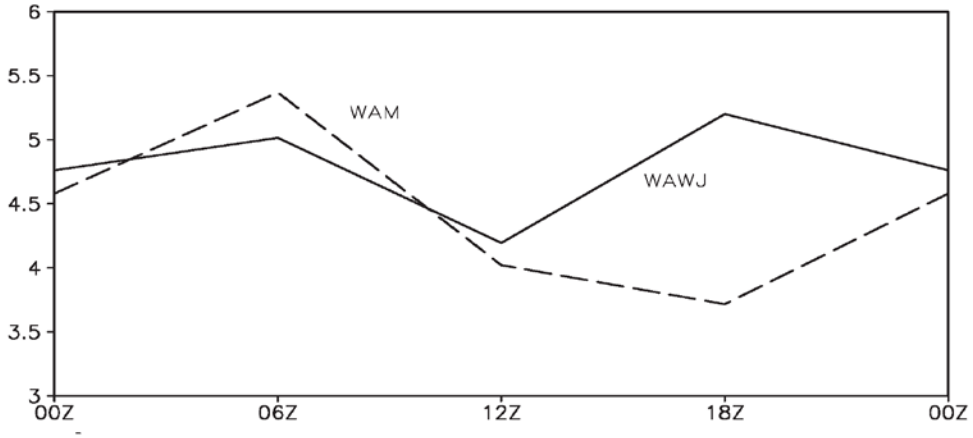

Figure 1.4 6-hourly zonal wind speeds (m s-1) in the WAWJ (solid) and the West African monsoon (WAM, dashed) averaging regions (see Fig. 1.2b) in the ERA40 reanalysis, averaged in Stage 3. The time axis is UTC. Local time in the jet region is UTC-1 hour. In the monsoon region, local time is the same as UTC.

Figure 1.4 displays climatological 6-hourly zonal wind speeds in the WAWJ (solid line) and the monsoon (dashed line) regions for Stage 3. The WAWJ has a weak semidiurnal cycle, with two daily maxima at 6Z and 18Z (5 AM and 5 PM local time). It is a little stronger at 18Z with a wind speed of about 5 m s^{-1}, and weakest at 12Z (11

AM local time) with a speed of 4.2 m s^{-1}. The cycle is similar in the other stages. In the monsoon region, the zonal winds have only one maximum each day, about 5.4 m s^{-1} at 6 AM local time, and a minimum of 3.7 m s^{-1} at 6 PM. The wind speed diurnal range in the monsoon region is about twice that in the jet region.

The seasonal development of the wind components in the jet region is shown in Figure 1.5a. The zonal wind is easterly in May, changes to westerly in early June, maintains a maximum from late July to early September, and returns to easterly in late October. The meridional wind has a similar seasonal cycle to the zonal wind, but the speeds are 3-4 m s^{-1} lower after the WAWJ begins to form. The vertical velocity is relatively strong in the jet region, and it develops rapidly in early summer. These large upward vertical velocities indicate that the WAWJ is co-located with the Atlantic ITCZ, as mentioned by Grodsky et al. (2003).

Figure 1.5b shows the wind components in the monsoon region. Variations in wind speeds are smaller than in the jet region during the analysis period. The zonal wind remains westerly through almost all of the analysis period, increasing from about 2.5 m s^{-1} in May and June to a maximum of about 5 m s^{-1} from mid-July to mid-August. It peaks about 2 weeks earlier than the WAWJ. The meridional wind is comprised of southerly flow at approximately 4 m s^{-1} throughout the spring and summer, exceeding the zonal wind speed until early July. The vertical velocity in the monsoon region is small throughout the period, further distinguishing the monsoon dynamics from that of the WAWJ. Weak subsidence from May through early June is replaced by essentially zero vertical velocities for the rest of the period.

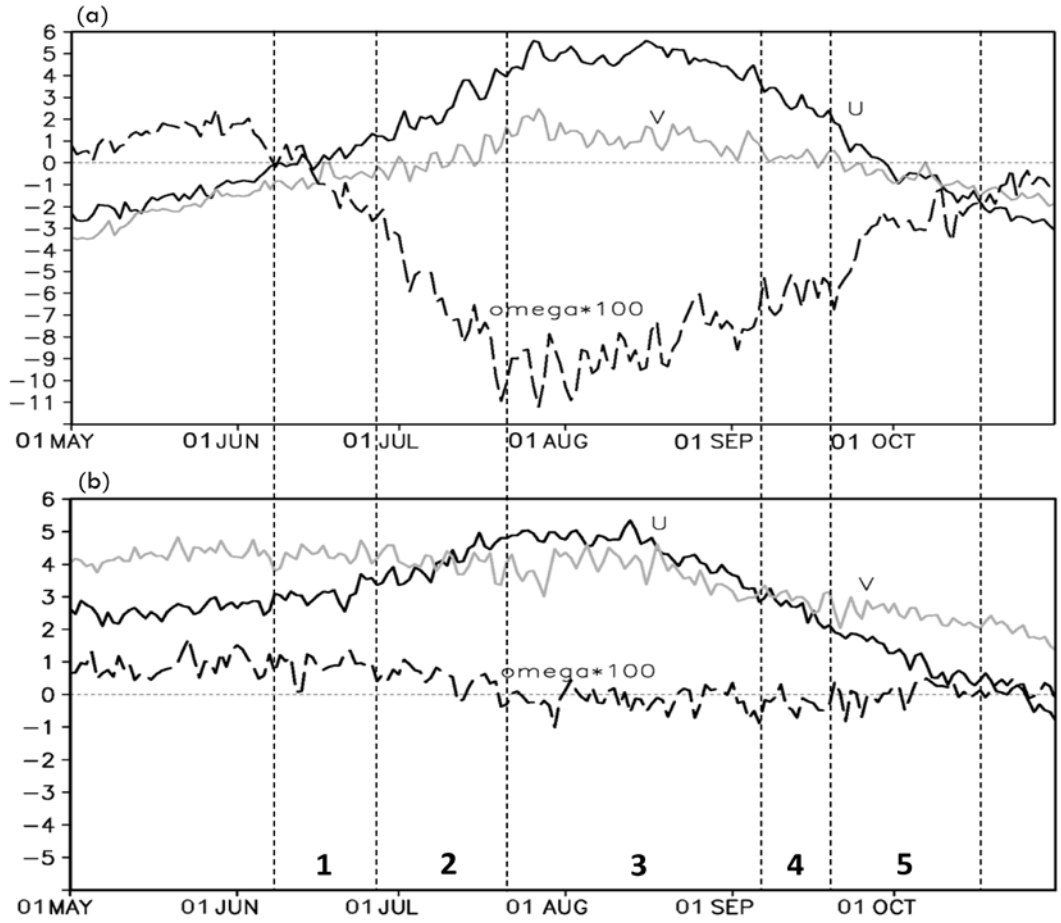

Figure 1.5 Averaged wind speeds in the (a) WAWJ (15°-25°W) and (b) monsoon (5°W-5°E) regions at the same latitudes (9.5°-10.6°N) in the ERA40 reanalysis. The averaging regions are shown in Fig. 1.2b. Black solid, gray solid, and black dashed lines represent the averaged zonal, meridional (m s^{-1}) and vertical p-velocities (Pa s^{-1}, scaled by 10^2), respectively. The numbers indicate the stages of the WAWJ as defined in Fig. 1.2.

1.5 Formation of the WAWJ

a. Dynamics

Tomas and Webster (1997) discuss the mechanisms of low-level tropical westerly flow. They suggest that when the cross-equatorial pressure gradient is large, in the vicinity of the zero absolute vorticity (η) contour, strong zonal wind shear is

needed to balance the absolute vorticity advection associated with divergent flow. Therefore, in the Northern Hemisphere, a tropical low-level westerly maximum tends to appear north of the $\eta = 0$ contour. An example of the low-level westerly maximum in the Indian Ocean in boreal summer is displayed to support the argument.

Whether this theory is sufficient to explain the formation of the WAWJ is examined in the ERA40 reanalysis. Over the eastern Atlantic, the $\eta = 0$ contour is located near 4°N in August, with a maximum zonal wind shear positioned near 4°-5°N (not shown). From 20°W to 40°W, westerlies are located to the north of the $\eta = 0$ contour, while easterlies are located to the south. However, the WAWJ is located about 5° farther north of this zonal wind shear maximum, which suggests that the formation of the jet is not only related to the large-scale absolute vorticity advection but also is associated with regional scale dynamics. Also, as pointed out by Grodsky et al. (2003), this mechanism does not explain the westward extension of the continental thermal low and the southward pressure gradient in the jet region. Here we try to answer these questions through momentum and surface heat budgets analyses.

Figures 1.6a-d display the spatial distribution of each term in the vector horizontal momentum equation (Eq. 1.1) at the time of the WAWJ maximum (Stage 3). The contours and vectors indicate the magnitudes and directions of the forces, respectively.

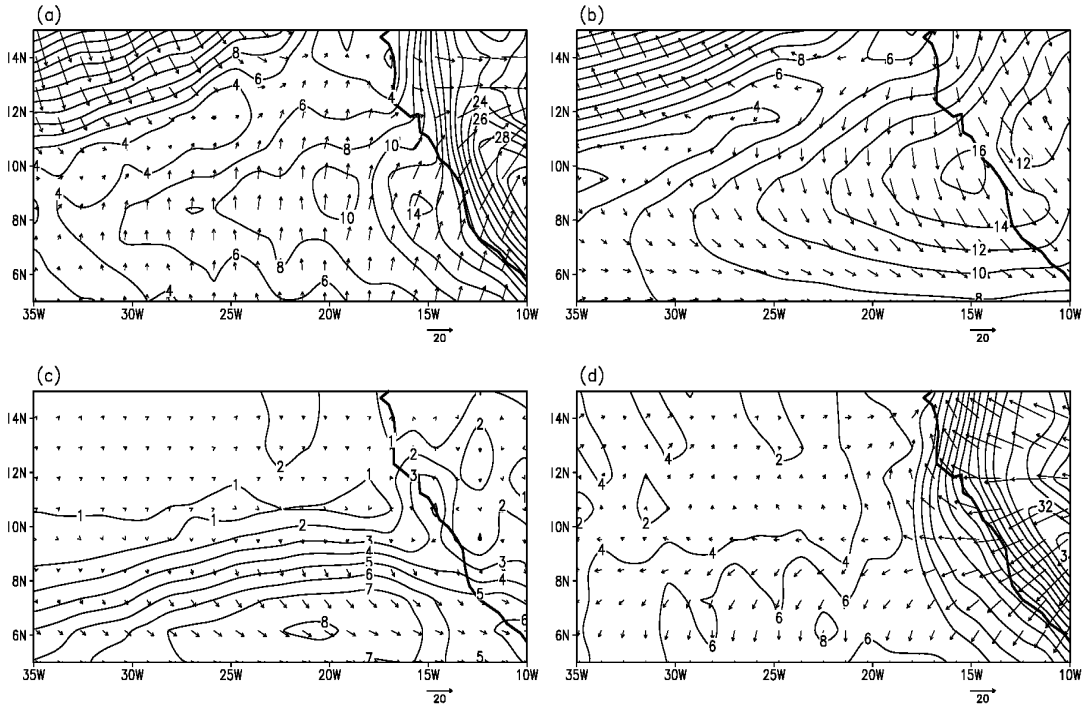

Figure 1.6 Vectors representing terms in Eq. 1.1, with contours showing magnitudes (10^{-5} m s^{-2}), averaged over the jet maximum period, as follows: (a) geopotential height gradient, (b) Coriolis, (c) acceleration, and (d) residual terms.

Within the North Atlantic subtropical high, in the upper left corner of each panel (11°N-15°N and 22°W-35°W), the flow is essentially geostrophic, with large and opposite pressure gradient (Fig. 1.6a) and Coriolis terms (Fig. 1.6b), and small acceleration and friction terms (Figs. 1.6c and d, respectively).

Further south, over the eastern Atlantic in the vicinity of the WAWJ (7°N-11°N and 14°W-32°W), pressure gradient forces (Fig. 1.6a) are directed mainly northward, with a maximum between 8°N and 10°N near 20°W, south of the offshore low (Fig. 1.2b). The Coriolis forces in this region (Fig. 1.6b) are directed southward and southeastward, with magnitudes 2-3×10^{-5} m s^{-2} greater than the pressure gradient forces. The acceleration term (Fig. 1.6c) is small in the vicinity of the WAWJ, but south of the jet region the acceleration is greater and aligned with the Coriolis force.

The residual term is comparable in magnitude to the acceleration term (Fig. 1.6d). It opposes the wind direction in general, supporting the interpretation of this term as friction.

Over West Africa, the flow is strongly ageostrophic, with pressure gradient and Coriolis forces essentially perpendicular to each other (Figs. 1.6a and b). The acceleration term (Fig. 1.6c) is relatively small. The residual is the largest term, again suggesting that this term reflects frictional accelerations which are expected to be large in the well-developed planetary boundary layer over tropical land surfaces. The residual term decreases rapidly with elevation (not shown).

To understand how the WAWJ forms, the evolution of the momentum balance (Eqs. 1.3 and 1.4) is analyzed in the jet acceleration region (Fig. 1.2b). The climatological meridional acceleration (dv/dt) is shown by the dotted line in Figure 1.7a, with a smoothed version using a 7-day running mean denoted by the black solid line. The numbers in Fig. 1.7a indicate the stages of the WAWJ as defined in Fig. 1.2. The meridional acceleration is negative during Stage 3, i.e., during the maximum of the WAWJ, and positive at all other times.

Each term in the meridional momentum budget (rhs of Eq. 1.4) is shown in Figure 1.7b. The first-order momentum balance is geostrophic. Negative values of the pressure gradient force before the middle of July are associated with the high to the north of the WAWJ acceleration region. This negative pressure gradient force weakens from May through July as the North Atlantic subtropical high intensifies and shifts northward in its normal seasonal cycle (see Figs. 1.2a-c). At the same time, the marine ITCZ moves northward in its seasonal cycle. The low-level convergence zone, which moves to about 11°N in the far eastern Atlantic because of the proximity to the continent (Hagos and Cook 2005), becomes co-located with the jet acceleration region in July (Fig. 1.2c), and the pressure gradient force changes sign (Fig. 1.7b).

From mid-July to early September, the Coriolis force associated with the high zonal velocities of the WAWJ is approximately 2.5×10^{-5} m s^{-2} greater than the pressure gradient force. Thus, the WAWJ is super-geostrophic when it is mature.

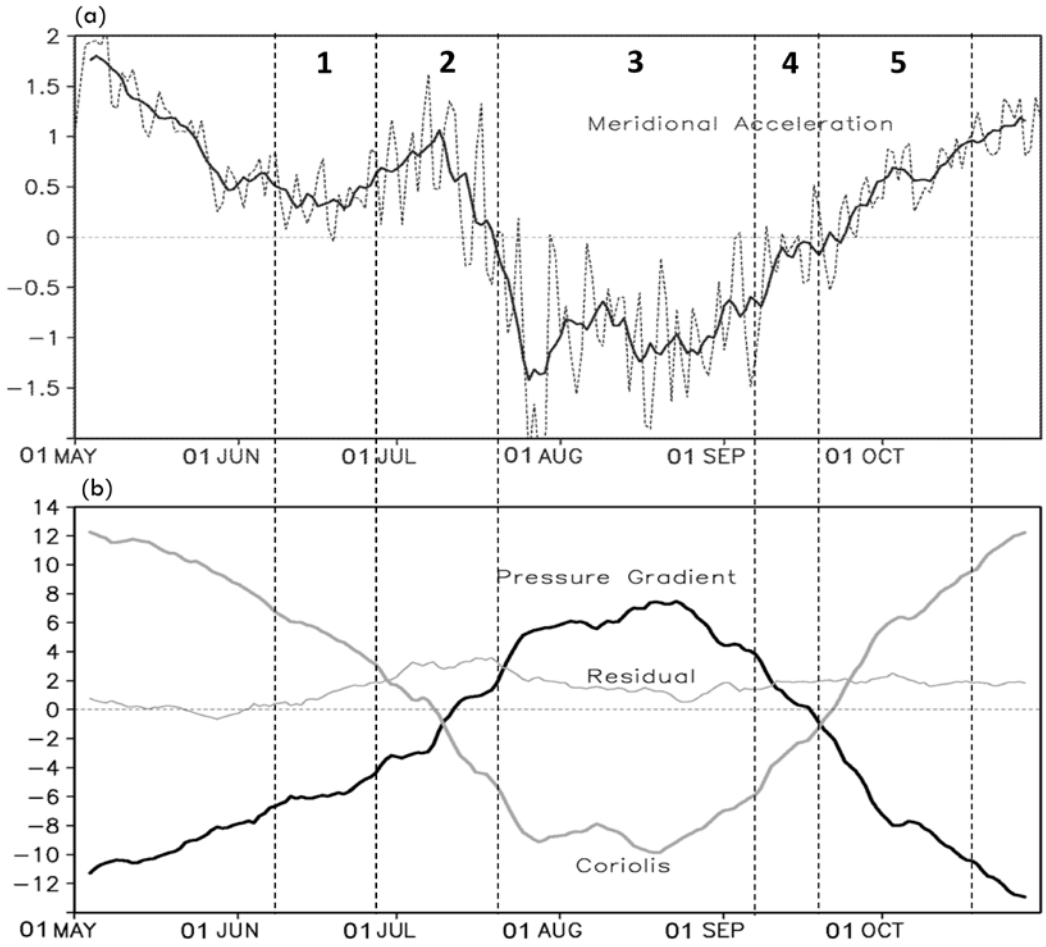

Figure 1.7 Meridional momentum budget terms (Eq. 1.4) in the jet acceleration region (shown in Fig. 1.2b), calculated from the ERA40 reanalysis. (a) Meridional acceleration (black dotted line) with 7-day running mean (black solid line). (b) 7-day running mean of the meridional geopotential height gradient (black thick line), Coriolis (gray thick line), and residual (gray thin line; 10^{-5} m s^{-2}).

An examination of the u-momentum balance (Eq. 1.3) explains the processes that accelerate the flow eastward. The climatological zonal acceleration (du/dt) is

shown by the dotted line in Figure 1.8a, with a smoothed version using a 7-day running mean denoted by the black solid line. Positive (eastward) acceleration increases by about 1×10^{-5} m s^{-2} from Stage 1 to 2, and the westerly wind intensifies. In Stage 3, the eastward zonal acceleration weakens after a maximum in late July, and becomes westward in early September. The westward zonal acceleration strengthens through Stages 4 (Fig. 1.2d) and 5 (Fig. 1.2e), and the jet is destroyed.

Each term on the rhs of Eq. 1.3 is plotted in Fig. 1.8b. The zonal momentum balance is approximately geostrophic until the middle of July, with opposing pressure gradient and Coriolis forces decreasing in magnitude as the continental thermal low extends westward over the eastern Atlantic (Figs. 1.2a and b), and with friction supporting the pressure gradient force. After the middle of July, the pressure gradient force settles into a relatively low positive value (about 2×10^{-5} m s^{-2}) as the westward extension of the thermal low becomes established (Fig. 1.2c). The Coriolis force changes sign at the end of Stage 2, and zonal geostrophic balance is interrupted during the jet maximum period (Stage 3). This change in the sign of the u-momentum equation Coriolis force, i.e., the sign change in v shown in Fig. 1.5a, occurs as the low-level tropical convergence zone (the marine ITCZ) moves across the jet acceleration region.

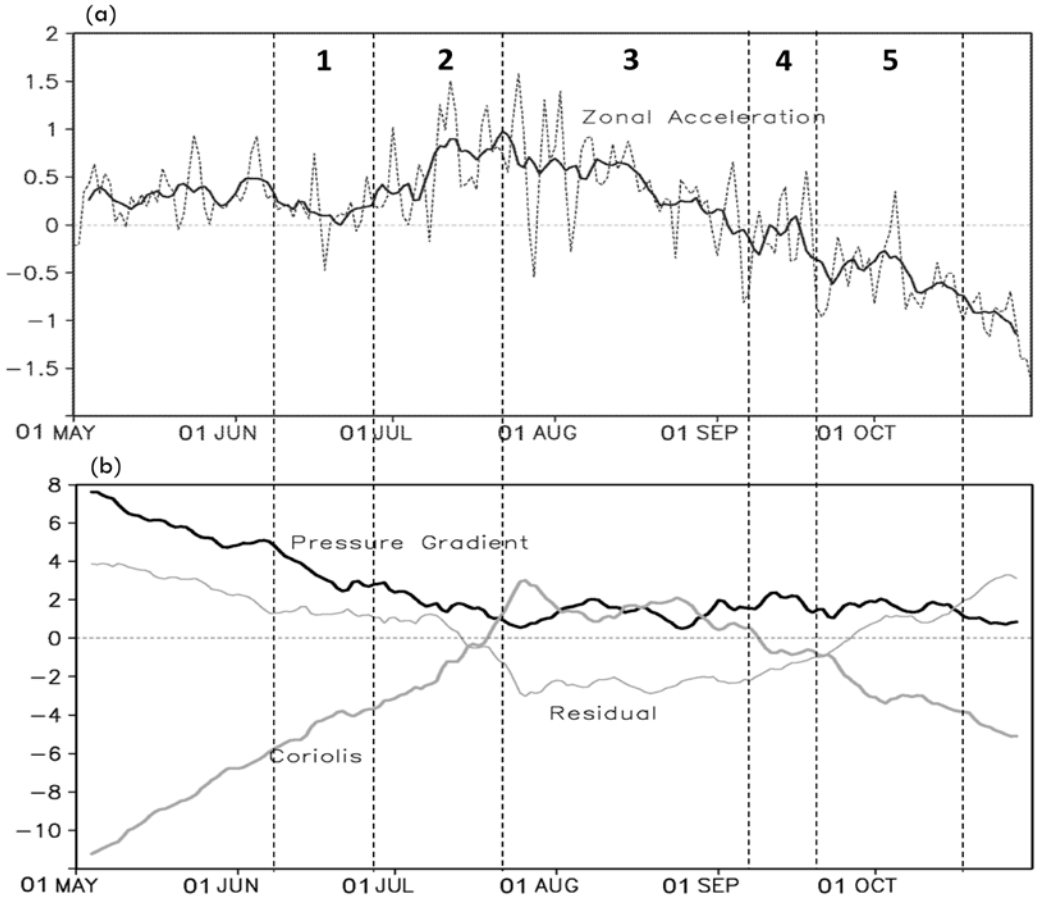

Figure 1.8 Same as Fig. 1.7, but for the zonal momentum budget (Eq. 1.3).

Figure 1.9 shows the zonal geostrophic and ageostrophic wind components, calculated based on Eq. 1.5, along with the total wind speed in the jet acceleration region. From early June to mid-July, and from late September to mid-October, the ageostrophic wind is in the opposite direction to the geostrophic wind, since the pressure gradient force ($-\partial\phi/\partial y$) is greater than the Coriolis force (fu) as seen in Fig. 1.7b. The generation of a westerly ageostrophic wind in Stages 1 and 2 is associated with an increase of the eastward acceleration (Fig. 1.8a), which is related to the decline in the westward Coriolis force (Fig. 1.8b) associated with the northward progression of the Atlantic marine ITCZ as discussed above. From mid-July to late

September, the ageostrophic wind is in the same direction as the geostrophic wind, as the Coriolis force is larger than the pressure gradient force (Fig. 1.7b). This occurs as a result of enhanced westerly acceleration by the zonal Coriolis force. As displayed in Fig. 1.8b, the Coriolis force in the jet acceleration region changes direction from westward to eastward in mid-July, enhancing the westerly flow.

From June to October, the ageostrophic wind component remains steady at about 1 m s^{-1}, so variations in the geostrophic wind explain much of the seasonality of the total zonal wind (Fig. 1.9). The daily zonal wind speed in the jet averaging region is significantly correlated (at the 95% confidence level) with the meridional geopotential height gradient from 8°-10°N and 15°-24°W, and from 7°-14°N and 24°-32°W in all stages.

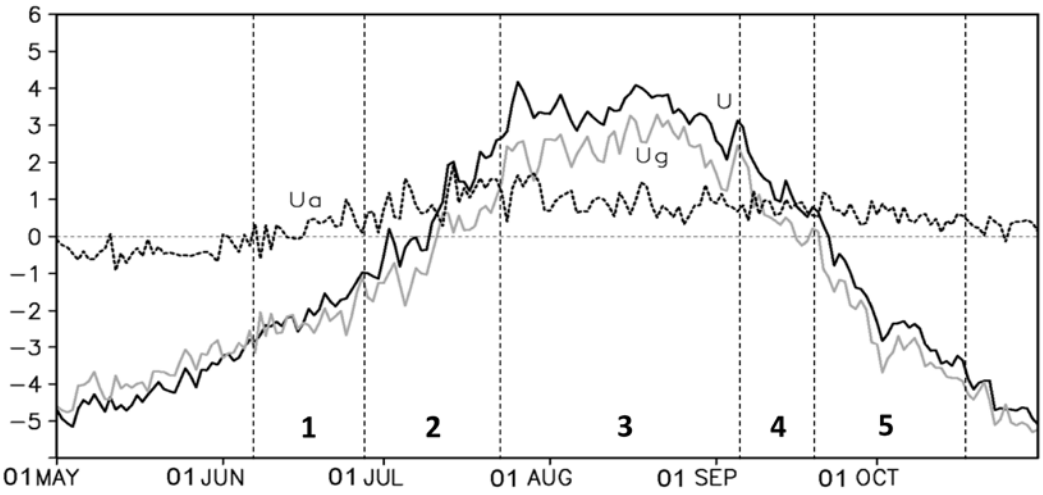

Figure 1.9 Zonal geostrophic (gray solid line), ageostrophic (black dashed line) and total wind speeds (black solid line) in the jet acceleration region.

The above analysis demonstrates that the WAWJ results from multi-scale interactions over the eastern Atlantic. It is also an example of atmosphere-ocean-land surface interaction since its formation is controlled by both continental and ocean

processes. When the seasonal development of the continental thermal low is superimposed on the seasonal progression of the marine ITCZ, a region of enhanced eastward acceleration forms off the west coast of Africa. The resulting WAWJ is, therefore, a regional-scale feature controlled by these large-scale structures.

b. Formation of the offshore low

The pressure gradient at 8°-13°N over the eastern Atlantic is critical to the formation of the WAWJ. As revealed in the reanalysis climatology (Fig. 1.2), the westward extension of the thermal heat low at 925 hPa is associated with the development of an offshore low at 15°N along the West African coast. The formation of the offshore low (Fig. 1.2c) is investigated in this section.

Figures 1.10a-e show SSTs (contoured) with wind vectors and geopotential heights (shaded) at 1000 hPa for each stage of the WAWJ development. The wind and geopotential height fields are similar to those at 925 hPa (see Fig. 1.2), but the relationship with surface heating is more clear at the lower level. Warm SSTs accompanied by low geopotential heights are located near the coast in every stage. In early June, the warmest SSTs are centered between 6°-11°N and 12°-20°W (Fig. 1.10a). From late June to early September, the region of warmest coastal SSTs moves north (Figs. 1.10b-c), and low geopotential heights extend westward over the eastern Atlantic at 10°N, reaching to about 28°W in Stage 3 (Fig. 1.10c). Note that the Atlantic cold SST tongue is evident at 6°-10°N in Stages 3 and 4 (Figs. 1.10c and d). During Stage 4, the warmest SSTs are located at 14°N, essentially coincident with the coastal low (Fig. 1.10d). The warmest SSTs extend southwestward from the West African coast to 24°W and 8°N in October, and the low center moves southward to about 8°N (Fig. 1.10e). Fig. 1.10 suggests that the evolution of the low is associated with heating of the ocean surface, so the surface heat budget is examined.

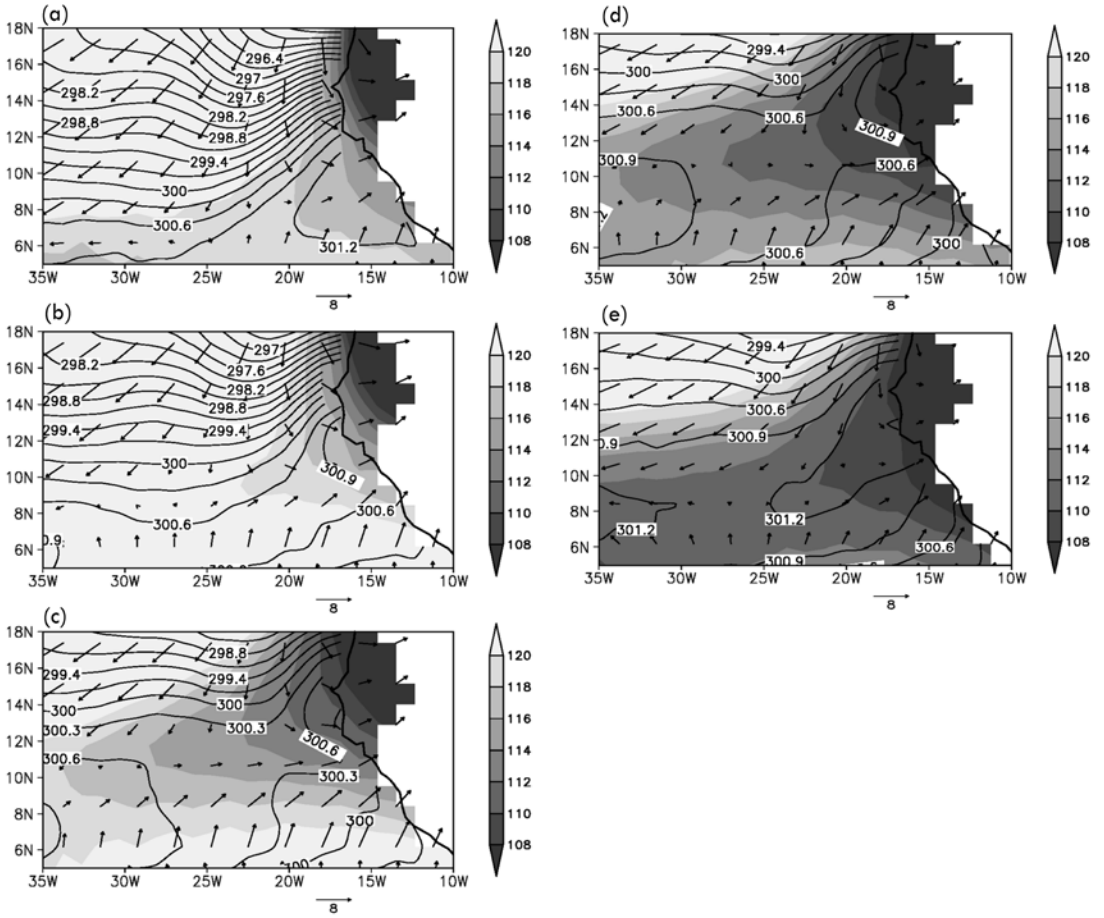

Figure 1.10 Skin temperature (contours), 1000 hPa geopotential heights (shading), and wind vectors in Stages 1 to 5 in (a)-(e), respectively. Contour interval is 2 gpm for geopotential heights, and 0.3 K for temperature. Topography is masked out.

Figure 1.11a displays the net surface heating (Eq. 1.6) from the ERA40 reanalysis for Stage 3. As shown in Fig. 1.11a, net heating values over land are smaller than 10 Wm^{-2}, but a net surface heating maximum of 130 Wm^{-2} is positioned at 17°-23°N over the eastern Atlantic. Near the coast, a net surface cooling maximum of -80 W m^{-2} is located at 13°W and 7°N.

Since the ERA40 heat balance values contain uncertainty (Allan et al. 2004), we also examined the radiation variables in the NCEP1 reanalysis for 1958-2001 and

the satellite-derived variables in the NASA/GEWEX Surface Radiation Budget (SRB; data obtained from the NASA Langley Research Center Atmospheric Sciences Data Center NASA/GEWEX SRB Project) products for 1984-2004. A narrow net surface heating center is found at 15°-18°W and 14°-25°N near the coast in the NCEP1 climatology. Each component of the heat budget in the NCEP1 reanalysis is similar to the ERA40 reanalysis (not shown). Surface solar and longwave radiation in the SRB climatology also show features similar to the ERA40 reanalysis (not shown).

Figure 1.11b shows the skin temperature differences between Stage 3 and Stage 2 (Stage 3 minus Stage 2). Corresponding to the net surface heating rates shown in Fig. 1.11a, SSTs in Stage 3 are about 2 K warmer than in Stage 2 at 17°-21°N near the coast, with relatively warm SSTs extending southward to 6°N at 35°W. Consistent with the surface cooling near 13°W and 7°N, SSTs in Stage 3 are about 0.5 K cooler than in Stage 2 near the western Guinean Coast. The pattern of surface heating shown in Fig. 1.11a, with warming to the north and cooling to the south, moves the coastal SST maximum to the north between Stages 2 and 3 (Figs. 1.10b and c).

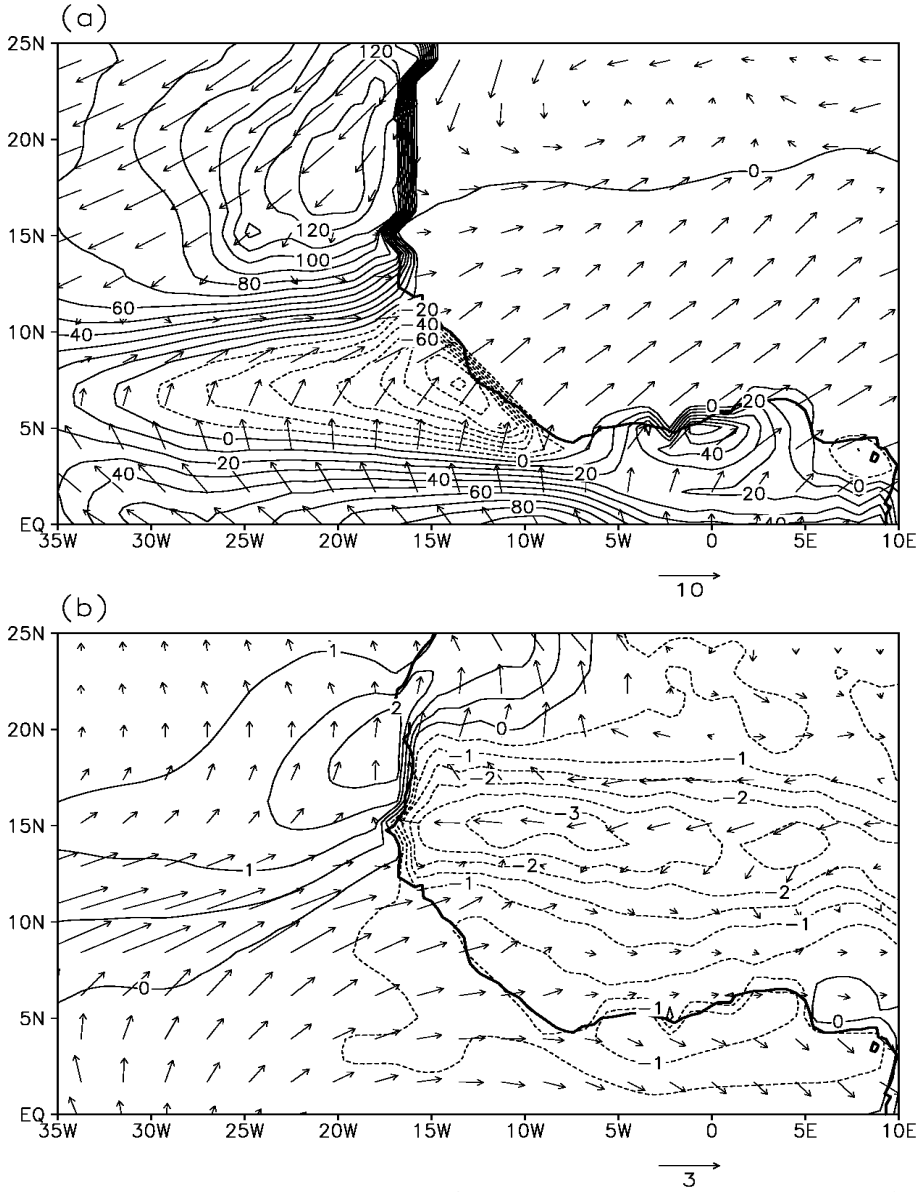

Figure 1.11 (a) Net surface heating (W m^{-2}) and 925 hPa wind vectors (m s^{-1}) from the ERA40 reanalysis during the WAWJ's mature stage (Stage 3). (b) Skin temperature (K) and 925 hPa winds differences for (Stage 3)-(Stage 2). Contour intervals are 10 W m^{-2} in Fig. 11a and 0.5 K in Fig. 1.11b.

Each component of the surface heat budget is examined for the time of the jet maximum (Stage 3). Figure 12a displays the net solar radiative heat flux. As shown in Fig. 1.12a, a solar heating center of 260 Wm^{-2} is located at 14°-25°N over the eastern Atlantic (extending northward to about 29°N, not shown). To the south, solar heating rates are much lower, with a minimum of 60 Wm^{-2} at 6°-11°N on the coast. So the pattern of surface heating to the north and cooling to the south seen in the net surface heat balance that advances the warm coastal SSTs northward from Stage 2 to Stage 3 is supported by the net surface solar radiation.

In addition to the distribution of solar heating, the pattern of latent cooling in the eastern Atlantic helps drive the northward shift of the SST maximum off the west coast of Africa. As seen in Fig. 1.12b, the evaporative cooling of the surface is minimal at 12°-18°N along the coast, and much stronger to the south with a maximum at 2°-7°N.

The net longwave radiative and sensible heat fluxes (not shown) are relatively uniform between 12°N and 22°N over the eastern Atlantic, so they do not play a primary role in moving the coast SST maximum to the north between Stages 2 and 3. It is the sum of the solar and latent heat fluxes (Figs. 1.12a and b) that produces the pattern of heating to the north and cooling to the south along the coast shown in Fig. 1.11a, and that moves the SST maximum northward between Stages 2 and 3 of the jet.

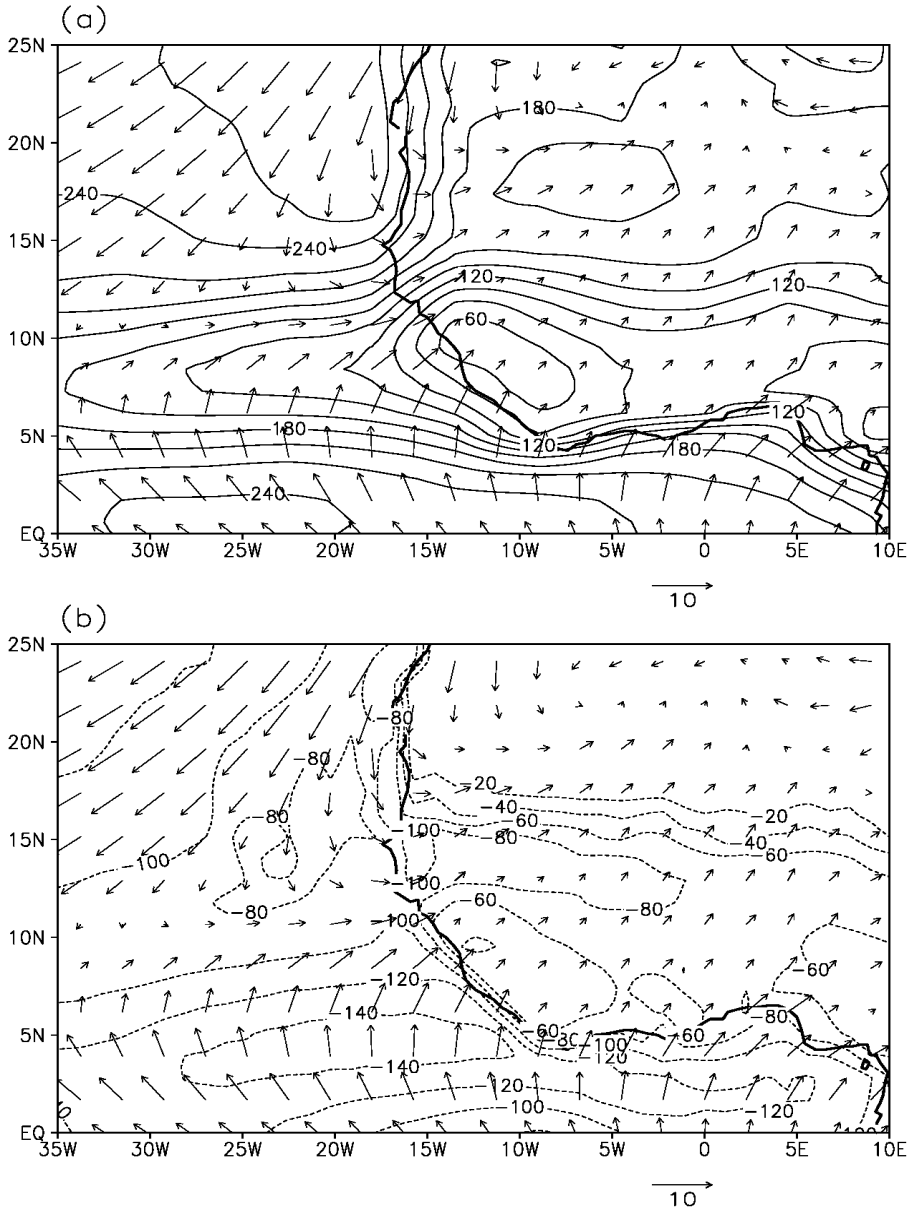

Figure 1.12 (a) Downward solar radiation and (b) upward latent heating flux averaged between July 22nd and Sept 5th for the jet maximum period (W m^{-2}). Positive values denote downward heat flux (surface heating), while negative values denote upward heat flux (surface cooling). Vectors are winds at 10 meters. Contour intervals are 20 W m^{-2}.

An examination of cloud distributions helps relate the surface heating pattern to the movement of the ITCZ and, thereby, the dynamics discussed in the previous section. Figure 1.13a shows total cloud cover from the ERA40 climatology (1958-

2001) for Stage 3. Between 15°-24°W and 16°-25°N, the cloud fraction is 0.4 or lower, allowing relatively high amounts of solar radiation to reach the surface (Fig. 1.12a). The cloud cover fraction is even lower over the Sahara, but the surface albedo is much higher than over the ocean (0.3-0.4 compared with 0.05-0.1) so the solar heating is centered over the ocean. The low solar heating of the surface at 4°-12°N (Fig. 1.12a) is related to the higher cloud covers of the ITCZ region (Fig. 1.13a).

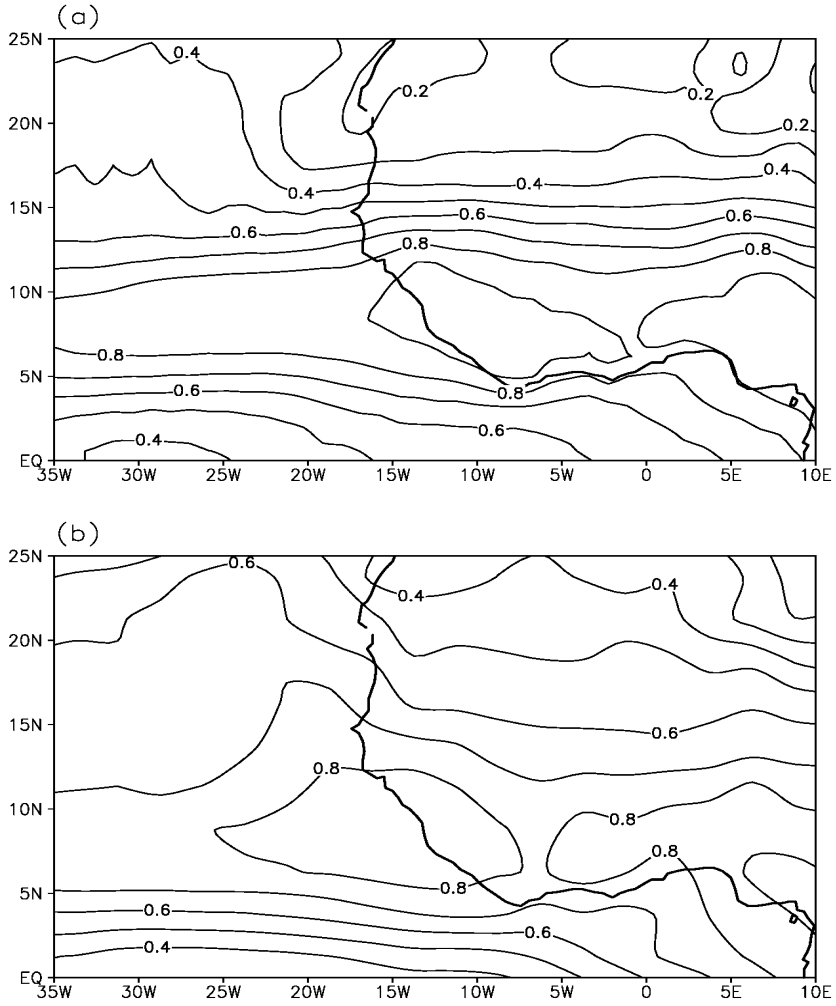

Figure 1.13 Total cloud cover (fraction) in (a) the ERA40 climatology (1958-2001) for the WAWJ mature stage (Stage 3) and (b) the ISCCP climatology (1984-2007) for August.

Since cloud cover in the reanalysis is not assimilated, satellite measurements from the International Satellite Cloud Climatology Project (ISCCP, http://isccp.giss.nasa.gov; Rossow and Shiffer 1999) climatology (1984-2007) for August are used to validate the cloud distribution shown in Fig. 1.13a. As shown in Fig. 1.13b, the mean cloud cover distribution in the ISCCP climatology is similar to that in the ERA40 reanalysis, with a minimum between 20°N and 25°N on the continent that extends westward over the eastern Atlantic. These low cloud amounts over the coastal eastern Atlantic are related to the low-level inversion (at 17°-25°N, not shown) associated with the westward advection of the dry and warm Saharan air (i.e., the Saharan air layer), which suppresses deep convection (Wong and Dessler 2005). The ISCCP cloud data also confirm the high cloud amounts between 5°N and 12°N associated with the ITCZ.

The pattern of latent cooling of the surface is also related to the seasonal movement of the ITCZ through the surface winds. The cooling maximum at 2-7°N is associated with strong surface winds to the south of the ITCZ, while the minimum in the north is associated with the low wind speeds in the offshore low to the north of the WAWJ. As the offshore low develops, the surface winds weaken and latent heat loss decreases, which tends to warm SSTs and deepen the low.

Surface heat budgets in different stages (not shown) reveal a similar association between the net surface heating and SST warming. From early June to mid-October (Stages 1-5), the net surface heating center is located at 19°N, 20°N, 19°N, 17°N, and 13°N, respectively, with a net cooling center associated with the ITCZ to the south.

Grodsky et al. (2003) also discuss the relationship between the WAWJ and SSTs, demonstrating that the presence of the jets causes a cooling of SSTs through Ekman pumping and latent heat loss. They find that these two processes cool eastern

Atlantic SSTs in August by about 0.35 K, when the westerly wind speed is 2 m s^{-1} stronger between a strong jet year (1999) and a weak jet year (2000). This cooling effect is quite local, and has only a small effect on the larger-scale surface heat balances discussed here.

1.6 Conclusions

The climatology and dynamics of the West African westerly jet (WAWJ) are studied in the relatively high-resolution (about 1.125° latitude by 1.125° longitude) ERA40 reanalysis. This work builds upon the observational analysis of Grodsky et al. (2003), who first identify the westerly flow onto the continent near 10°N as a jet using QuikSCAT data. The work is further motivated by the results of Patricola and Cook (2007, 2008) who find that the WAWJ plays a crucial role in moisture transport into the Sahel, and that the jet can vary independently of the southwesterly monsoon flow. Here we show that the structure and dynamics of the WAWJ and the southwesterly monsoon flow are distinct, and study the processes that cause the jet to form.

The WAWJ develops at the beginning of June, reaches a maximum intensity of 6 m s^{-1} at 925 hPa during August, and dissipates in mid-October. Based on the strength of the zonal wind speed in the ERA40 climatology (1958-2001), five stages of jet development are identified. At its mature stage, July 22nd – September 5th, the jet extends between 12°-30°W and 8°-11°N, and from the surface to 700 hPa.

In the 6-hourly ERA40 reanalysis, the jet displays a weak semidiurnal cycle, with two wind speed maxima of 5-6 m s^{-1} at 5 AM and 5 PM local time and minima of 4-5 m s^{-1} at 11 AM and 11 PM local time.

The formation of the WAWJ depends on multi-scale interactions. Over the eastern Atlantic, a region of enhanced westerly acceleration forms when the seasonal progression of the continental low is superimposed on the seasonal progression of the

Atlantic marine ITCZ. While the pressure gradient force in the relatively small region between 9°-10°N and 20°-30°W accelerates the zonal wind to the east, the superposition of the large-scale meridional convergence associated with the ITCZ constrains the development of meridional acceleration. In this way, the regional-scale WAWJ is coupled to large-scale processes.

Analysis of the momentum budget shows that the mature WAWJ is super-geostrophic. A westerly ageostrophic wind component develops as the southerly flow adds to eastward acceleration via the Coriolis term. The ageostrophic wind contributes up to 40% of the total wind during Stage 2 and Stage 4, e.g., mid-July and from early to mid-September.

The geostrophic zonal wind explains much of the WAWJ's seasonal variation. The meridional pressure gradient at 8°N-13°N associated with the geostrophic wind is influenced by the westward extension of the continental thermal low, which in the ERA40 reanalysis is related to the formation of an offshore low over the eastern Atlantic.

The surface heat budget analysis reveals that the development of the offshore low is related to seasonal SST warming in the eastern Atlantic, a response to the net surface heating. From early June to mid-October, a net surface heating pattern with warming at 8°-25°N and cooling to the south at 4°-8°N persists over the eastern Atlantic between 10°W and 35°W. As the magnitude of this heating pattern varies, SSTs between 6°N and 18°N vary, with a coastal SST maximum moving northward and southward. The offshore low at 1000hPa is co-located with this coastal SST maximum. In Stage 3, when coastal SSTs strongly warm and the thermal low is deep, the westward extension of the low reaches its maximum, with the strongest southward geopotential height gradient setting up in the jet region.

The net surface heat pattern mainly reflects the distribution of the solar

radiative and latent heat fluxes. The solar radiation maximum over the eastern Atlantic is associated with low cloud amounts at 16°-25°N in the coastal region where there is a low-level inversion that prohibits strong convection (Wong and Dessler 2005), and the minimum to the south is related to high cloud amounts in the ITCZ. The weak surface wind speeds in the offshore low and strong wind speeds to the south of the ITCZ are associated with the latent cooling minimum to the north and maximum to the south, respectively.

In summary, the Atlantic ITCZ plays an important role in the WAWJ formation. The ITCZ favors formation of a purely westerly acceleration zone, and thus is dynamically associated with the jet formation. The ITCZ is also thermally related to the WAWJ formation through the surface heat budget and the formation of the offshore low.

Previous studies discuss the importance of westerly flow over the eastern Atlantic and West Africa without distinguishing the WAWJ from the southwesterly monsoon flow. Here we demonstrate that the WAWJ is a feature distinct from the monsoon flow.

First, the geographical locations of the two are different. The WAWJ is located over the eastern Atlantic and the West African coast, while the monsoon westerlies are mainly over the West African continent. In the summer, the jet is centered between 8°N and 11°N (Figs. 1.1a and 1.3a), and the monsoon westerlies extend inland to 20°N (Figs. 1.1a and 1.3b).

The vertical wind in the jet region is up to 10 times greater than that in the monsoon region from late July to early September. While the meridional wind in the monsoon region is 2-3 m s^{-1} stronger than in the WAWJ region, the maximum zonal wind in is about 2 m s^{-1} weaker (Fig. 1.5). The diurnal cycle of the monsoon westerly flow, which has a peak at 6 AM local time and a minimum at 6 PM, is also

distinguished from the semidiurnal cycle of the WAWJ (Fig. 1.4).

The monsoon dynamics is also different from that of the WAWJ. In the monsoon region, momentum balance is achieved among the pressure gradient force, Coriolis force, and a strong friction term, and the flow is sub-geostrophic. The formation of the West African monsoon is essentially related to the heat capacity differences between the West African continent and the Atlantic, which is associated with large-scale land/sea pressure gradients at low levels and the seasonal migration of the southerly trades. Thus, the monsoon development is directly related to the strength of the continental thermal low, and both peak earlier in the year than the WAWJ (Figs. 1.2b and 1.5b). In contrast, the WAWJ is more closely related to the westward extension of the thermal low as well as the seasonal progression of the marine ITCZ over the eastern Atlantic.

REFERENCES

Allan R. P., M.A. Ringer, J. A. Pamment, and A. Slingo, 2004: Simulation of the Earth's radiation budget by the European Center for Medium-Range Weather Forecasts 40-year reanalysis (ERA40), *J. Geophys. Res.,* **109**, D18107, doi:10.1029/2004JD004816.

Braconnot, P., S. Joussaume, N. de Noblet, and G. Ramstein, 2000: Mid-Holocene and Last Glacial Maximum African monsoon changes as simulated within the Paleoclimate Modeling Intercomparison Project. *Global Planet. Change,* **26,** 51–66.

Cadet, D. L., and N. O. Nnoli, 1987: Water vapor transport over Africa and the Atlantic Ocean during summer 1979. *Q. J. R. Meteorol. Soc.*, **113**, 581-602.

Cook, K. H., 1999: Generation of the African easterly jet and its role in determining West African precipitation. *J. Climate*, **12**, 1165-1184.

Druyan, L. M., and R. D. Koster, 1989: Sources of Sahel precipitation for simulated drought and rainy seasons. *J. Climate.*, **2**, 1438-1446.

Grist, J. P., and S. E. Nicholson, 2001: A study of the dynamic factors influencing the rainfall variability in the West African Sahel. *J. Climate*, **14**, 1337-1359.

Grodsky, S. A., J. A. Carton and S. Nigam, 2003: Near surface westerly wind jet in the Atlantic ITCZ. *Geophys. Res. Lett.*, **30(19)**, 2009, doi: 10.1029/2003GL017867.

Gu, G., and R. F. Adler, 2004: Seasonal evolution and variability associated with the west African monsoon system. *J. Climate*, **17**, 3364-3377.

Fontaine, B., P. Roucou, and S. Trzaska, 2003: Atmospheric water cycle and moisture fluxes in the West African monsoon: mean annual cycles and relationship using NCEP/NCAR reanalysis. *Geophys. Res. Lett.*, **30(3)**, 1117, doi:10.1029/2002GL015834.

Hagos, S. M., and K. H. Cook, 2005: Influence of surface processes over Africa on the

Atlantic marine ITCZ and South American precipitation. *J. Climate.*, **18**, 4993-5010.

Hagos, S. M., and K. H. Cook, 2008: Ocean warming and late 20th century Sahel drought and recovery. *J. Climate.*, **21,** 3797–3814.

Jury, M. R., D. B. Enfield, and J.-L. Melice, 2002: Tropical monsoons around Africa: Stability of El Nino-Southern Oscillation associations and links with continental climate. *J. Geophys. Res.*, **107(C10)**, 3151, doi:10.1029/2000JC000507.

Kalnay, E., M. Kanamitsu, R. Kistler, et al., 1996: The NCEP/NCAR 40-year reanalysis project. *Bull. Amer. Meteorol. Soc.*, **77**, 437– 471.

Kanamitsu, M., W. Ebisuzaki, J. Woollen, S. Yang, J. Hnilo, M. Fiorino, and G. Potter, 2002: NCEP-DOE AMIP-II reanalysis. *Bull. Amer. Meteorol. Soc.*, **83**, 1631-1643.

Koster, R. J. Jouzel, R. Suozzo, G. Russell, W. Broecker, D. Rind, and P. Eagleson, 1986: Global source of local precipitation as determined by the NASA/GISS GCM. *Geophys. Res. Lett.*, **13**, 121-124.

Lamb, P. J., 1983: West African water vapor variations between recent contrasting sub-Saharan rainy seasons. *Tellus,* **35,** 198–212.

Nicholson, S. E., and J. P. Grist, 2003: The seasonal evolution of the atmospheric circulation over West Africa and equatorial Africa. *J. Climate.*, **16**, 1013-1030.

Patricola, C. M., and K. H. Cook, 2007: Dynamics of the West African monsoon under mid-Holocene processional forcing: Regional climate model simulations. *J. Climate*, **20**, 694-716.

Patricola, C. M., and K. H. Cook, 2008: Atmosphere/vegetation feedbacks: A mechanism for abrupt climate change over northern Africa. *J. Geophys. Res*., **113**, D18102, doi: 10.1029/2007JD009608.

Rossow, W. B., and R. A. Schiffer, 1999: Advances in understanding clouds from

ISCCP. *Bull. Amer. Meteor. Soc.*, **80**, 2261-2288. The ISCCP D2 data/images were obtained from the International Satellite Cloud Climatology Project web site http://isccp.giss.nasa.gov maintained by the ISCCP research group at the NASA Goddard Institute for Space Studies, New York, NY, January, 2005.

Sijikumar, S., P. Roucou, and B. Fontaine, 2006: Monsoon onset over Sudan-Sahel: simulation by the regional scale model MM5. *Geophys. Res. Lett.*, **33**, L03814, doi:10.1029/2005GL024819.

Simmons, A., S. Uppala, D. Dee, and S. Kobayashi, 2007a: ERA-Interim: New ECMWF reanalysis products from 1989 onwards. *ECMWF Newsletter No.110*, 25-35.

Simmons, A., S. Uppala, and D. Dee, 2007b: Update on ERA-Interim. *ECMWF Newsletter No. 111*, 5.

Tomas, R. A., and P. J. Webster, 1997: The role of inertial instability in determining the location and strength of near-equatorial convection. *Q. J. R. Meteorol. Soc.*, **123**, 1445-1482.

Uppala, S. M., P. W. Kallberg, A.J. Simmons, et al., 2005: The ERA-40 re-analysis, *Q. J. R. Meteorol. Soc.*, **131**, 2961–3012, doi:10.1256/qj.04.176.

UCAR/NCAR/CISL/DSS and ECMWF, 2005: ERA40 T106 Analysis Fields on Pressure Surfaces, and ERA40 T106 6-hourly Surface Analysis and Surface Forecast Fields, created at NCAR. *Published by the CISL Data Support Section at the National Center for Atmospheric Research, Boulder, CO* (ds127.1 and ds 127.0).

Wong, S., and A. E. Dessler, 2005: Suppression of deep convection over the tropical North Atlantic by the Saharan air layer. *Geophys. Res. Lett.*, **32**, L09808, doi:10.1029/2004GL022295.

CHAPTER 2

ROLE OF THE WEST AFRICAN WESTERLY JET IN SAHEL RAINFALL VARIATIONS

2.1 Introduction

Two low-level westerly flow regimes are important for moisture transport into West Africa. One is the well-known West African monsoon (WAM) flow, which is formed by the westward acceleration of the onshore flow across the Guinean coast. The other is the westerly flow near 10°N, directed from the eastern Atlantic onto the West African coast. Grodsky et al. (2003) first identified this westerly flow as a jet using high-resolution scatterometer measurements and studied its dynamics. Pu and Cook (2010; hereafter PC2010) called this jet the West African westerly jet (WAWJ). They studied the mechanisms of the jet's formation, and distinguished its features and dynamics from the WAM flow. Here we advance our understanding of the WAWJ by studying how it is related to Sahel rainfall variability on interannual and decadal scales, and by comparing the moisture transport associated with the jet with that of the monsoon flow.

Relevant literature is reviewed in the following section, with an emphasis on our current understanding of the moisture transport that supports Sahel rainfall and the WAWJ. Section 2.3 describes the datasets and analysis methods used. Results are presented in section 2.4, and section 2.5 summarizes the conclusions.

2.2 Background

A number of authors have investigated the ways in which moisture is transported into West Africa. Studies that identify moisture transport associated with

the zonal flow are particularly relevant to our focus on the WAWJ. For example, Kidson (1977) suggested that the westerly flow to the south of the 850 hPa trough (around 8°N) is an important low-level moisture source for Sahel rainfall. Cadet and Nnoli (1987), in a case study for May through mid-September of 1979, identified a strong westerly moisture flux from the eastern Atlantic below 850 hPa that develops in early June near 5°N. They report that, in August, the moisture flux maximum is located near 10°N in association with a westerly wind maximum.

In the middle troposphere (700-500 hPa), a strong easterly moisture flux associated with the African Easterly jet (AEJ) centered near 15°N advects moisture from eastern and central Africa to the west. Cook (1999) found that moisture divergence between 600 hPa and 800 hPa over West Africa is associated with this jet.

Druyan and Koster (1989) compared various water vapor fluxes into West Africa in the GISS climate model. They found that westerly water vapor transport from the tropical North Atlantic Ocean is the largest moisture supply for rainfall in the western Sahel, while southwesterly moisture transport from the Gulf of Guinea contributes the most to the central Sahel.

These studies of westerly moisture transport into Sahelian West Africa do not specifically address the role of the WAWJ because it was only identified as a jet recently, and it was not previously distinguished from the (south)westerly monsoon flow. Building on the identification of the jet by Grodsky et al. (2003), PC2010 studied the dynamics of the jet in various reanalyses. They showed that the WAWJ is clearly distinguished from the monsoon westerly flow in terms of its structure, seasonal cycle, and dynamics. The jet develops when a region of westerly acceleration forms by the superposition of the Atlantic marine ITCZ and the westward extension of the continental thermal low in their seasonal progressions. The extension of the thermal low is associated with the formation of an offshore low which is related to the

seasonal warming of coastal SSTs between 6°N and 18°N. In August, when the coastal SST strongly warms and the thermal low is deep, the westward extension reaches a maximum and the WAWJ peaks.

A number of studies relate variations in moisture transport with variations in Sahel rainfall. For example, Fontaine et al. (2003) studied moisture fluxes over the West African monsoon region (5°-20°N, 18°W-18°E) from 1968-1998. They found that there are stronger westerly fluxes (between 5°N-15°N) from the northern tropical Atlantic into West Africa in wet years, along with enhanced moisture fluxes from the Mediterranean Sea into the northern Sahel.

Using a regional climate model, Hagos and Cook (2008) studied the influence of Indian and Atlantic Ocean SSTAs on Sahel precipitation in the late 20th century. Warming in the Indian Ocean in the 1980s forced subsidence over central Africa and anomalous anticyclonic circulations over the west coast, which drives moisture away from the Sahel. During the 1990s, the region of subsidence moved to the west as the scale of the Indian Ocean warming increased, and Sahel rainfall increased. Cyclonic circulation associated with warm SSTAs in the northern tropical Atlantic Ocean further enhanced moisture transport into the Sahel to support the rainfall recovery.

Gu and Adler (2004) suggested that when moisture transport from the Gulf of Guinea is reduced due to the development of the Atlantic cold tongue in summer, water vapor transported by the westerly flow between 10°W and 10°E at 850 hPa can influence rainfall along 10°N over West Africa.

These studies, and others, associate variations in Sahel precipitation and westerly moisture transport, but they do not distinguish the WAWJ from the monsoon westerlies. Only a few recent studies discuss this association. Grodsky et al. (2003) found there is a “substantial relationship” between the amplitude of the WAWJ and the Western Sahel Rainfall Index (WSRI; Lamb 1983). The correlation between the

time series of the first EOF of August zonal winds averaged at 10°-30°W and the WSRI is significant from 1949 to 2001.

Patricola and Cook (2007) simulated the precipitation of the African Humid Period (AHP) by applying specified land surface conditions and summer insolation in a regional model. They found that the simulated monsoon flow across the Guinean coast in the AHP case is similar to that of the present day, but the WAWJ is much stronger and deeper. The enhanced WAWJ together with the elimination of the African easterly jet supports the wetness of the Sahel and Sahara. The inability of global models to capture the WAWJ may explain their difficulties in simulating a sufficiently-wet AHP.

Patricola and Cook (2008) identified an atmosphere/vegetation feedback mechanism that may contribute to the propensity for abrupt climate change over northern Africa. They found that when a coupled atmosphere/vegetation regional model is initialized with the southern border of the Sahel north (south) of 17.9°N, a green (dry) Sahara solution results. There was no difference in the southwesterly monsoon flow across the Guinean coast between the dry (present day) and "green Sahara" climate states. Rather, an intensification of the WAWJ provided the critical moisture transport into the northern Sahel and Sahara.

The purpose of this paper is to investigate the relationship between variations in the WAWJ and Sahel rainfall on interannual and decadal time scales.

2.3 Methodology

Climatological Sahel precipitation is greatest in August (Kidson 1977; Long et al. 2000), essentially coincident with the late July to early September maximum in the WAWJ speed (PC2010). So this study of interannual to decadal variability is focused on the month of August.

Reanalysis products are used to examine features of the circulation. The ERA40 reanalysis (Uppala et al. 2005; UCAR/NCAR/CISL/DSS and ECMWF, 2005; T106, about 1.125° latitude by 1.125° longitude) is analyzed for 1958-2002, and the ERA-Interim reanalysis (Simmons et al. 2007a, b; 1.5° latitude by 1.5° longitude) for 1989-2009. The ECMWF TOGA Global Advanced Operational Spectral Analysis[2] (EC-TOGA; T106) for 1998-2007 is used for recent years. The lower resolution (2.5° latitude by 2.5° longitude) NCEP/NCAR reanalysis (NCEP1; Kalnay et al. 1996) for 1958-2009 and the NCEP/DOE AMIP II reanalysis (NCEP2; Kanamitsu et al. 2002) for 1979-2009 are also used as a comparison.

For precipitation, the CRU ts3.0 (CRU; Mitchell and Jones 2005; 0.5° latitude by 0.5° longitude) station observations for 1958-2006, the satellite-derived Global Precipitation Climatology Project (GPCP; Adler et al. 2003; 2.5° latitude by 2.5° longitude) data for 1979-2009, and the CPC Merged Analysis of Precipitation (CMAP; Xie and Arkin 1996; 2.5° latitude by 2.5° longitude) data for 1979-2009 are used.

Multiple datasets are used for several reasons. First is that the Sahel has a relatively low density of station observations to constrain the reanalyses. Also, longer time series may have uncertainties due to changes of observing stations or data processing methods. Cross-validation among datasets provides an estimate of these uncertainties. In addition, since some reanalyses do not extend to the present, e.g., the ERA40 reanalysis ends in August 2002, we examine comparable reanalyses to include recent years.

To characterize the strength of the WAWJ, a "WAWJ index" is defined as the area average of the August 925 hPa zonal wind speed for 8.4°-10.6°N and 15°-25°W.

[2] European Centre for Medium-Range Weather Forecasts, updated yearly: ECMWF TOGA Global Advanced Operational Spectral Analysis, daily 1985-cont. Dataset ds111.0 published by the CISL Data Support Section at the National Center for Atmospheric Research, Boulder, CO, available online at http://dss.ucar.edu/datasets/ds111.0/.

This averaging region is chosen to capture the maximum westerly wind (see Fig. 3a in PC2010). A "WAM index" is used to characterize the strength of the monsoon flow. It is defined as the 925 hPa wind speed averaged between 5°W-5°E and 5.0°-7.3°N in August. The monsoon averaging region has the same number of grid point as the jet region, and it captures both the maximum westerly and southerly wind speeds over the Guinean coast.

2.4 Results

a. Correlations between the WAWJ and precipitation

Figure 2.1 shows the time series of the WAWJ index from various reanalyses. Means and standard deviations of the indices are listed in Table 2.1. While the jet indices from the different reanalyses have similar interannual variations, the strength varies. The mean jet index ranges from 3.4 m s^{-1} in the NCEP2 reanalysis to 5.0 m s^{-1} in the ERA40 reanalysis. The NCEP1 jet index is greater than the ERA40 jet index for 1958-1963, smaller for 1963-2000, and again greater for 2001-2002. The magnitude of the NCEP2 jet index is very similar to the NCEP1 jet index for 1979-1990, 1-2 m s^{-1} weaker than the NCEP1 jet index for 1991-2000, and 2-3 m s^{-1} weaker for 2001-2009. The magnitude of the ERA-Interim jet index resembles the NCEP1 jet index for 1989-2000, and is 0.5-1 m s^{-1} weaker for 2001-2009. The jet index in the EC-TOGA analysis lies between the ERA-Interim and NCEP2 jet indices. The standard deviation is highest in the NCEP1 reanalysis and lowest in the ERA-Interim reanalysis.

Many factors can contribute to differences among the reanalyses, e.g., different sources of observations, physical parameterizations used in models, and assimilation methods. Lack of observations in West Africa might also be important. As a comparison, we examined 925 hPa zonal wind speeds in regions with significantly more observations, e.g., North America and Europe. The differences among the

reanalyses are very small in these regions, while in other regions with sparse observations, e.g., South America, the differences are large (not shown).

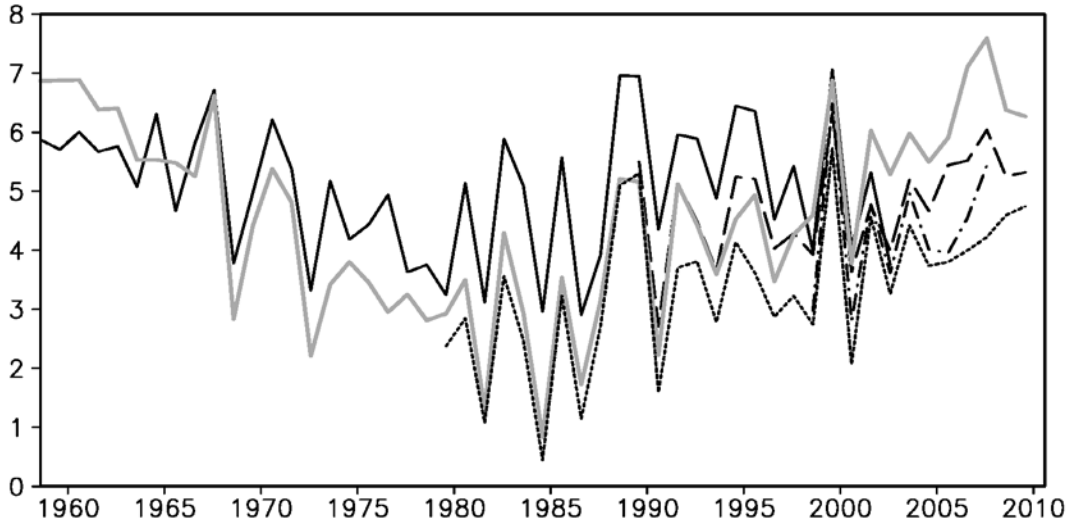

Figure 2.1 WAWJ indices (m s^{-1}) from the ERA40 (black solid line), ERA-Interim (black long dashed line), NCEP1 (solid grey line), and NCEP2 (black short dashed line) reanalyses, and the EC-TOGA (dot-dash line) analyses. All are interpolated to a 1.5° grid.

Table 2.1 Means and standard deviations (σ) of jet indices (m s^{-1}) from various reanalyses.

Reanalyses	Time	Mean (σ)
ERA-40	1958 - 2002	5.0 (1.2)
ERA-Interim	1989 –2009	4.8 (0.9)
EC-TOGA	1998 –2007	4.4 (1.1)
NCEP1	1958 –2009	4.6 (1.6)
NCEP2	1979 –2009	3.4 (1.3)

Despite the uncertainties and differences among the reanalysis products, Fig. 2.1 demonstrates that, there are common features. Correlations among the WAWJ indices are displayed in Table 2.2, and all pass the 99% confidence level. This suggests that the reanalyses are useful for examining the WAWJ, but with some caution. Considering the small scale of the WAWJ, the high resolution ERA40 reanalysis for 1958-2002 and the ERA-Interim reanalysis for 2003-2009 are used as the primary resources in this paper.

Table 2.2 Correlation coefficients among jet indices from various reanalyses. All exceed the 99% confidence levels.

	ERA-Interim	EC-TOGA	NCEP1	NCEP2
ERA40	$Co_{1989\text{-}2002}$=0.87	-	$Co_{1958\text{-}2002}$=0.76	$Co_{1979\text{-}2002}$=0.89
ERA-Interim	-	$Co_{1998\text{-}2007}$=0.90	$Co_{1989\text{-}2009}$=0.86	$Co_{1989\text{-}2009}$=0.89
EC-TOGA	-	-	$Co_{1998\text{-}2007}$=0.85	$Co_{1998\text{-}2007}$=0.96
NCEP1	-	-	-	$Co_{1979\text{-}2009}$=0.88

To investigate the relationship between the strength of the WAWJ and Sahel rainfall, correlations among all combinations of three reanalyses and three precipitation datasets were calculated (Figure 2.2). Figures 2.2a-c display correlations between the CRU precipitation and the ERA40 (1958-2002), NCEP1 (1958-2006), and NCEP2 (1979-2006) jet indices, respectively, with only correlation coefficients exceeding the 95% confidence levels displayed. In each case, significant positive correlations extend across the Sahel.

When other combinations of precipitation data and reanalysis jet indices are correlated, similar patterns emerge. Figures 2.2d, e, and f show correlations between the CMAP precipitation and the ERA40 (1979-2002), NCEP1 (1979-2009), and

NCEP2 (1979-2009) jet indices, respectively. Figures 2.2g-i display correlations between the GPCP precipitation and jet indices in the three reanalyses. Correlations between the WAWJ indices and Sahel rainfall are robust and consistent across all combinations of data sets.

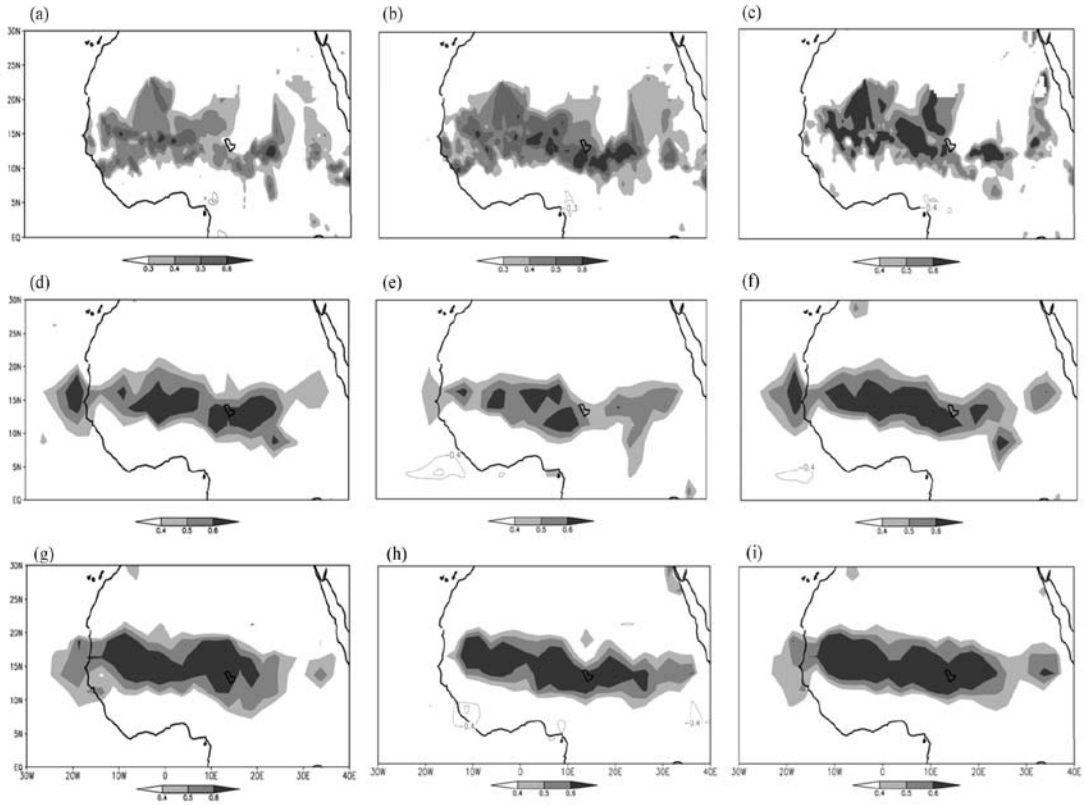

Figure 2.2 Correlations between the WAWJ indices from 3 reanalyses and 3 precipitation datasets. Only correlation coefficients exceeding the 95% confidence levels are shown. Shading denotes positive correlations while contours denote negative correlations with intervals of -0.1. Figs. 2.2a-c are correlations between the CRU precipitation and the ERA40, NCEP1 and NCEP2 jet indices, respectively. Figs. 2.2d-f are correlations between the CMAP precipitation and three jet indices, while Figs. 2.2g-i are correlations between the GPCP precipitation and three jet indices.

We define a Sahel precipitation index based on the correlations shown in Fig. 2.2, averaging August rainfall between the west coast (about 17°W) and 30°E and

between 10°N and 20°N. Because both the ERA40 reanalysis (1958-2002) and CRU precipitation (1901-2005) are not updated to the present, the ERA-Interim reanalysis for 2003-2009 and GPCP data for 2006-2009 are used to extend the jet and Sahel precipitation time series. Using different records to extend the indices may introduce some inconsistency, but including recent information provides a better estimate of decadal variations and trends. Means and deviations of the WAWJ and Sahel precipitation indices from different data sets for the years in which they overlap are listed in Table 2.3 to characterize their differences.

Table 2.3 Means and standard deviations (σ) of the jet indices (m s^{-1}) from the ERA40 and ERA-Interim reanalyses and the Sahel precipitation indices (mm day^{-1}) from the CRU and GPCP observations during their overlap periods.

Datasets	Overlap period	Mean (σ)
ERA40	1989-2002	5.4 (1.1)
ERA-Interim		4.5 (0.9)
CRU	1979-2005	4.4 (0.9)
GPCP		4.4 (0.9)

Figure 2.3a shows the time series of the WAWJ index from the ERA-40 and ERA-Interim reanalyses (solid line) and the Sahel precipitation index from the CRU and GPCP observations (dashed line) from 1958 to 2009. The WAWJ and precipitation indices are highly correlated, with a correlation coefficient of 0.62 that exceeds the 99% confidence level. From the late 1950s through the 1960s, both the WAWJ and Sahel precipitation are relatively strong. From the 1970s to the 1980s, both the jet and the rainfall are weak, with minima in 1984. They both recover in the late 1980s and vary near the climatological average during the 1990s and 2000s.

To isolate the decadal signal, the time series shown in Fig. 2.3a are filtered by

applying a 9-year running mean, and displayed in Fig. 2.3b. Decadal variations of the jet index are similar to the jet variations shown by Grodsky et al. (2003), who examined the time series of the amplitude of the first EOF of the zonal wind in the jet region. Co-variations of the jet and Sahel precipitation indices on decadal time scales are evident. From the 1960s to the 1980s, both the jet and Sahel precipitation indices experienced strong, weak, and recovery periods. In the 1990s, the magnitude of the jet index is similar to that in the 1960s while the Sahel precipitation index is still weaker than its 1960s level. During the 2000s, the jet index is weaker than in the 1990s, while the magnitude of the Sahel rainfall index is very similar to its 1990s level.

Figure 2.3c shows interannual variations of the WAWJ and Sahel precipitation indices, calculated as the full time series (Fig. 2.3a) minus the filtered time series (Fig. 2.3b). Interannual variations of the WAWJ index are also significantly correlated with Sahel precipitation, with a correlation coefficient of 0.63, exceeding the 99% confidence level.

The WAWJ and Sahel rainfall indices are also highly correlated in July and September (not shown). The correlation between the jet index and Sahel rainfall index for July (September) is 0.41 (0.64) for 1958-2009 (1958-2008), exceeding the 99% confidence level.

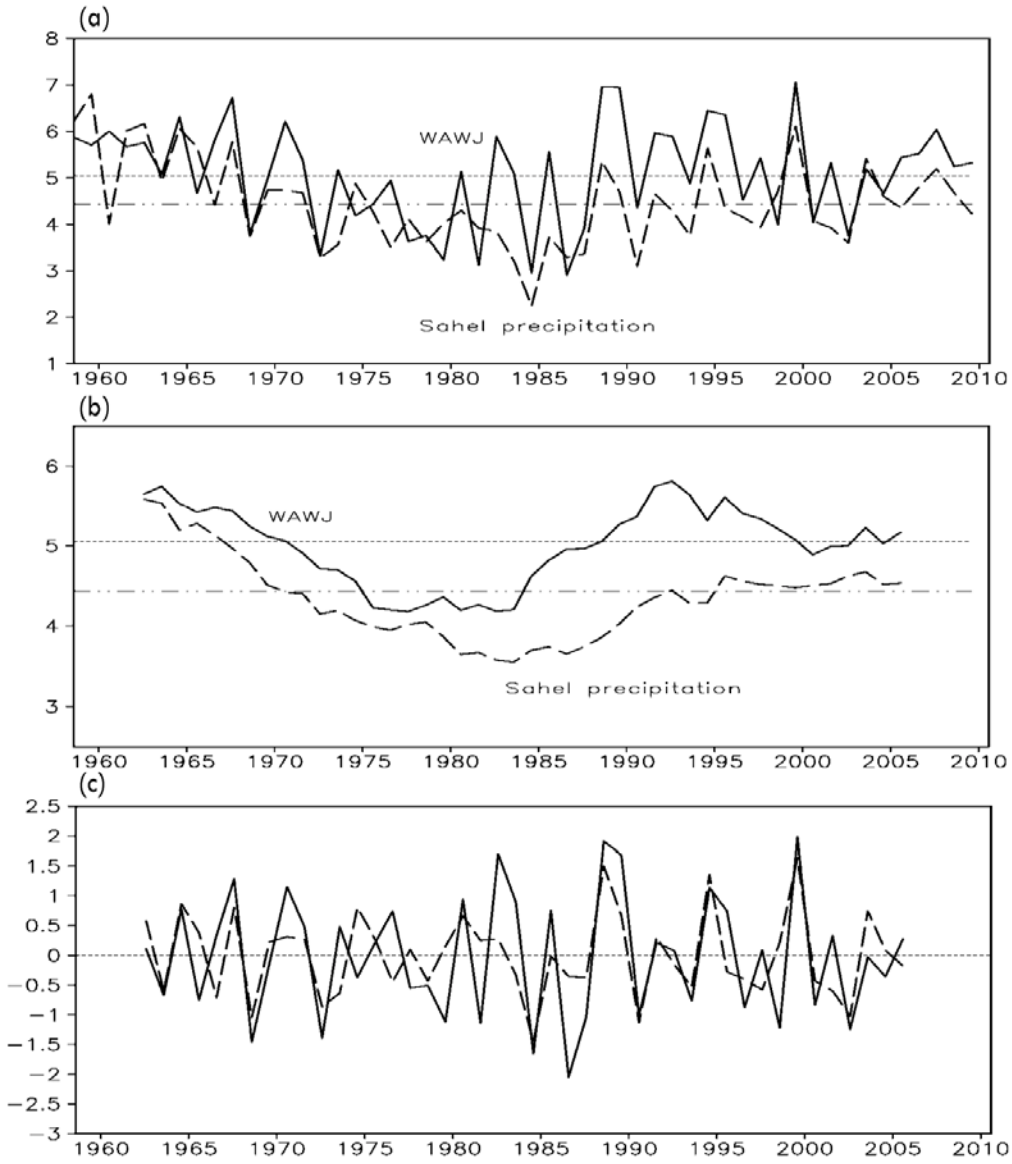

Figure 2.3 (a) The WAWJ (solid) index (m s^{-1}) from the ERA40 reanalysis for 1958-2002 and the ERA-Interim reanalysis for 2003-2009, and the Sahel precipitation (dashed) index (mm day^{-1}) from the CRU data for 1958-2006 and the GPCP data for 2007-2009. (b) Decadal and (c) interannual components of the jet and Sahel precipitation indices. All indices are interpolated to a 1.5° grid. Dashed (dot-dot-dash) lines in (a)-(b) denote the mean of the jet (Sahel precipitation) index for 1958-2002.

b. Relationship between the WAWJ and precipitation on decadal times scales

Based on the decadal-scale co-variations of the WAWJ and Sahel precipitation (Fig. 2.3), three periods are defined, namely, 1958-1971, 1972-1987, and 1988-2009, corresponding to times of a wet Sahel/strong jet, dry Sahel/weak jet, and relatively wet Sahel/strong jet, respectively. The end of a strong (weak) jet period is defined when the anomalies of the jet index reach -0.5 (0.5) standard deviation (σ), and within next 7 years at least 5 years have negative (positive) anomalies and no positive (negative) anomalies greater than 1σ. The same criterion is applied to the Sahel precipitation index to define wet and dry periods. Note that the last period is not a rigid "wet" period based on the criterion above. The number of years with positive precipitation anomalies is the same as the number of years with negative anomalies, but the magnitudes of the positive anomalies are slightly larger than the negative anomalies.

Note that this criterion begins the drought period in 1972, while some previous work defines the Sahel drought from 1968 (Nicholson 1981, Druyan 1989). The different starting years may be related to the different datasets used, different averaging regions, different reference periods when calculating anomalies, or the fact that we only evaluate for August here to clarify the relationship with the WAWJ. Long et al. (2000) note that interannual variations of Sahel precipitation averaged for June-July and for August-September are quite different. Our choice of periods is very similar to that of Long et al. (2000), who defined 1959-1971 and 1972-1989 as wet and dry periods for southern sub-Sahara (about 8°-16°N, see Fig. 1 in Long et al. 2001) for August and September. The following analysis is the same, and the conclusions are not changed, if 1968 is used as the beginning at the dry period.

Figures 2.4a-c show 925 hPa wind vectors, zonal wind speeds (shading), and geopotential heights (contours) averaged over the three periods. Average WAWJ speeds exceed 6 m s^{-1} in the 1958-1971 and 1988-2009 periods (Figs. 2.4a and c,

respectively). The thermal low extends westward over the eastern Atlantic to about 35°W in association with a well-developed offshore low near 15°N that accompanies the formation of the WAWJ (PC2010). In 1972-1987, the jet maximum speed is around 5 m s^{-1}, and the thermal low only extends westward to about 25°W (Fig. 2.4b).

Figure 2.5a shows the August precipitation climatology from the CRU and GPCP data for 1958-2009. There are two maxima over West Africa, one along the west coast between 5°N and 12°N and the other at 10°E and 7°N over the eastern Guinean coast. North of 15°N, precipitation rates fall below 6 mm day^{-1}.

Precipitation anomalies, calculated as differences from the 1958-2009 mean, for the three time periods are displayed in Figs. 2.5b-d. Positive Sahel precipitation anomalies for 1958-1971 range up to 1.25 mm day^{-1} (about 30%), centered between 10°N and 15°N, and extending inland from the west coast to about 26°E (Fig. 2.5b). The Guinean coast region is anomalously dry. A nearly opposite pattern occurs during the second period (1972-1987), with a dry Sahel and relatively wet Guinean coast region (Fig. 2.5c). The anomalies range from -1.5 mm day^{-1} to 1 mm day^{-1} (-30% to 10%). From 1988 to 2009, displayed in Fig. 2.5d, precipitation anomalies are mostly positive, with drying over the western Guinean coast. Sahel precipitation has partially recovered in this recent time period, with positive anomalies about two fifths of the magnitude of the first period.

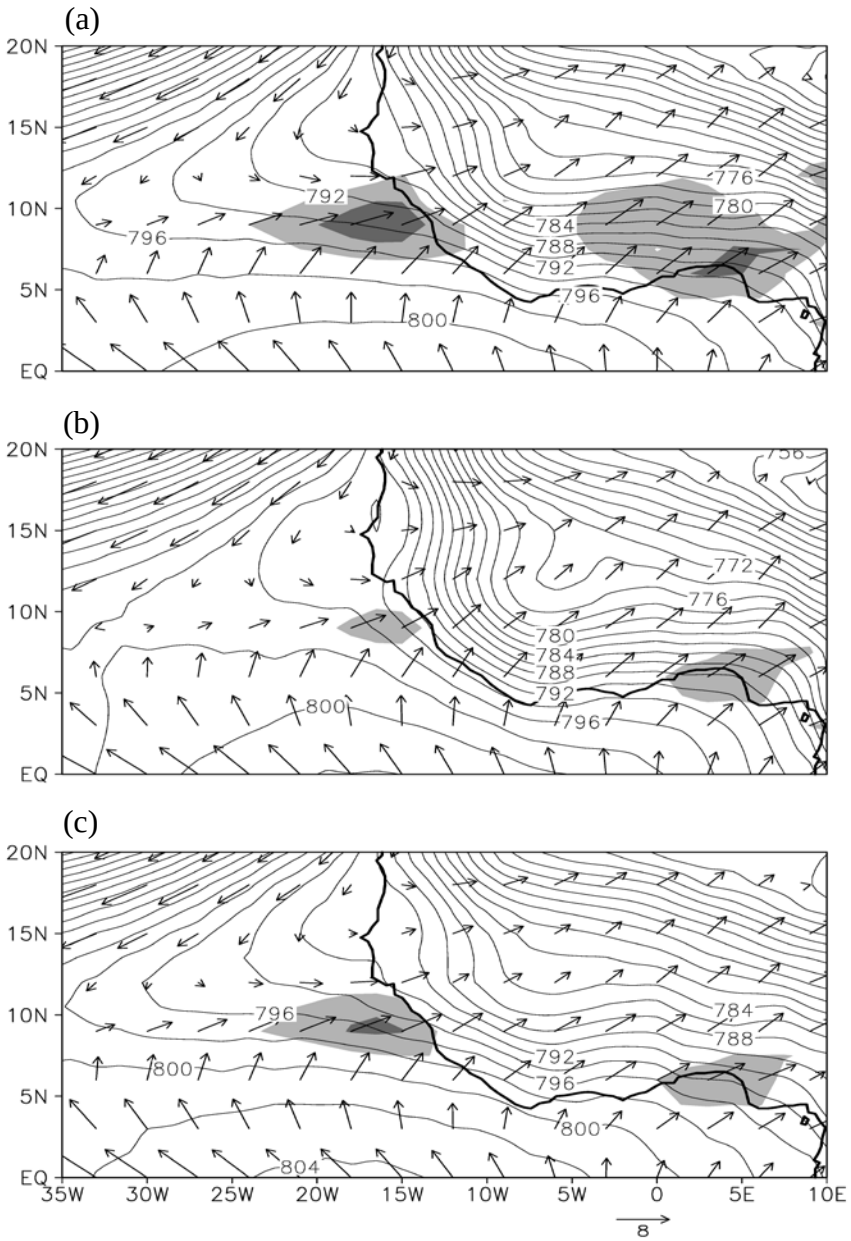

Figure 2.4 925 hPa wind (m s^{-1}) and geopotential heights (gpm; contours) for (a) 1958-1971, (b) 1972-1987, and (c) 1988-2009 from the ERA40 (1958-2002) and ERA-Interim (2003-2009) reanalyses. Westerly winds greater than 5 m s^{-1} (6 m s^{-1}) are shaded with light (dark) gray.

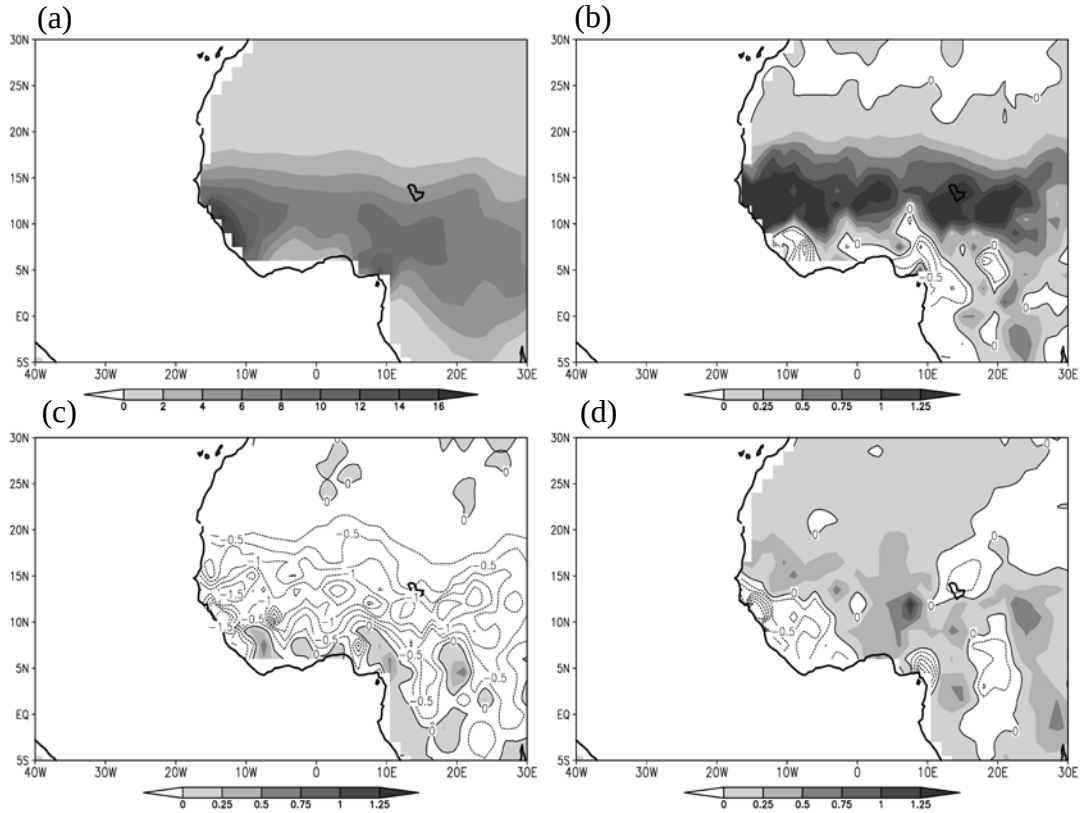

Figure 2.5 (a) Precipitation climatology (1958-2009) and anomalies for (b) 1958-1971, (c) 1972-1987, and (d) 1988-2009 from the CRU (1958-2005) and GPCP (2006-2009) data. Shading denotes positive values while contours denote negative values. Contour intervals are 2 mm day^{-1} in (a) and 0.25 mm day^{-1} in (b)-(d).

To relate decadal precipitation variations to features of the circulation, we examine the vertically-integrated, mass-weighted moisture flux, M, for August as

$$M = -\frac{1}{g}\int_{Ps}^{Ptop}(q\vec{V})dp \approx -\frac{1}{g}\sum_{p=Ps}^{p=10}\left(q\vec{V}\right)\Delta p\,, \qquad (2.1)$$

where q is specific humidity and $\vec{V}$ is the horizontal wind. The integration is from the surface (P_s) to P_{top}=10 hPa, and calculated as a finite sum shown on the right hand side of the equation. As shown in PC 2010, the WAWJ extends from the surface to 700 hPa at its mature stage in the climatology. Further examination of the ERA40

reanalysis shows that in August the monsoon flow occurs primarily below 700 hPa and the AEJ is centered at 600 hPa. This motivates a decomposition of the atmospheric column moisture transport, M, into an integral from the surface to 700 hPa (M_1) and from 700 hPa to 10 hPa (M_2) according to

$$M = M_1 + M_2 \approx -\frac{1}{g}\sum_{p=Ps}^{p=700}\left(q\vec{V}\right)\Delta p - \frac{1}{g}\sum_{p=700}^{p=10}\left(q\vec{V}\right)\Delta p \cdot \qquad (2.2)$$

Figures 2.6a and b show M_1 and M_2 for the 1958-2009 ECMWF reanalysis climatology, respectively. Between the surface and 700 hPa, the primary fluxes of moisture onto the African continent are the westerly flux at 7.5°- 10°N in the vicinity of the WAWJ and the southwesterly flux at 10°W-10°E associated with the monsoon flow across the Guinean coast (Fig. 2.6a). Between 12.5°-15°N and 18°W-5°E, the small easterly fluxes over land are associated with the lower levels of the AEJ. Along the west coast between 20°N and 30°N, a northeasterly flux transports moisture off the coast. Above 700 hPa over land, easterly fluxes associated with the African easterly jet transport moisture off the continent between 10°N and 20°N (Fig. 2.6b).

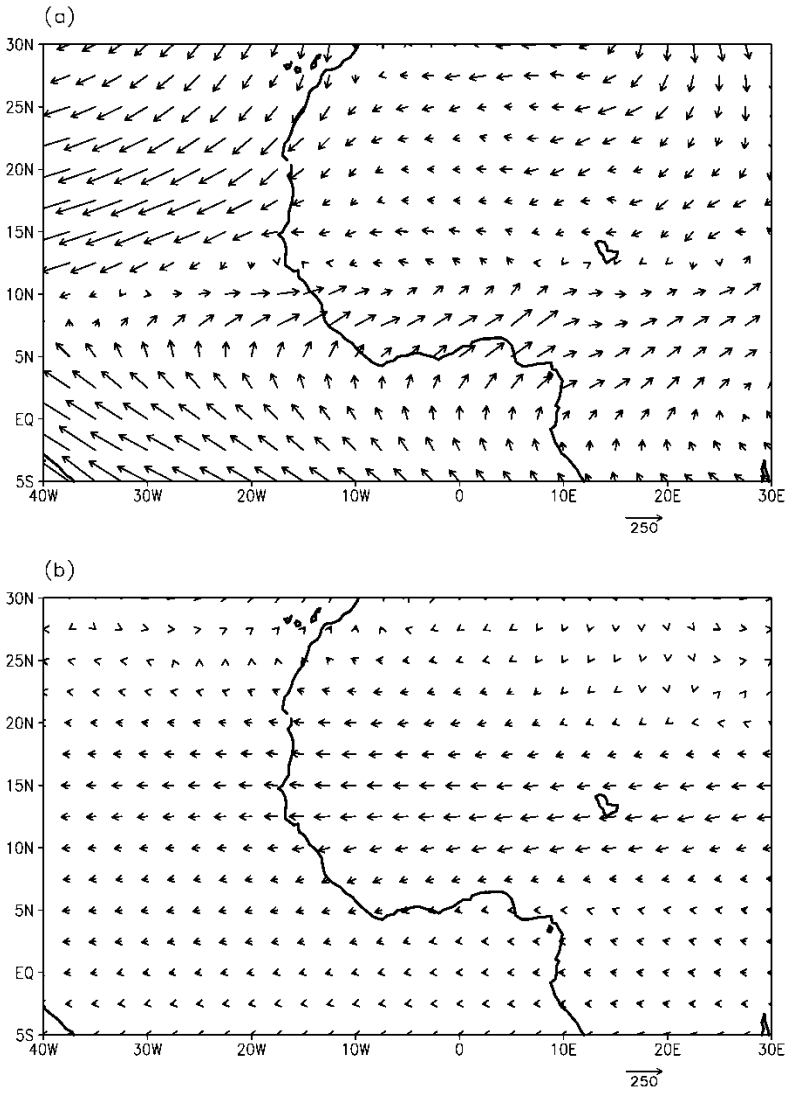

Figure 2.6 Vertically-integrated mass-weighted moisture transport from the ERA40 and ERA-Interim reanalyses for the 1958-2009 climatology, integrated (a) from the surface to 700 hPa and (b) from 700 hPa to 10 hPa. Vector scale indicates the magnitude of the moisture flux in kg $m^{-1}s^{-1}$.

Figures 2.7a-c display anomalies of M_1 (Eq. 2.2) for each time period defined above. These anomalies are very similar in structure to the horizontal wind anomalies, indicating that changes in $\vec{V}$ and not q (Eq. 2.2) are most important.

The role of the enhanced WAWJ in bringing moisture onto the west coast in the 1958-1971 wet period is evident in Fig. 2.7a. Over the eastern Atlantic, an enhanced westerly moisture flux is located between 15°W and 40°W. Anomalous southwesterly moisture flux at 0-10°W associated with the monsoon also transports more moisture from the Gulf of Guinea onto the continent. Over land, an anomalous cyclonic circulation is centered near 20°E and 15°N, and this carries moisture eastward and northward to 20°N.

In the 1972-1987 drought period, the anomalous moisture transport from the eastern Atlantic is negative between 5°-12.5°N and 40°W-5°E (Fig. 2.7b). This is related to the weak WAWJ of this period (Fig. 2.4b). Moisture transport by the monsoon flow over the Guinean coast changes little. Over land, an anomalous northerly moisture flux at 12°E and 5°-15°N brings moisture from the Sahel toward the Guinean coast.

In the 1988-2009 “recovery” period, an anomalous westerly moisture flux associated with a stronger WAWJ is located at 7°-15°N over the eastern Atlantic, enhancing eastward moisture transport toward the continent (Fig. 2.7c). Along the west coast at 10°W, moisture is transported northward to about 18°N. Over the Gulf of Guinea at 5W°-5°E, southwesterly moisture transport associated with the monsoon is decreased.

Anomalies of moisture transport between 700 hPa and 10 hPa (M_2) are quite small (not shown), indicating that changes in moisture transport by the African easterly jet are not strongly correlated with the decadal drought signal.

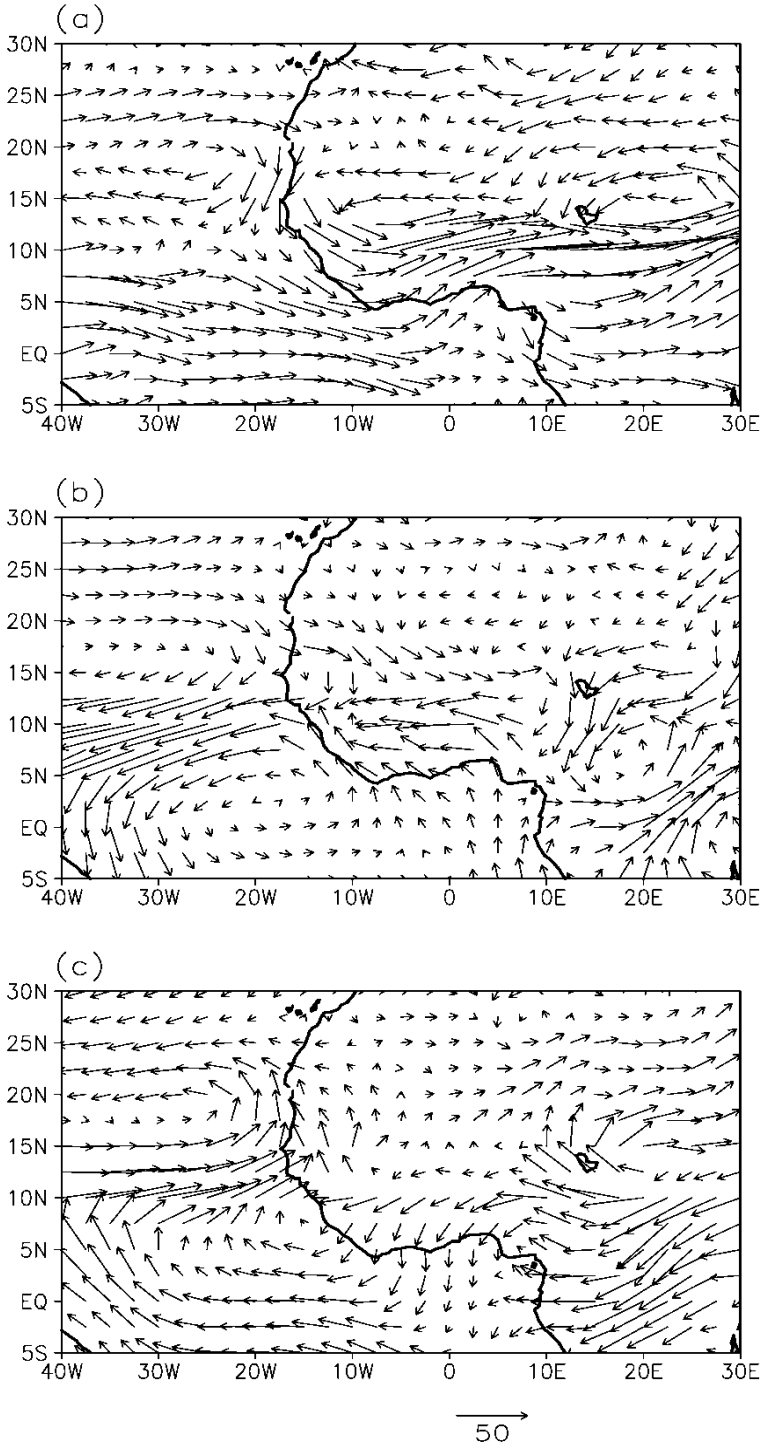

Figure 2.7 Vertically-integrated mass-weighted moisture transport for (a) 1958-1971, (b) 1972-1987, and (c) 1988-2009, integrated from the surface to 700 hPa. Vector scale indicates the magnitude of the moisture flux in kg $m^{-1}s^{-1}$.

The moist static energy (MSE) budget analysis helps to demonstrate the association between the moisture profile and large-scale convective precipitation in the Sahel. MSE is the sum of the sensible, latent and geopotential energy according to

$$MSE = c_p T + Lq + gz \,, \tag{2.3}$$

where c_p is the specific heat of air at constant pressure, T is air temperature, L is the latent heat of vaporization of water, q is specific humidity, g is the acceleration due to gravity, and z is height. MSE increasing with altitude denotes a stable atmosphere, so increases in low-level MSE destabilize the vertical column and promote convection.

Figures 2.8a-c display anomalies of MSE and its component terms (Eq. 2.3) over the Sahel at 18°N and 15°W-30°E, where the anomalies of precipitation (by per cent) are relatively large, for 1958-1971,1972-1987 and 1988-2009, respectively. As shown in Fig. 2.8a, during 1958-1971 the negative slope of MSE anomalies (solid line) below 600 hPa indicates a convectively unstable environment. Increased low-level moisture content (Lq; dashed line) associated with enhanced low-level moisture transport (Fig. 2.7a) destabilizes the lower atmosphere, while decreases in temperature (c_pT; dot-dash line) tend to stabilize the lower troposphere. Anomalies between 500 hPa and 600 hPa act to stabilize the mid-troposphere. Between 250 hPa and 500 hPa, in association with decreases in moisture content at high levels, instability increases again. Changes of geopotential term (gz; dotted line) are negligible.

In the 1972-1987 dry period (Fig. 2.8b), large decreases in moisture content between 700 hPa and 1000 hPa are associated with a more stable MSE profile. Small increases in low-level temperature tend to destabilize the atmosphere, but they are overwhelmed by the moisture anomalies.

During the 1988-2009 recovery, MSE anomalies are relatively small. The anomalous negative slope of the MSE is mainly associated with increases in moisture

content and air temperature below 850 hPa accompanied by decreases in moisture content at 700 hPa. Above 500 hPa, the anomalous MSE slope is positive, indicating that deep convection is discouraged.

Figs. 2.5-2.8 suggest that decadal variations of Sahel precipitation are related to variations of the WAWJ via low-level moisture transport. In periods when the WAWJ is strong, enhanced westerly moisture transport increases the low-level moisture content over the Sahel, and this is associated with decreased vertical stability and precipitation increases.

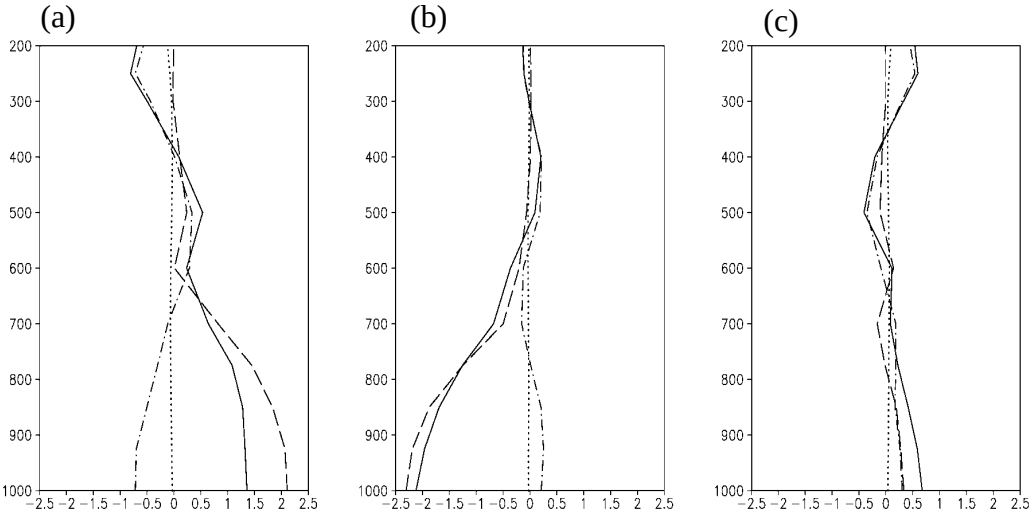

Figure 2.8 Anomalies of moist static energy (MSE) terms (Eq. 2.3) averaged between 15°W and 30°E at 18°N for (a) 1958-1971, (b) 1972-1987, and (c) 1988-2009, with reference to the 1958-2009 mean. Sold lines denote the total MSE, dashed (dot-dash) lines denote the moisture (temperature) term, and dotted lines denote the geopotential term (units: 10^3 m^2 s^{-2}).

This association between the WAWJ and Sahel rainfall on decadal time scales does not necessarily mean that the former is the fundamental cause of the latter. Variations of the WAWJ and westerly moisture transport displayed here may be part of large-scale circulation changes in response to SST variations in the Indian Ocean and tropical Atlantic, which provide forcing of Sahel rainfall variations during the

1980s and 1990s (Hagos and Cook 2008). The close connection between the WAWJ and the local circulation, e.g., the continental thermal low and its westward extension (PC2010), also suggests feedbacks between the precipitation field and land surface conditions through modifications of the WAWJ. Also note that the correlation between the WAWJ index and Sahel rainfall index is 0.62, which suggests that the WAWJ (statistically) explain less than 40% of the Sahel rainfall variance in August. Other factors, e.g., the WAM and local land surface processes, also influence Sahel rainfall.

c. Case studies of the relationship between the WAWJ and Sahel precipitation

To examine the relationship between the WAWJ and Sahel rainfall in individual extreme years, we chose a year from each decadal period defined above when both the anomalies of the jet and Sahel rainfall indices are greater than $\pm 1\sigma$. 1964, 1984, and 1999 are chosen. Because two different reanalyses (observations) are used in the third period, we also examine 2007, when the anomaly of the jet index from the ERA-Interim reanalysis is relatively large, 0.9σ, and the anomaly of the Sahel precipitation index from the GPCP data is about 0.8σ.

Precipitation anomalies for the four years are displayed in Figures 2.9a-d. Anomalously high precipitation extends across the western Sahel, with drying to the south, in 1964 and 1999 (Figs. 2.9a and d, respectively). In 1984, the driest year during 1958-2009 period (Fig. 2.3a), Sahel precipitation anomalies are up to -4 mm day^{-1} (-80 %; Fig. 2.9b). In 2007, the Sahel is predominantly wet as is the Guinean coast region, but negative precipitation anomalies dominate in the southwest and over the Cameroon highlands.

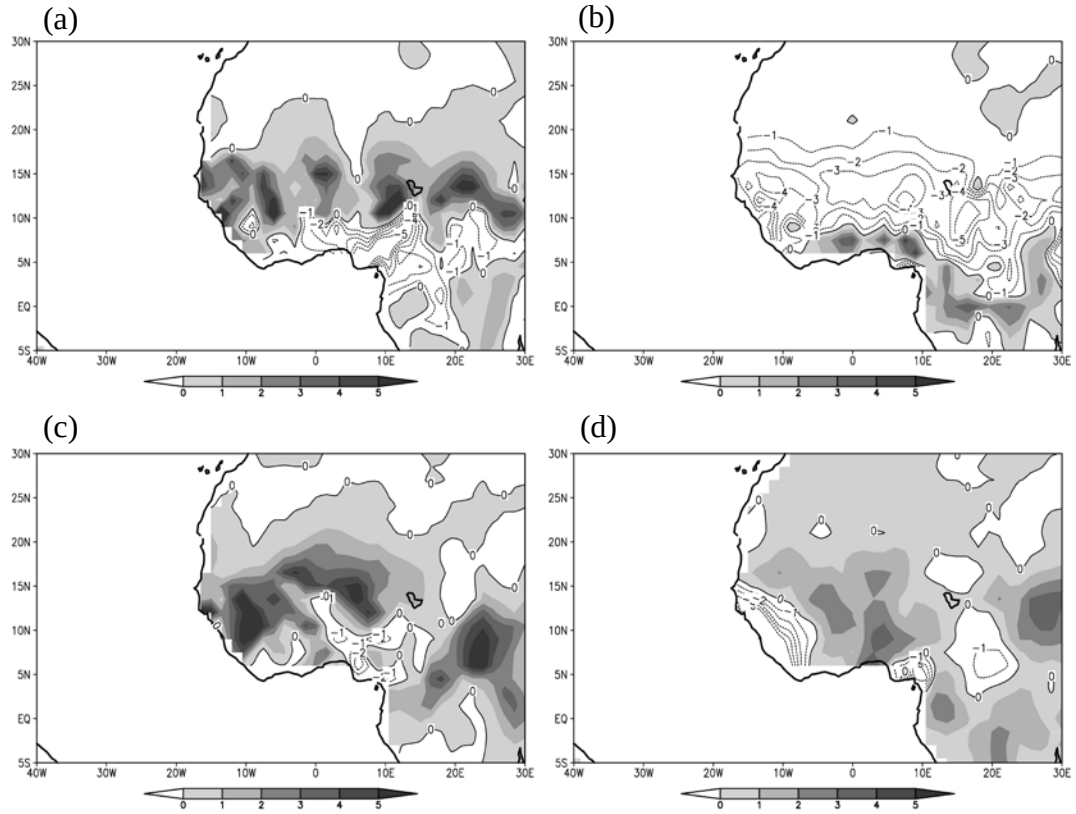

Figure 2.9 Precipitation anomalies for (a) 1964, (b) 1984, (c) 1999 in the CRU data, and (d) 2007 in the GPCP data with reference to the 1958-2009 mean. Shading denotes positive anomalies while contours denote negative anomalies with intervals of -1 mm day^{-1}.

An examination of the moisture transport connects the flow and precipitation anomalies for these extreme years. Figures 2.10a-d display anomalies of M_1 (Eq. 2.2) for 1964, 1984, 1999, and 2007, respectively. In the anomalously wet years in the Sahel of 1964, 1999, and 2007, westerly moisture fluxes from the eastern Atlantic are enhanced (Figs. 2.10a, c, and d, respectively) in association with a strong WAWJ (Fig. 2.3a). Westerly and southerly anomalies over the continent further transport moisture eastward and northward to the Sahel. In 1984, the westerly moisture flux at 8°-12°N over the eastern Atlantic is strongly decreased (Fig. 2.10b). Over land, an anomalous northerly flux between 0°-10°E and 10°-18°N transports moisture from the Sahel to the Guinean coast. Note that the anomalous northerly moisture fluxes over the

Guinean coast between 0° and 10°E in 1964, 1999 and 2007 (Fig. 2.10a,c, and d) are associated with a weaker southerly monsoon flow (not shown).

The moisture transport anomalies shown in Fig. 2.10 are consistent with the precipitation anomalies in Fig. 2.9 in general. Enhanced (decreased) rainfall in the Sahel is accompanied by enhanced (decreased) westerly moisture transport by the WAWJ.

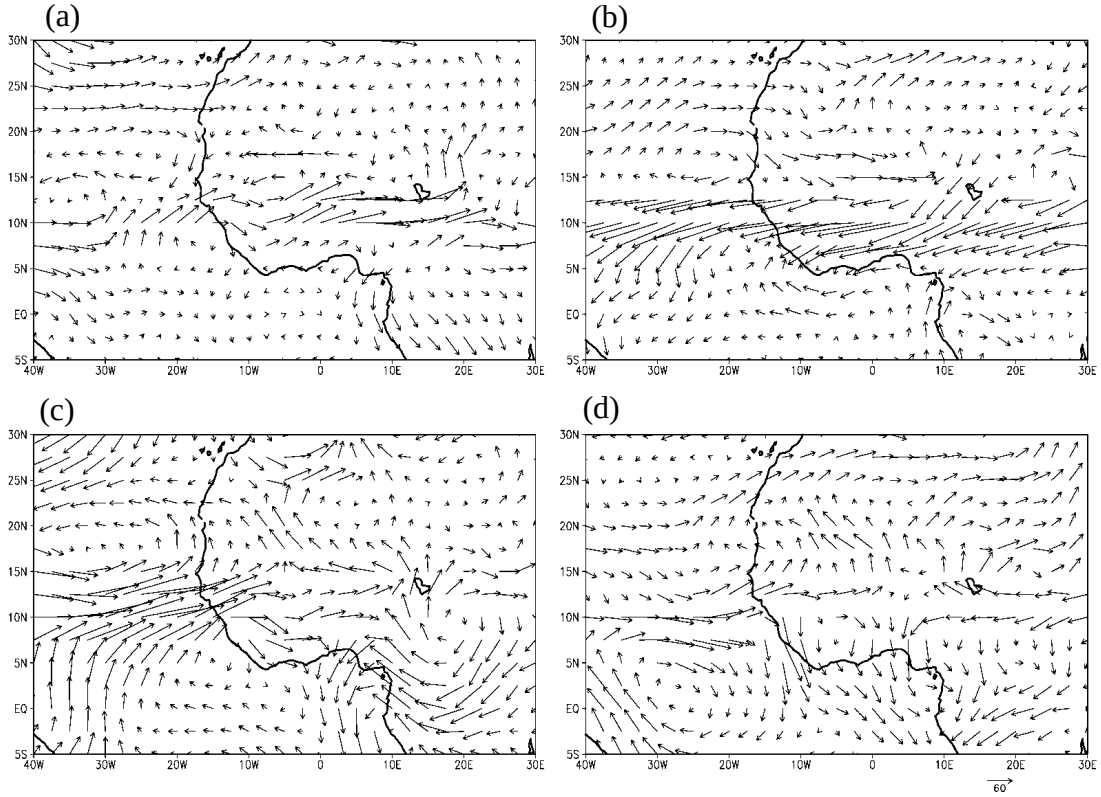

Figure 2.10 Anomalies of the vertically-integrated mass-weighted moisture transport from the surface to 700 hPa for (a) 1964, (b) 1984, and (c) 1999 from the ERA40 reanalysis, and (d) 2007 from the ERA-Interim reanalysis with reference to the 1958-2009 mean. Vector scale indicates the magnitude of the moisture flux in kg m^{-1} s^{-1}

Figures 2.11a-d show MSE anomalies averaged between 15°W and 30°E at 18°N (where the anomalies of precipitation are relatively large) for 1964, 1984, 1999

and 2007, respectively. In 1964, 1999, and 2007, the negative slopes of the MSE anomalies (solid lines) indicate a destabilized environment (Figs. 2.11a, c, and d, respectively). Increases in MSE at low levels are associated with moisture (dashed line) increases below 700 hPa. The geopotential term (dotted line) changes little while the temperature term (dot-dash line) either tends to stabilize the vertical column (Figs. 2.11a and c) or changes little compared to the climatology (Fig. 2.11d). In 1984, decreases in low-level MSE are related to large decreases in moisture content below 600 hPa (Fig. 2.11b). While increases in low-level temperature tend to destabilize the vertical column, the effect of moisture decreases dominates and the stability of the atmosphere increases.

As shown in Figs. 2.9-2.11, the association between the WAWJ and Sahel rainfall persists in various cases from different periods, suggesting that this relationship is robust.

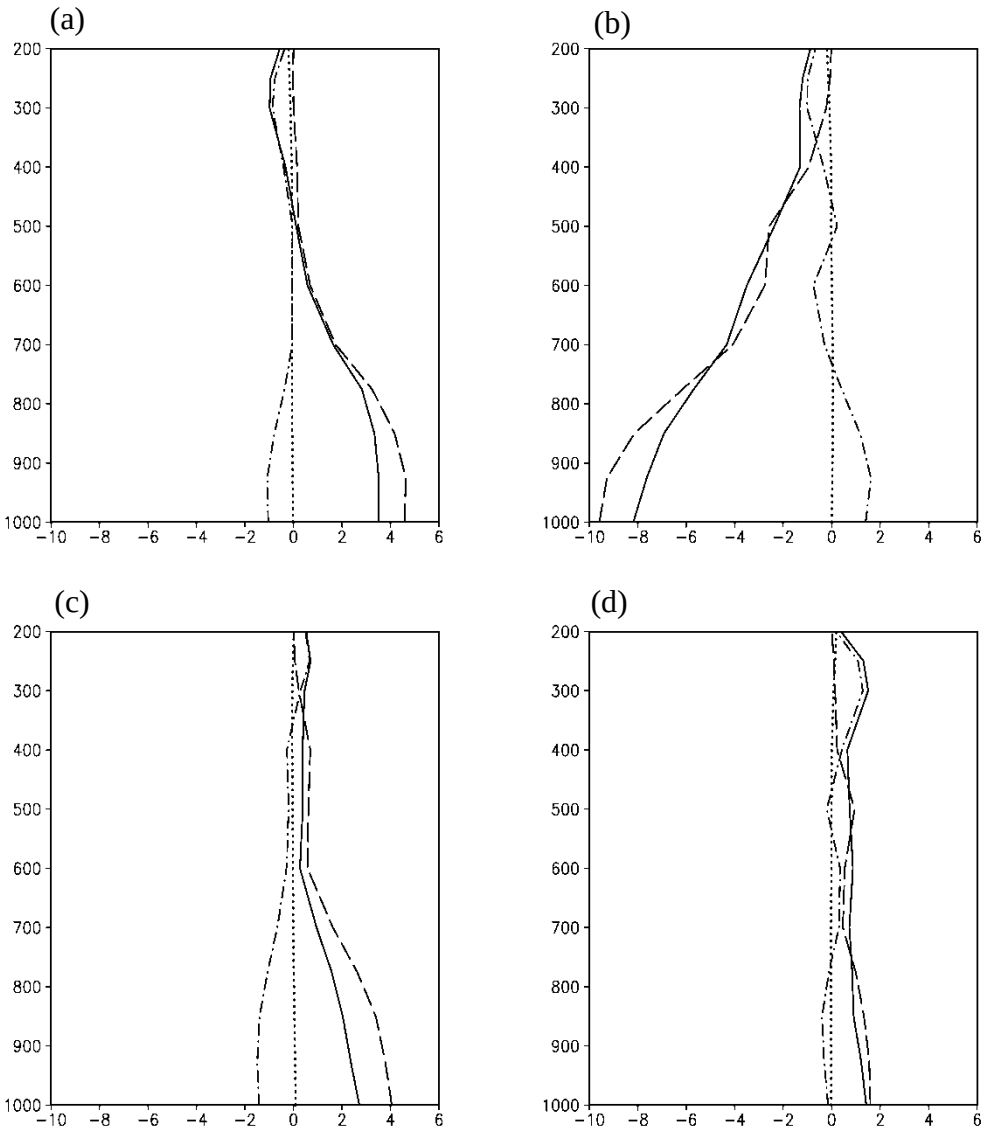

Figure 2.11 Anomalies of MSE terms averaged between 15°W and 30°E at 18°N for (a) 1964, (b) 1984, and (c) 1999 from the ERA40 reanalysis, and (d) 2007 from the ERA-Interim reanalysis with reference to the 1958-2009 mean. Sold lines denote the total MSE, dashed (dot-dash) lines denote the moisture (temperature) term, and dotted lines denote the geopotential term (units: 10^3 m^2 s^{-2}).

d. Comparison between the WAWJ moisture transport and the monsoon moisture transport

As displayed in Fig. 2.6a, both the southwesterly moisture flux associated with the monsoon flow across the Gulf of Guinea and the westerly flux associated with the WAWJ are important moisture sources for Sahel precipitation. Here we compare these two moisture sources.

Figure 2.12a displays a 50-year Hovmöller diagram of the zonal moisture transport averaged between 7.5°N and 10°N and vertically-integrated from the surface to 700 hPa. This represents moisture transport onto the African continent by the WAWJ. Moisture transport onto the continent by the monsoon flow is represented in Fig. 2.12b by the vertically-integrated meridional moisture transport averaged between 0° and 5°E. A comparison of Figs. 2.12a and b indicates that, overall, onshore moisture transport by the WAWJ is stronger and more variable than transport by the monsoon flow.

Westerly moisture transport associated with the WAWJ is strongest between 12°-20° W. Consistent with the previous discussion, this westerly moisture transport exhibits strong interannual and decadal variations. In the dry period (1972-1987), westerly moisture transport at 25°-35°W and 10°W-0°E is much weaker than during the wet (1958-1971) and recovery (1988-2009) periods. In the mid-1980s, westerly moisture transport between 5°W and 35°W decreases up to -60% compared with the climatological mean.

Southerly moisture transport from the Gulf of Guinea to the African continent is greatest between 0° and 10°N (Fig. 2.12b). Decadal variations are weaker than those of the zonal moisture transport (Fig. 2.12a). For instance, during the dry period of the late 1970s and the 1980s, the meridional moisture transport across the Guinean coast was very similar to that during the wet period in the 1960s.

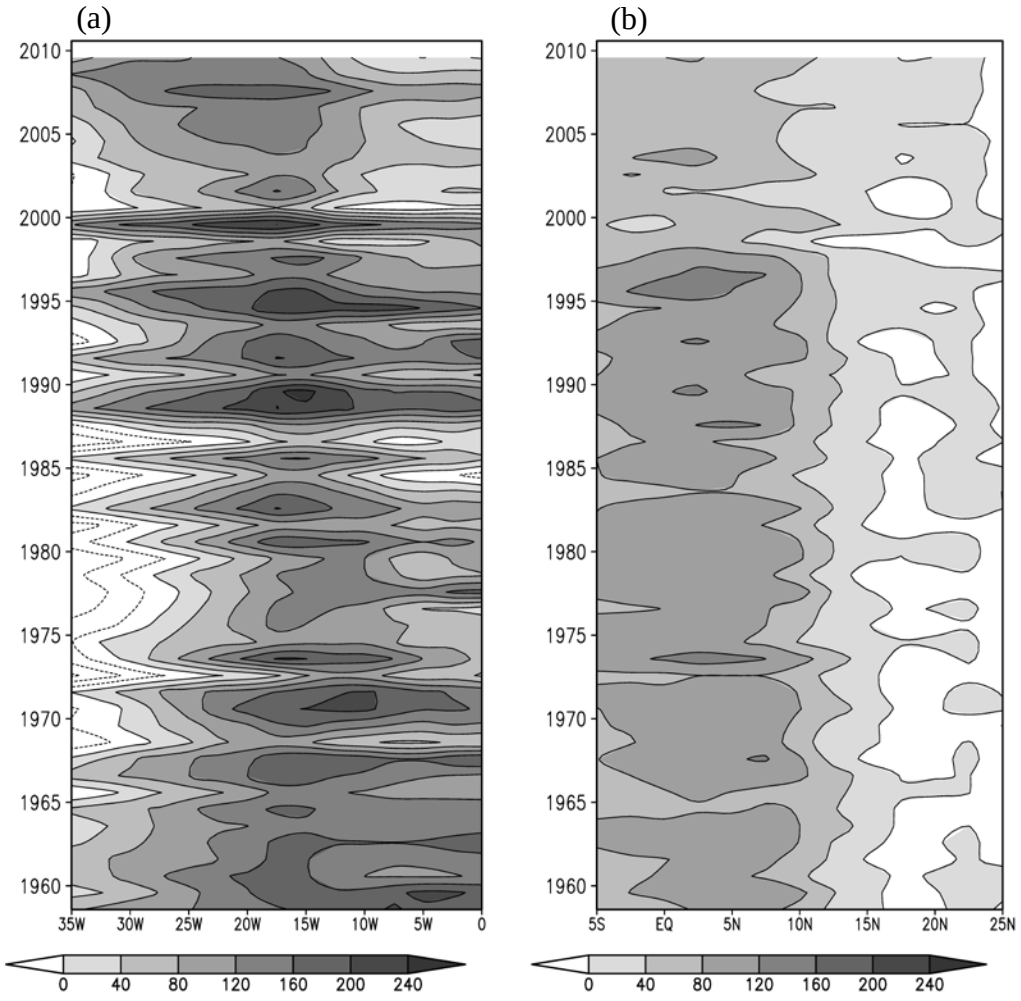

Figure 2.12 Vertically-integrated (a) zonal moisture flux (averaged between 7.5°N and 10°N) and (b) meridional moisture flux (averaged between 0° and 5°E) from the surface to 700 hPa in the ERA40 and ERA-Interim reanalyses. Contour interval is 40 Kg m^{-1} s^{-1}. Westerly and southerly fluxes are shaded.

Such a difference between the strength of the monsoon moisture transport and Sahel precipitation can also occur in individual years. For instance, in 1999 and 2007, when the Sahel was wet (Figs. 2.9c and d), the southwesterly monsoon flow and associated moisture transport (Figs. 2.10c and d) was weak. This agrees with Lamb (1983), who found that the strength of the monsoon moisture transport across the

Guinean coast is not always consistent with Sahel precipitation.

Figure 2.13 displays the WAM (dotted line) and Sahel precipitation (short-dashed line) indices (defined in section 3) along with their 9-year running means (solid and long-dashed lines) for 1958-2009. The monsoon index is relatively strong during the 1960s, around the average during the 1970s, and weak in the 1980s. After a small increase in the early 1990s, the monsoon index has weakened since the late 1990s. During the 2010s, the strength of the monsoon index decreased up to 15% compared with the climatological mean. The correlation between the WAM index and the Sahel precipitation index is 0.36 for 1958-2009, above the 99% confidence level but the correlation is lower than that between the WAWJ and Sahel precipitation, consistent with a weaker association between the southerly moisture transport over the Guinean coast and Sahel rainfall variations (Figs. 2.3a and 2.12b).

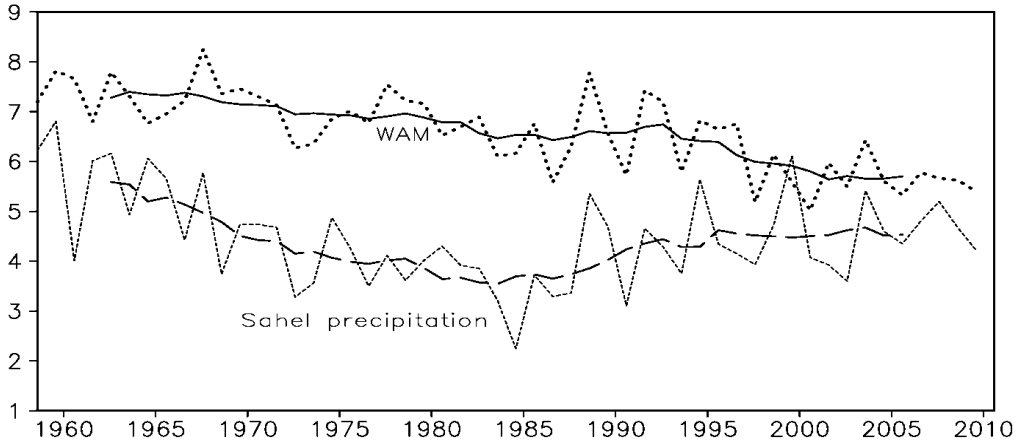

Figure 2.13 West African monsoon (dotted) index (m s^{-1}) and Sahel precipitation (short dashed) index (mm day^{-1}) and their 9-year running means (sold line for the monsoon index and long dashed line for the Sahel precipitation index). All indices are interpolated to a 1.5° grid.

e. Role of the WAWJ in the regional vorticity balance

The WAWJ is associated with Sahel precipitation not only through moisture

transports. In the quasi-equilibrium of the climatological mean, when mid-tropospheric condensational heating associated with monsoon rainfall stretches vortex columns in the lower troposphere and generates a positive low-level relative vorticity tendency, the low-level flow compensates by advecting negative vorticity into the region. Cook (1997) showed that the primary vorticity balance in this region is the Sverdrup balance, i.e., the positive vorticity tendency is balanced by the advection of low planetary vorticity air from lower latitudes by the monsoon flow across the Guinean coast. Here we find that vorticity advection by the WAWJ is also important for this balance,

The climatological vorticity equation is

$$-(\zeta + f)\nabla \cdot \vec{V} - \vec{V} \cdot \nabla(\zeta + f) + k \cdot \left(\frac{\partial \vec{V}}{\partial p} \times \nabla \omega \right) + k \cdot (\nabla \times \vec{F}) = 0 \,, \qquad (2.4)$$

where ζ is the relative vorticity, f is the Coriolis parameter, $\vec{V} = (u, v)$ is the horizontal wind, in which *u* is the zonal wind and *v* is the meridional wind, ω is the vertical p-velocity, and $\vec{F} = (F_x, F_y)$ is friction. Variables are averaged over time for the climatology, such that $\partial\zeta / \partial t = 0$, the effects of transients are neglected [see Cook (1997)], and the frictional generation of relative vorticity is calculated as a residual.

Figures 2.14a and b display the convergence and advection terms (first 2 terms on the left hand side in Eq. 2.4) for August at 925 hPa for the 1958-2002 ERA40 climatology. The 925-hPa level is chosen because it displays the role of the WAWJ most clearly, but the 850 hPa level is very similar. Between 5°N and 15°N over the eastern Atlantic and West Africa, a positive vorticity tendency is associated with the convergence term (Fig. 2.14a) in the vicinity of the WAWJ. South of the jet core at 10°N, this vorticity tendency is balanced by the advection term (Fig. 2.14b). North of 10°N, the positive vorticity tendency is balanced by friction (not shown), similar to

Cook (1997). The tilting term is relatively small terms and is also not shown.

The negative vorticity tendency over the eastern Atlantic and the West African coast just south of 10°N associated with advection (Fig. 2.14b) is generated by the northward advection of low absolute vorticity. This is similar to the findings of Cook (1997) for the monsoon flow. However, for the monsoon flow the advection term was dominated by the meridional advection of low planetary vorticity air, while in the vicinity of the WAWJ it is dominated by the meridional advection of low relative vorticity air. In the jet region, the meridional gradient of the zonal wind is negative to the north of the jet core and positive to the south, setting up a positive (northward) meridional gradient of relative vorticity, i.e.,

$$\frac{\partial \zeta}{\partial y} \approx \left[\frac{\partial}{\partial y} \left(-\frac{\partial u}{\partial y} \right) \right] > 0 \cdot \tag{2.5}$$

So low relative vorticity is transported northward into the WAWJ region by the southerly flow $(-v\frac{\partial \zeta}{\partial y} < 0)$ into the Atlantic marine ITCZ in which the WAWJ is embedded. In this way, the WAWJ is coupled to the precipitation climatology in helping to maintain the local vorticity balance as well as through the moisture budget.

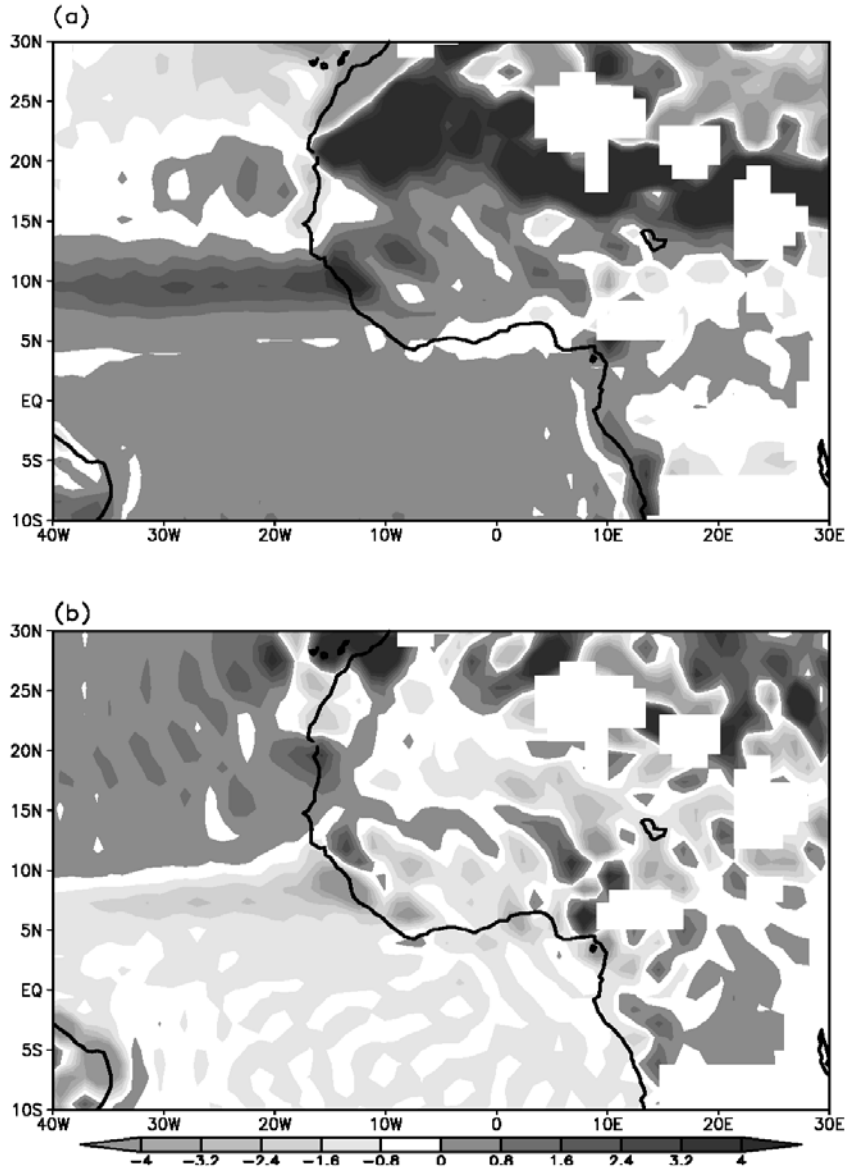

Figure 2.14 (a) Convergence and (b) advection terms in the vorticity equation (Eq. 2.4). Values are calculated for August at the 925 hPa level for the ERA40 climatology (1958-2002). Shading intervals are 0.8×10^{-10} s^{-2}. Topography is masked out.

f. Processes of WAWJ variations

PC2010 found that the WAWJ has a significant ageostrophic component, but the geostrophic component of the zonal flow, U_g, captures most of its seasonal variations. Here we find that the correlation between the WAWJ and U_g on interannual and decadal time scales is high, at 0.81 for the 1958-2009 analysis period (exceeding the 99% confidence level). This suggests that variations of the WAWJ are related to the low-level geopotential height gradient at 8°-13°N over the eastern Atlantic and to coastal SSTs (PC2010).

To explore the degree to which eastern Atlantic SSTs might influence decadal rainfall variability in the Sahel by forcing variations in the WAWJ, idealized (process-study) simulations with an atmosphere-only regional climate model were conducted using the NCAR/NOAA WRF (Weather Research and Forecasting) model (Skamarock et al. 2008) version 3.1. Previous work (Patricola and Cook 2010) found that with appropriate parameterization and resolution choices, WRF represents the features of the West African climate very well.

Following Patricola and Cook (2010), we use a domain from 57.6°W and 38.2°E to 16°S and 34.2°N, 28 vertical levels, 90-km resolution, and the following parameterizations: the RRTM longwave (Mlawer et al. 1997) and Dudhia shortwave (Dudhia 1989) radiation schemes; Noah land surface model (Chen and Dudhia 2001); Mellor-Yamada-Janjic planetary boundary layer scheme (Mellor and Yamada 1982; Janjic 1990, 1996, 2002); Kain-Fritsch cumulus scheme (Kain 2004; Kain and Fritsch 1990, 1993) .

For the control simulation, surface and lateral boundary conditions are climatological means (1958-2001) from the NCEP1 reanalysis, except soil moisture, soil temperature, skin temperature, and SST, which are from the ERA40 reanalysis. The model is initialized on March 15th, and run through the end of October.

Three additional simulations were conducted. In one, named *Test 1*, decadal-mean SSTs, surface and lateral boundary conditions for the relatively wet period of 1958-1971 are prescribed. A second simulation (*Test 2*) also uses SSTs for 1958-1971, but with climatological (1958-2001) surface, initial, and lateral boundary conditions. In a third simulation (*Test 3*), SST and boundary conditions for the dry period of 1972-1987 are prescribed.

None of the test simulations captures the observed decadal anomalies of the WAWJ or Sahel rainfall. In *Test 1*, the WAWJ is weaker than in the control run and Sahel rainfall decreases for JJAS. In *Test 2*, the WAWJ is weakly enhanced in July but changes little in August. Rainfall decreases between 5°-20°E and 7°-15°N and increases in the rest of West Africa in July. In August, rainfall between 13°-16°N and 10°W-10°E increases and decreases over the west coast and the eastern Sahel. In *Test 3*, the WAWJ is stronger than in the control run for June and September, but changes little in July and August. Rainfall decreases over the northern Sahel at 14°-15°W and increases in the south for June, August and September. In July, Sahel rainfall increases between 5°W and 5°E and decreases between 15°E and 30°E.

In short, the decadal anomalies produced by these simulations forced with decadal-mean Atlantic SSTAs do not resemble the observed anomalies. This suggests that decadal rainfall variations over the Sahel are not caused by Atlantic SSTs through control of the WAWJ, despite the fact that the WAWJ is a primary source of moisture for Sahel rainfall. Moisture is delivered into the Sahel by the WAWJ, but decadal variations in the WAWJ may be simply a *response* to variations in the rainfall that are forced in other ways.

Hagos and Cook (2008) found that decadal SST variations in the Indian Ocean influence the low-level westerly moisture flux near the West African coast. The results of the simulations discussed above support this result in suggesting that eastern

Atlantic SSTA forcing alone cannot explain decadal variations of Sahel rainfall and the WAWJ.

PC2010 showed that the formation of the region of westerly acceleration that produces the WAWJ is associated with the seasonal progression of the Atlantic marine ITCZ, so the role of the Atlantic ITCZ in the jet's decadal variability is examined here.

From 1958-2009, there are 8 years in which the WAWJ index anomaly exceeds one standard deviation, namely, 1964, 1967, 1970, 1988, 1989, 1994, 1995, and 1999. With the exception of 1970, the Atlantic marine ITCZ off the West African coast (20°-30°W) is located to the north of its climatological position in these "strong WAWJ" years. [The zero meridional wind speed contour is used to identify the location of the ITCZ as in Grist and Nicholson (2001).] Similarly, in 9 out of 11 "weak WAWJ" jet years, the ITCZ is located to the south of its climatological position.

The association between the speed of the WAWJ and the location of the Atlantic ITCZ is consistent with the dynamics of the jet formation (PC2010). In years when the ITCZ is located farther north (south), the westerly acceleration region is extended (reduced). Stronger (weaker) southerly winds between 8°-11°N and 20°-30°W enhance (decrease) the westerly acceleration through the Coriolis acceleration. Figure 2.15 shows the time series of the jet index (dotted line), a smoothed version of the jet index (9-year running mean; solid line), and the meridional wind speed (dot-dash line) averaged over the jet acceleration region (20°-30°W, 8.4°-10.6°N) also with its 9-year running mean (dashed line) from the ERA40 and ERA-Interim reanalyses. A high correlation (0.62 for 1958-2009, exceeding the 99% confidence level) between the two further confirms this hypothesis.

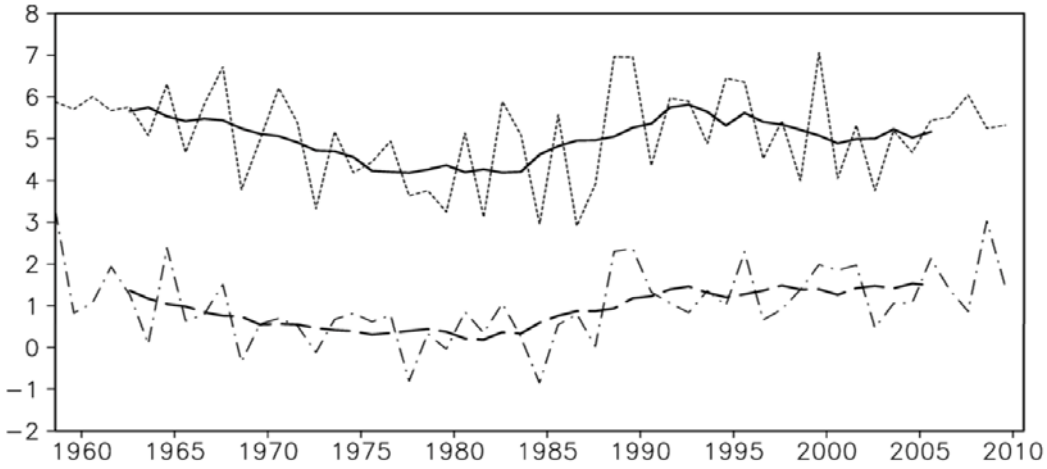

Figure 2.15 WAWJ (dotted line) index averaged over the jet region (15°-25°W, 8.4°-10.6°N) with its 9-year running mean (solid line) and the meridional wind speed (dot-dash line) averaged over the jet acceleration region (20°-30°W, 8.4°-10.6°N) with its 9-year running mean (dashed line) from the ERA40 and ERA-Interim reanalyses. Units are m s^{-1}.

2.5 Conclusions

Previous work documents that westerlies over the eastern Atlantic bring moisture to West Africa. This westerly flow is usually considered to be of the monsoon flow, but Grodsky et al. (2003) identified it as a low-level jet. Pu and Cook (2010) refer to this jet as the West African westerly jet (WAWJ) and further distinguish it from the monsoon flow by showing that it is physically separate and governed by different dynamics. Here, the relationship between the WAWJ and Sahel precipitation on decadal and interannual time scales is examined for August, when both the jet intensity and rainfall rates are maximum.

Correlations across different reanalyses and precipitation datasets over different time periods agree that variations of the WAWJ are significantly positively correlated to precipitation over West Africa between 10°-20°N and 18°W-30°E. Based on this co-variation of the WAWJ and Sahel precipitation, 3 periods are identified, namely, 1958-1971, 1972-1987, and 1988-2009, corresponding to times of a wet

Sahel/strong jet, dry Sahel/weak jet, and relatively wet Sahel/strong jet, respectively.

Decadal variations of Sahel precipitation are closely related to variations of the WAWJ. During wet (dry) periods, enhanced (weakened) westerly moisture transport by a strong (weak) WAWJ increases (decreases) the low-level moisture content over the Sahel, destabilizing (stabilizing) the atmosphere and fueling precipitation.

The relationship between the jet and Sahel precipitation is also found in individual years. For instance, in 1964, 1999, and 2007 (1984), when the jet is strong (weak), enhanced (reduced) westerly moisture fluxes occur over the eastern Atlantic, combined with anomalous southerly (northerly) moisture fluxes over the continent and Sahel precipitation increases (decreases) .

The WAWJ also plays an important role in maintaining the regional vorticity balance. In the jet region, the strong zonal wind shear sets up a positive (northward) relative vorticity gradient. The positive, low-level relative vorticity tendency due to mid-tropospheric condensational heating associated with precipitation is mainly balanced by the northward transport of low relative vorticity. This is different from the monsoon region where the Sverdrup balance dominates (Cook 1997).

The correlation between the monsoon index and the Sahel rainfall index is lower than that between the WAWJ index and the Sahel rainfall index, suggesting a weaker association between Sahel rainfall and the southwesterly monsoon flow over the Guinean coast in August. Moisture transport across the Guinean coast also has weaker decadal variability and is less consistent with Sahel rainfall variations than the westerly moisture flux across the West African coast associated with the WAWJ.

When monsoon flow over the Guinean coast is weak, e.g., 1964 and 1999, with an anomalously strong jet and enhanced westerly moisture transport, Sahel precipitation is strong. This suggests that the WAWJ plays an essential role in Sahel precipitation variations. As shown in the ERA40 and ERA-Interim reanalyses, the

monsoon flow is weakening in recent years, despite a partial recovery of Sahel rainfall. Understanding the relationship between the WAWJ and Sahel precipitation is especially useful under this scenario.

Strong (weak) jet years are usually accompanied by the northward (southward) displacement of the Atlantic marine ITCZ, revealing that the association between the WAWJ and the ITCZ is not limited to the seasonal time scale (PC2010). When the Atlantic ITCZ is located north of its climatological location, the southerly winds in the jet acceleration region (20°-30°W and 8.4-°10.6°N) are greater, enhancing westerly acceleration by the Coriolis force.

Regional model simulations suggest that forcing from eastern Atlantic SSTs alone does not explain decadal variations in the WAWJ. The WAWJ is a primary mode of moisture delivery to the Sahel from the Atlantic, but it is not controlled by Atlantic SSTs. Rather, it responds to variations associated with precipitation forced by other means, such as Indian Ocean SSTs (Hagos and Cook 2008).

REFERENCES

Adler, R.F., G.J. Huffman, A. Chang, R. Ferraro, P. Xie, J. Janowiak, B. Rudolf, U. Schneider, S. Curtis, D. Bolvin, A. Gruber, J. Susskind, P. Arkin, E. Nelkin 2003: The Version 2 Global Precipitation Climatology Project (GPCP) Monthly Precipitation Analysis (1979-Present). *J. Hydrometeor*., **4**, 1147-1167.

Cadet, D. L., and N. O. Nnoli, 1987: Water vapor transport over Africa and the Atlantic Ocean during summer 1979. *Q. J. R. Meteorol. Soc.*, **113**, 581-602.

Chen, F., and J. Dudhia, 2001: Coupling an advanced land-surface/ hydrology model with the Penn State/ NCAR MM5 modeling system. Part I: Model description and implementation. *Mon. Wea. Rev.*, **129**, 569–585.

Cook, K. H., 1997: Large-scale atmospheric dynamics and Sahelian precipitation. *J. Climate*, **10**, 1137-1152.

Cook, K. H., 1999: Generation of the African easterly jet and its role in determining West African precipitation. *J. Climate*, **12**, 1165-1184.

Druyan, L. M., and R. D. Koster, 1989: Sources of Sahel precipitation for simulated drought and rainy seasons. *J. Climate*, **2**, 1438-1446.

Druyan, L. M., 1989: Advances in the study of sub-Saharan drought. *Int. J. Climatol.*, **9**, 77-90.

Dudhia, J., 1989: Numerical study of convection observed during the winter monsoon experiment using a mesoscale two-dimensional model, *J. Atmos. Sci.*, **46**, 3077–3107.

Fontaine, B., P. Roucou, and S. Trzaska, 2003: Atmospheric water cycle and moisture fluxes in the West African monsoon: mean annual cycles and relationship using NCEP/NCAR reanalysis. *Geophys. Res. Lett*., **30**(3), 1117, doi:10.1029/2002GL015834.

Grist, J. P., and S. E. Nicholson, 2001: A study of the dynamic factors influencing the

rainfall variability in the West African Sahel. *J. Climate*, **14**, 1337-1359.

Grodsky, S. A., J. A. Carton and S. Nigam, 2003: Near surface westerly wind jet in the Atlantic ITCZ. *Geophys. Res. Lett*., **30**, 1-4.

Gu, G., and R. F. Adler, 2004: Seasonal evolution and variability associated with the west African monsoon system. *J. Climate*, **17**, 3364-3377.

Hagos, S. M., and K. H. Cook, 2008: Ocean warming and late 20th century Sahel drought and recovery. *J. Climate.*, **21,** 3797–3814.

Janjic, Z. I., 1990: The step-mountain coordinate: physical package, *Mon. Wea. Rev.*, **118**, 1429–1443.

Janjic, Z. I., 1996: The surface layer in the NCEP Eta Model, *Eleventh Conference on Numerical Weather Prediction*, Norfolk, VA, 19–23 August; Amer. Meteor. Soc., Boston, MA, 354–355.

Janjic, Z. I., 2002: Nonsingular Implementation of the Mellor–Yamada Level 2.5 Scheme in the NCEP Meso model, *NCEP Office Note*, **No. 437**, 61 pp.

Kain, J. S., and J. M. Fritsch, 1990: A one-dimensional entraining/ detraining plume model and its application in convective parameterization, *J. Atmos. Sci.*, **47**, 2784–2802.

Kain, J. S., and J. M. Fritsch, 1993: Convective parameterization for mesoscale models: The Kain-Fritcsh scheme, *The representation of cumulus convection in numerical models*, K. A. Emanuel and D.J. Raymond, Eds., *Amer. Meteor. Soc.*, 246 pp.

Kain, J. S., 2004: The Kain-Fritsch convective parameterization: An update. *J. Appl. Meteor.*, **43**, 170–181.

Kalnay, E., Coauthors, 1996: The NCEP/NCAR 40-year reanalysis project. *Bull. Amer. Meteorol. Soc.*, **77**, 437– 471.

Kanamitsu, M., W. Ebisuzaki, J. Woollen, S. Yang, J. Hnilo, M. Fiorino, and G.

Potter, 2002: NCEP-DOE AMIP-II reanalysis. *Bull.Amer. Meteorol. Soc.*, **83**, 1631-1643.

Kidson, J. W., 1977: African rainfall and its relation to the upper air circulation. *Quart, J. R, Met. Soc.*, **103**, 441-456.

Lamb, P. J., 1983: West African water vapor variations between recent contrasting Subsaharan rainy seasons. *Tellus,* **35A,** 198–212.

Long, M., D. Entekhabi, and S. E. Nicholson, 2000: Interannual variability in rain fall, water vapor flux, and vertical motion over West Africa. *J. Climate.*, **13**, 3827-3841.

Mellor, G. L., and T. Yamada, 1982: Development of a turbulence closure model for geophysical fluid problems. *Rev. Geophys. Space Phys.*, **20**, 851–875.

Mitchell, T. D., and P. D. Jones, 2005: An improved method of constructing a database of monthly climate observations and associated high-resolution grids. *Int. J. Climatol.*, **25**, 693-712.

Mlawer, E. J., S. J. Taubman, P. D. Brown, M. J. Iacono, and S. A. Clough, 1997: Radiative transfer for inhomogeneous atmosphere: RRTM, a validated correlated-k model for the longwave. *J. Geophys. Res.*, **102 (D14)**, 16663–16682.

Nicholson, S. E., 1981: Rainfall and atmospheric circulation during drought periods and wetter years in West Africa. *Mon. Wea. Rev.*, **109**, 2191-2208.

Patricola, C. M., and K. H. Cook, 2007: Dynamics of the West African monsoon under mid-Holocene processional forcing: Regional climate model simulations. *J. Climate*, **20**, 694-716.

Patricola, C. M., and K. H. Cook, 2008: Atmosphere/vegetation feedback: A mechanism for abrupt climate change over northern Africa. *J. Geophys. Res.*, **113**, D18102, doi: 10.1029/2007JD009608.

Patricola, C. M., and K. H. Cook, 2010: Northern African climate at the end of the

twenty-first century: an integrated application of regional and global climate models. *Clim. Dyn.*, **35**,193-212.

Pu, B., and K. H. Cook, 2010: Dynamics of the West African westerly jet. *J. Climate* (in press).

Simmons, A., S. Uppala, D. Dee, and S. Kobayashi, 2007a: ERA-Interim: New ECMWF reanalysis products from 1989 onwards. *ECMWF Newsletter No.110*, 25-35.

Simmons, A., S. Uppala, and D. Dee, 2007b: Update on ERA-Interim. *ECMWF Newsletter No. 111*, 5.

Skamarock, W. C., J. B. Klemp, J. Dudhia, D. O. Gill, D. M. Barker, M. G. Duda, X. Huang, W. Wang, and J. G. Powers, 2008: A Description of the Advanced Research WRF version 3, NCAR Tech. Note, NCAR/TN-475+STR, 125 pp.

Uppala, S. M., et al., 2005: The ERA-40 re-analysis. *Q. J. R. Meteorol. Soc.*, **131**, 2961–3012, doi:10.1256/qj.04.176.

UCAR/NCAR/CISL/DSS and ECMWF, 2005: ERA40 T106 Analysis Fields on Pressure Surfaces, created at NCAR. *Published by the CISL Data Support Section at the National Center for Atmospheric Research, Boulder, CO* (ds127.1).

Xie, P., and P. A. Arkin**,** 1996: Global precipitation: a 17-year monthly analysis based on gauge observations, satellite estimates, and numerical model outputs. *Bull. Amer. Meteor. Soc.*, **78**, 2539-2558.

CHAPTER 3

NORTH AMERICAN CLIMATE RESPONSE TO THE ATLANTIC MERIDIONAL OVERTURNING CIRCULATION SHUTDOWN AND GREENHOUSE GAS WARMING

3.1 Introduction

The thermohaline circulation is the density driven global ocean circulation. The part over the Atlantic basin is referred to as the Atlantic meridional overturning circulation (AMOC). The cold and dense water sinks at high latitudes and forms deep water, which flows southward to the Southern Hemisphere. At the surface, northward flow transports the warm and salty water to compensate the mass loss. Oceanic heat transport in the Atlantic, which is mainly associated with the AMOC, is overall northward (Ganachaud and Wunsch 2000; Stammer et al. 2003), with the magnitude of about 0.7 ± 0.2 PW (1 PW=10^{15} W) over the tropical Atlantic and 1.3 ± 0.15 PW near 25°N (Ganachaud and Wunsch 2000; 2003). Reorganization of the AMOC is believed in association with abrupt cooling events in paeloclimatic records (Alley and Agustsdottir 2005; Clark et al. 2001; Broecker 2003； Clarke et al. 2004). When the formation of the deep water is suspended by large amount of the freshwater input, the AMOC may be slowed or even shutdown.

Coupled atmosphere-ocean model simulations suggest that the strength of the AMOC is sensitive to increases in CO_2 concentration, and weakens as the sea surface buoyancy increases (Gregory et al. 2005). While the observed slowdown of the AMOC has some uncertainties (Kerr 2005; Latif et al. 2006), most of the IPCC (Intergovernmental Panel on Climate Change) coupled models predict a slowdown of the AMOC in the 21st century (IPCC AR4 2007). Although none of the IPCC model

predicts a complete shutdown of the AMOC by the end of the 21st century when forced with the IPCC SRES (Special Report on Emissions Scenarios, Nakicenovic et al. 2000) scenarios, studies also found that models may underestimate the possibility as many are less sensitive to the forcing, e.g., freshwater influxes, than the real world (Alley and Agustsdottir 2005). Estimation and understanding climate responses to the AMOC reorganization in the context of global warming will provide useful information for risk management.

While various models simulated the AMOC slowdown/shutdown in the future, few provide details on regional climate changes, as the coarse resolution of the GCMs (general circulation models) limits spatial details of the prediction. In this paper, we take advantage of the high resolution and regionally specified parameterizations of the regional climate model to provide a detailed study on climate variations over North America under a hypothetical shutdown of the AMOC in the period of 2081-2100. This study will add to the understanding of how the combined forcing of the greenhouse gas warming and AMOC shutdown influences regional climate.

Studies on climate impacts associated with the reorganization of the AMOC with emphasis on North American climate variations are reviewed in Section 3.2. Section 3.3 introduces the regional model used in this study and the simulation design. Section 3.4 is the model validation, comparing the output of the control simulation with the reanalyses and observations. Section 3.5 presents the results and Section 3.6 contains main conclusions.

3.2 Background

Studies found that about 8200 years ago, there was an abrupt cooling over Europe and northeastern North America, accompanied with drying over Sahara, western Asian monsoon regions, and probably the U.S. Great Plains, and a southward

shift of the ITCZ (Alley and Agustsdottir 2005). This “8k” event along with other cooling events, such as the Younger Dryas and Heinrich events, are believed to be associated with the reorganization of the AMOC (Alley and Agustsdottir 2005; Clark et al. 2001; Broecker 2003).

Studies suggest that enhanced freshwater influx before the cooling events may dilute the surface of the North Atlantic Ocean and suppress the formation of the Atlantic deep water and the meridional overturning circulation. For instance, the 8k event is believed to be related to the outburst flood by the drainage of large ice lakes about 8400 years ago (Clarke et al. 2004), while the Younger Dryas event is associated with the rerouted continental runoff from the Mississippi River to the St. Lawrence River at about 13,000 B.P. (before the present; Clark et al. 2001).

Model simulations with freshwater forcing produce anomaly patterns similar to the paleoclimatic records (Ressen et al. 2001a and b, 2002), further confirming that organization of the AMOC is an important mechanism for abrupt climate changes.

Global warming has a potential to change the buoyancy of the surface water over the North Atlantic and influence the strength of the AMOC. Recent observations show that freshwater input over the high latitude oceans increases (Dickson et al. 2003; Curry and Mauritzen 2005). Comparing the transatlantic section at 25°N with four pervious sections taken over the past five decades, Bryden et al. (2005) found that the AMOC has slowed by about 30 percent between 1957 and 2004, and the northward heat transport is reduced. However, since direct observation of ocean circulation is sparse and limited, there are uncertainties about the observed AMOC trend, e.g., whether its variations are within the nature variability or represent a long term trend (Kerr 2005; Latif et al. 2006).

Many atmosphere-ocean general circulation models (AOGCMs) simulate a weakening the AMOC when forced with increasing CO_2 concentration (Wood et al.

1999; Manabe and Stouffer 1999; Gregory et al. 2005). For instance, using the GFDL coupled model, Dixon et al. (1999) found that increasing greenhouse gas changes net surface freshwater fluxes (precipitation, evaporation and runoff from land) over the North Atlantic, reducing surface densities at high latitudes. The vertical convection is inhibited and the AMOC weakens.

Thorpe et al. (2002) found in HadCM3 coupled model, the AMOC weakens about 20% in response of a CO_2 increasing of 2% per year for 70 years. Schmittner et al. (2005) found 28 projections from 9 coupled models forced with the SRES A1B CO_2 concentration predicted a weakening of the AMOC by 25(±25)% until 2100.

Many studies explored the climate impacts of the AMOC shutdown in the coupled models. Vellinga and Wood (2002) studied the climate feedbacks of the AMOC shutdown in a pre-industrial climate state through an atmosphere-ocean coupled model, HadCM3. During the first 50 years after the AMOC collapsed in the model, the air temperature decreases about 1-2°C in the Northern Hemisphere and increases about 0-0.5°C in the Southern Hemisphere. Eastern North America and Europe cool about 1-2°C in (model) years 20-30, while the maximum cooling (-8°C) occurs over the northwest Atlantic. Precipitation is reduced over the large parts of the mid-latitudes in the Northern Hemisphere. Over the U.S. there is a weak increase of precipitation over the southwest. The ITCZ over the Atlantic and eastern Pacific is shifted southward.

Multi-model comparisons of the model reactions to idealized freshwater perturbations are reported by Stouffer et al. (2006). Freshwater flux of 0.1 Sv (1 Sv = 10^6 m^3 s^{-1}) is applied to the North Atlantic Ocean uniformly between 50°N and 70°N for 100 years to force 15 coupled AOGCMs and Earth system models. The strength of the AMOC at the 100^{th} year decreases by 9% ~ 62% among various models. The ensemble mean averaged in the 81-100 model years shows that most of the Northern

Hemisphere cools with a cooling maximum of -3°C located south of Greenland and 0°C to -0.6°C over the continents. Among the 15 models 5 have predicted a warming over the Barents and Nordic Sea in various degrees, which is caused by the northward shift of oceanic deep convection which results in increasing northward heat transport in higher latitudes. A warming of 0°C-0.3°C occurs in the Southern Hemisphere. Precipitation decreases in most of the Northern Hemisphere except over the North Pacific.

Another group of simulations with stronger freshwater perturbation of 1.0 Sv is conducted by 9 models. The AMOC collapses to a near shutdown condition within 50 years of the start of the perturbation. In the ensemble mean, the Northern Hemisphere cools about 2°C-3°C on average and the Southern Hemisphere warms about 0.3°C. The maximum cooling occurs between Scotland and Iceland up to -12°C. Over North America, cooling reaches -4°C in the northwest, and up to -2°C in other parts of the continent. Maximum warming of about 2.4°C occurs over the South Atlantic long the African coast.

Other simulations show similar results (Barreiro et al. 2008). When the AMOC is shutdown, the temperature in the Northern Hemisphere will decrease by 1-3°C, and there will be a slight warming of 0-0.5°C in the Southern Hemisphere. However, the warming in the South Hemisphere is lagged to the cooling in the Northern Hemisphere. Roche et al. (2010) found that under Last Glacial Maximum conditions after the AMOC is shutdown the maximum warming in the Southern Hemisphere occurs about 190-300 (model) years later than the coldest period in Greenland, and this result is supported by ice-core evidence (Petit et al. 1999; EPICA community members 2004) although the time resolution of records in Antarctica and Greenland are too coarse to clearly identify the time lag.

While these papers explore the climate change under paleoclimatic and pre-

industrial conditions, studies on the AMOC shutdown in the context of increasing CO_2 concentration is especially useful in predicting climate changes in the future as the cooling effect of the AMOC shutdown may offset or change the effects of greenhouse gas warming. Although the chance of the AMOC shutdown in the 21st century is very low, the possibility cannot be excluded (IPCC AR4 2007). Study of this extreme climate state will provide a likely upper limit of climate impacts for policy makers in risk management.

Using the coupled climate model HadCM3, Vellinga and Wood (2008) studied climate impacts of a hypothetical shutdown of the AMOC in the 2050s. The AMOC shutdown is artificially induced by applying 5×10^5 km^3 of freshwater perturbation to the North Atlantic between 50°N and 90 °N. The effect of greenhouse gas warming is also considered by prescribing historical CO_2 concentration for 1859-1990, IS92a scenario for 1990-2100 and a constant value of 700 ppmv for 2100-2150. The strength of the AMOC weakens with a rate of about -0.3 Sv/decade in the first half of the 21st century. After an instantaneous freshwater perturbation in 2049, it substantially reduces and then recovers at a rate of about 0.6 Sv/decade.

During the first decade of the AMOC shutdown, relative to global warming, the Northern Hemisphere air temperature cools about -1.7°C while the Southern Hemisphere slightly warms. Along the west fringes of Europe and most of the North Atlantic the cooling effect due to the AMOC shutdown outweighs the greenhouse gas warming effect and the temperature returns to pre-industrial conditions. As the AMOC recovers, by the year 2150 the temperature catches up with the parallel simulation forced by greenhouse gas alone. While precipitation changes are generally in opposition to that caused by the greenhouse gas warming, over Central America, Southern Europe, and Southeast Asia, the precipitation is further reduced.

They also compared climate impacts of the pre-industrial AMOC shutdown

with those of the AMOC shutdown under global warming and found that influences of the AMOC shutdown and greenhouse gas increasing may add linearly (e.g., averaged surface air temperature in the Northern Hemisphere over land) and nonlinearly (precipitation field) in different regions (Vellinga and Wood 2008).

Laurian et al. (2009) studied the cooling effect of the AMOC shutdown in the ECHAM/MPI-OM climate model simulation forced by 1.0 Sv freshwater and SRES A1B CO_2 concentration from 2001 to 2100. They found that a global surface cooling of 0.72 K (compared to the control simulation forced only by A1B CO_2 emission scenario) is associated with reduced downward longwave radiation due to reduced water vapor content.

Jacob et al. (2005) found that using a high resolution (0.5°) regional model to dynamically downscale the AOGCM output provided a better risk assessment for Europe of AMOC-induced climate change. They found that the regional model predicted a much larger fraction of snow in total precipitation than the global model because of its higher resolution and better ability to simulate regional orographic features.

Here we use a regional climate model to investigate the climate response over North America to the AMOC shutdown and greenhouse gas warming on high spatial (90 km) and temporal (monthly) resolutions. Our method is different from the dynamical downscaling that is directly driven by the AOGCM output. Detail simulation design is addressed in the following section.

3.3 Simulation design

The regional climate model NCAR/NOAA WRF (Weather Research and Forecasting) version 3.1.1 (Skamarock et al. 2008) is used to conduct the simulations. The model is fully compressible and non-hydrostatic, using flux-form Euler governing

equations to calculate horizontal and vertical winds, potential temperature and moisture on the terrain-following σ surface.

In order to examine how the shutdown of the AMOC will influence the regional climate adjacent to the North Atlantic, a relatively large domain is chosen. Figure 3.1 shows the domain, from 125°W to 30°E and from 5°S to 70°N. Here we focus on climate variations over North America. Changes over West Africa and Europe will be addressed in another paper.

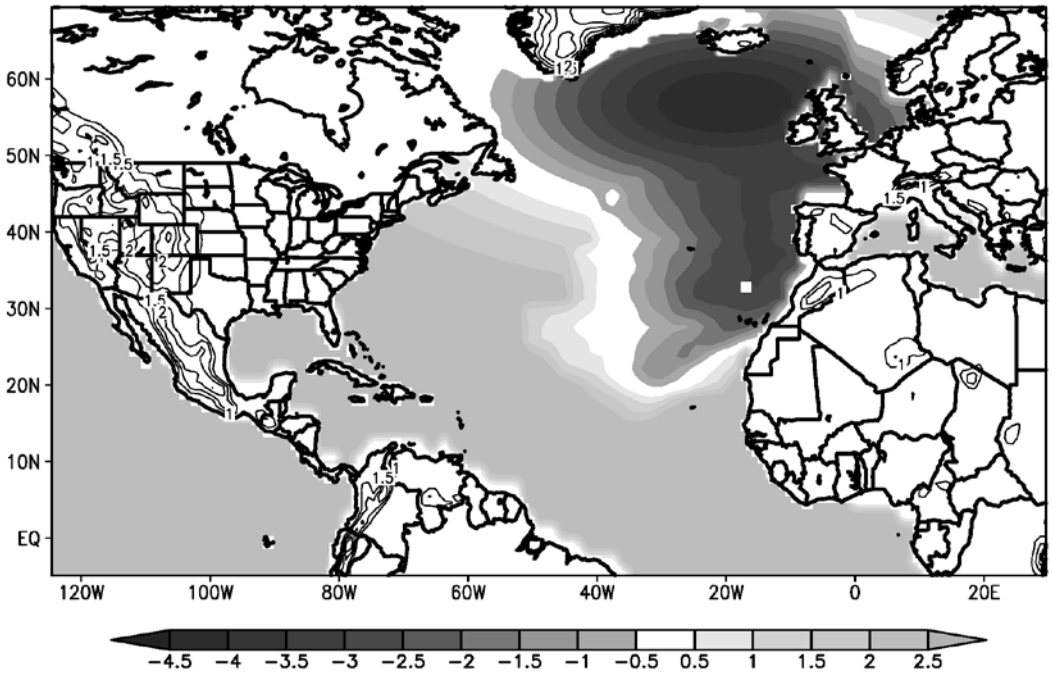

Figure 3.1 SST anomalies between the shutdown simulation and the control simulation. Shading over the ocean denotes SST anomalies with intervals of 0.5 K. Contours over land denote topography higher than 10^3m with intervals of 0.5×10^3m.

90-km resolution is used. Previous studies found this horizontal resolution is enough to produce a reasonable summer climate over northern Africa (Patricola and Cook 2010) and North America by the WRF model. The model contains 31 vertical levels, with the top of the atmosphere set at 30 hPa. The physical parameterization

selections are the same as Patricola and Cook (2010), except that the RUC land surface model (Smirnova et al. 1997, 2000) is replaced by the unified Noah land surface model (Chen and Dudhia 2001), which produces more realistic results. Other parameterizations used are: the Mellor-Yamada-Janjic planetary boundary layer scheme (Mellor and Yamada 1982; Janjic 1990, 1996, 2002), the Monin-Obukhov-Janjic surface layer scheme (Monin and Obukhov 1954; Janjic 1994, 1996, 2002), the new Kain-Fritsch cumulus scheme (Kain and Fritsch 1990, 1993) , the Purdue Lin microphysics scheme (Lin et al. 1983; Rutledge and Hobb 1984; Tao et al. 1989; Chen and Sun 2002), the RRTM longwave radiation scheme (Mlawer et al. 1997), and the Dudhia shortwave radiation scheme (Dudhia 1989).

Three groups of simulations are conducted, the control run, shutdown, and slowdown, to represent the present day climate, the extreme condition when the AMOC is shutdown and a mild state when the AMOC is slowed. In this paper we mainly discuss the results from the shutdown simulation. In each group, 20 years simulations are run to form a stable climatology. Interested in climate variations in summer and early autumn, in each year, integrations are initialized on 15 March and run for 200 days to 30 September. The first 17 days are disregarded for spin-up. Our analysis is focused on April -September.

In the control run, surface and lateral boundary conditions are from the NCEP2 reanalysis (Kanamitsu et al. 2002) for 1981-2000. Monthly values from the reanalysis are linearly interpolated to 6-hourly values for WRF input. The CO_2 concentration is held fixed at 330 ppmv.

Ensemble mean of 9 IPCC AR4 AOGCMs, the CCCMA_CGCM3.1, CNRM-CM3, ECHAM/MPI-OM, GFDL-CM2.0, MIROC3.2 (medium resolution), MRI CGCM2.3.2, NCAR CCSM, NCAR PCM, and the UKMO-HadCM3, following Patricola and Cook (2010), is averaged between 1981 and 2000 to form the present

day climatology. Output from the same 9 AOGCMs forced by the IPCC SRES A2 emission scenario for 2081-2100 is averaged to form the climatology in the future. The monthly mean differences between the two, future minus the present day, are used as "anomalies" and applied to the NCEP2 reanalysis (1981-2000) monthly values to form the lateral and surface boundary conditions for the hypothetical shutdown of the AMOC.

An idealized SSTA (SST anomaly) pattern is designed to represent Atlantic SST variations within two decades after the AMOC shutdown under greenhouse gas warming. Based on results of previous water-hosing experiments (Vellinga and Wood 2002, 2008; Stouffer et al. 2006; Chang et al. 2008; Barreiro 2008), a Gaussian shape cooling center of -7 K is placed over the North Atlantic at 20ºN and 55ºW. AOGCMs predict that the Atlantic will cool by -5 K ~ -12 K in terms of AMOC shutdown, and -7 K is in the middle of this range. SSTs over the eastern boundary current (e.g., the Canary Current) region also cool but in a lesser extent, so a comma-like cold anomaly pattern is designed. Over the whole domain, a uniform 2.5 K warming is applied to all the ocean points to represent the effect of greenhouse gas warming by the end of the 21st century. 2.5 K is approximately the domain averaged warming of the GCM ensemble mean in 2081-2100. The SST prescribed to the WRF is the sum of this idealized SSTA and the NCEP2 1981-2000 SST.

CO_2 concentration is set to 757 ppmv, the mean value of the SRES A2 emissions scenario during 2081-2100. This scenario represents inaction of the global community, i.e., business as usual, and likely is an upper limit of the expected change in CO_2 concentration.

The AOGCM output does not provide the soil moisture and soil temperature fields that are needed in WRF input. Given the lack of a better option the same present day values from the NCEP2 reanalysis are used for the shutdown simulation for each

year. Examination of the soil moisture and soil temperature fields over Africa from previous simulations reveal that they adjust rapidly to the overlying atmospheric conditions, usually within a couple of weeks.

For the slowdown simulation, the setting is the same as the shutdown except the prescribed SSTA is the SST anomalies between the AOGCM ensemble mean averaged during 2081-2100 and during 1981-2000. The SSTA is positive over the whole domain with relatively weak warming of 0-1.5 K over the North Atlantic (centered at 20°-40°W and 45°-65°N) and 2-3 K warming over the subtropical and tropical oceans (not shown). The name "slowdown" is referred to the state of the AMOC in comparison to the present day. Note that the climate in this period is influenced by both greenhouse gas warming and the weakening of the AMOC.

3.4 Simulation Validation

Output from the control simulation averaged between 1981 and 2000 is compared with the reanalysis and observations in the same period to examine if the present day climate is well represented. Figures 3.2a-d show 850 hPa wind and geopotential heights from the ERA40 reanalysis and the control simulation for April-June (AMJ) and July-September (JAS) in the 1981-2000 mean. In AMJ, as shown in the ERA40 reanalysis, the primary large-scale system is the North Atlantic subtropical high (or the Bermuda high) over the ocean at 40°W and 25°N and the Icelandic low at high latitudes near 80°W (Figs. 3.2a). In the control run, the strength of two centers is about 10 pgm greater than that in the ERA40 reanalysis, and the westerly winds between them are also greater compared to the ERA40 reanalysis.

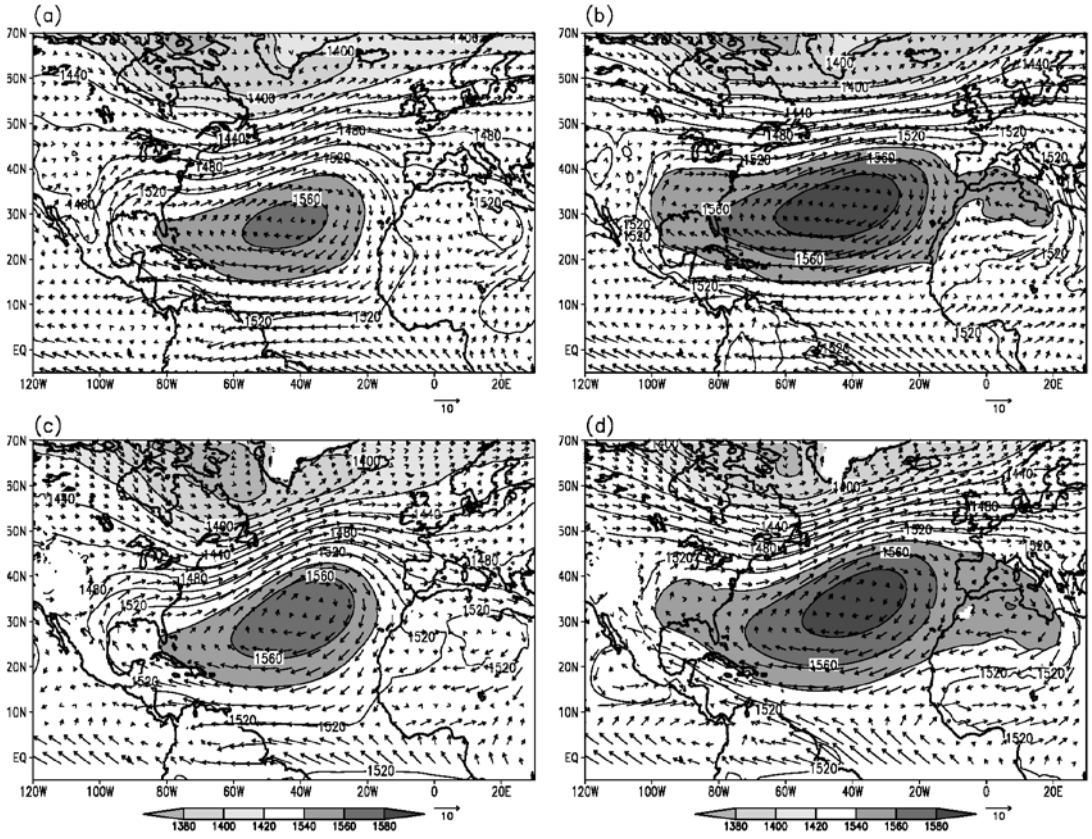

Figure 3.2 850 hPa geopotential heights and winds in (a)-(b) the ERA40 reanalysis and (c)-(d) the control run for (a), (c) AMJ and (b), (d) JAS in the 1981-2000 mean. Contour intervals are 20 gpm. Geopotential heights greater than 1540 gpm and less than 1420 gpm are shaded. Topography is masked out in the model output.

In JAS, the subtropical high is stronger and extends to the continents (Fig. 3.2b). In the WRF control run, while the east-west extension of the subtropical high is very similar to the ERA40 reanalysis, the north-south extension is a little weaker over the eastern U.S., but greater over the North Atlantic Ocean, Western Europe and northern Africa (Fig. 3.2d). Note that over the eastern Pacific there is a low located at 110°W and 15°N which does not appear in the ERA40 reanalysis (Fig. 3.2b) but is seen in the NCEP 2 reanalysis at 1000 hPa (not shown). This feature is associated with the relatively high SST between 10°-20°N and 95°-110°W in the NCEP 2 reanalysis. At high latitudes, the magnitude and location of the Icelandic low are very similar to those in the ERA40 reanalysis.

The root mean square (RMS) differences of 850 hPa geopotential height, zonal and meridional wind speeds between the control simulation and the ERA40 reanalysis are 8.9 (9.0) gpm, 1.2 (1.7) m s^{-1}, 0.9 (1.1) m s^{-1} for AMJ (JAS), respectively.

Major features at higher levels, e.g. 500 hPa and 200 hPa, are also well simulated by the WRF (not shown). In general, the control run successfully reproduced the large-scale circulation of the present day.

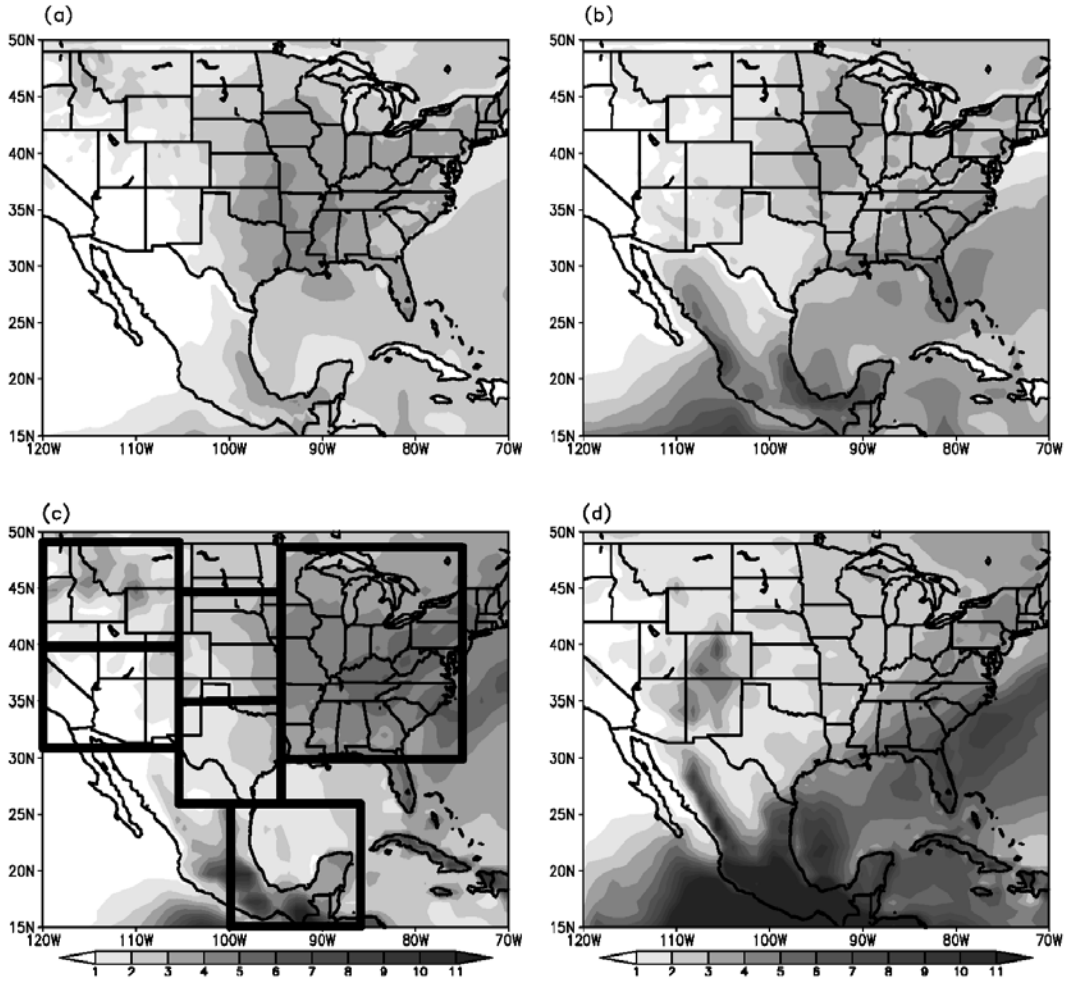

Figure 3.3 Precipitation from (a)-(b) the NARR and (c)-(d) WRF control run for (a), (c) AMJ and (b), (d) JAS in the 1981-2000 climatology. Black boxes denote six regions defined in Section 3.5.

Figures 3.3a-f display the AMJ and JAS averaged precipitation from the North American Regional Reanalysis (NARR; Mesinger et al. 2006) and the control run for 1981-2000. In AMJ, precipitation in the NARR is mainly located over the east central and eastern U.S., with a maximum at 90°W and 30°N (Fig. 3.3a). In the control run, while the rainfall gradient over the central U.S. is well-captured, the maximum is misplaced to around 80°W and 40°N (Fig. 3.3c). In the north, the maxima over Montana and Idaho are well simulated, although the magnitude is a little greater

compared to that in the NARR. Precipitation over the southern Mexico is also overestimated.

In JAS, precipitation maxima in the NARR are located over the upper Mississippi Valley and along the southeast coast (Fig. 3.3b). In the WRF control run, the precipitation maximum over the southeast coast is well simulated while the maximum over the upper Mississippi Valley is missed (Fig. 3.3d). Over Colorado and New Mexico, the precipitation is overestimated compared to the NARR. Over Mexico the precipitation amount is also much greater than that in the NARR.

RMS differences of the precipitation between the control simulation and the NARR shown in Fig. 3.3 (15°-50°N, 120°W-70°W) is 1.3 mm day^{-1} for AMJ and 3.4 mm day^{-1} for JAS.

Further examination of the monthly mean precipitation found that the rainfall maximum in June over the central U.S. is misplaced to May. 3 hourly output shows that over the central U.S., the mid-night to early morning rainfall maximum shown in the NARR is not captured by the control run (not shown). Over the Great Plains, the warm season precipitation is mainly contributed by the nocturnal precipitation, and both regional models (Davis et al. 2003) and AGCMs (Lee et al. 2007) have difficulties in capturing this maximum. Liang et al. (2004) found diurnal cycles of rainfall in a MM5-based regional climate model are sensitive to the choice of cumulus parameterization. The Kain-Fritsch scheme, which is used in our control run, works better in capturing the late afternoon peaks over the southeast U.S. where moist convection is controlled by the near-surface forcing, while the nocturnal precipitation maximum over the Great Plains is better represented by the Grell scheme. Davis et al. (2003) also found that the Kain-Fritsch scheme may put the rainfall maximum too far west. This is consistent with the overestimated rainfall over Colorado and New Mexico shown in Figs.3.3c and d.

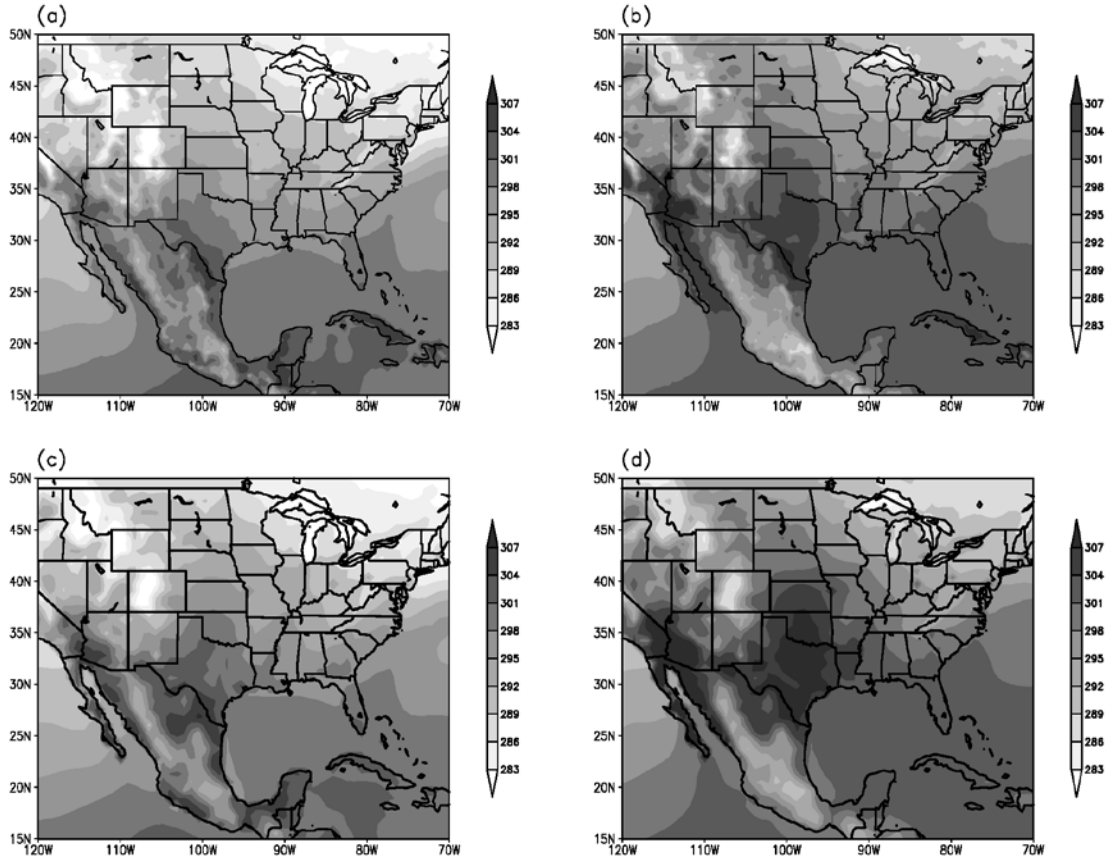

Figure 3.4 Skin temperature (K) from (a)-(b) the NARR and (c)-(d) WRF control run for (a), (c) AMJ and (c), (d) JAS.

Figures 3.4a-d display the surface skin temperature in the NARR and the control run for AMJ and JAS. In AMJ, as shown in Fig. 3.4a, temperature maxima in the NARR are located over southern Texas and along the west coast of Mexico. Over the northwestern U.S., the temperature is relatively low over the Rocky Mountains. Over the central and eastern U.S., there is a clear meridional temperature gradient. All these major features are well represented in the control run (Fig. 3.4c). In JAS, in the NARR the temperature maxima are located over central Texas and southeastern California, while the temperature over the central and southern Mexico is relatively low compared to that in the north (e.g., Texas) and over the ocean (Fig. 3.4b). In the

control run, the maximum in the U.S. is located further north in Texas and Oklahoma (Fig. 3.4d). Over the west coast of Mexico, temperature is higher than that in the NARR. Note that the skin temperature in NARR is not assimilated.

RMS differences of skin temperatures between the control simulation and the NARR shown in Fig. 3.4 is 1.8 K for AMJ and 2.1 K for JAS.

In summary, the large-scale circulation in the simulation domain and major climate features over the U.S. and Mexico are well captured by the WRF control run.

3.5 Results

a. Precipitation and circulation changes

The six regions (see Fig. 3.3c), the north central (35°-45°N, 95°-105°W), south central (26°-35°N, 95°-105°W), northwestern (40°-49°N, 105°-120°W), southwestern (32°-40°N, 105°-120°W), and eastern U.S. (31°-49°N, 75°-95°W), and the eastern Mexico (15°-26°N, 86°-100°W), are defined based on the monthly precipitation anomalies between the shutdown and control simulations and the seasonal precipitation changes in the control run. In these regions rainfall anomaly patterns and seasonal variations are relatively uniform.

Figures 3.5a-f show the regional averaged monthly precipitation in the control (black solid lines) and shutdown simulations (black dashed lines). Over the north central U.S. (Fig. 3.5a), in the shutdown simulation, precipitation decreases from April to September, with maximal anomaly of -0.9 mm day $^{-1}$ in August (about -42%). Two-tailed t-test is applied to examine if the differences between the control and shutdown simulations are statistically significant. It shows that monthly rainfall anomalies in June, July, August, and September are significant at the 80% confidence levels, while anomalies in April and May are not significant at the 80% confidence level.

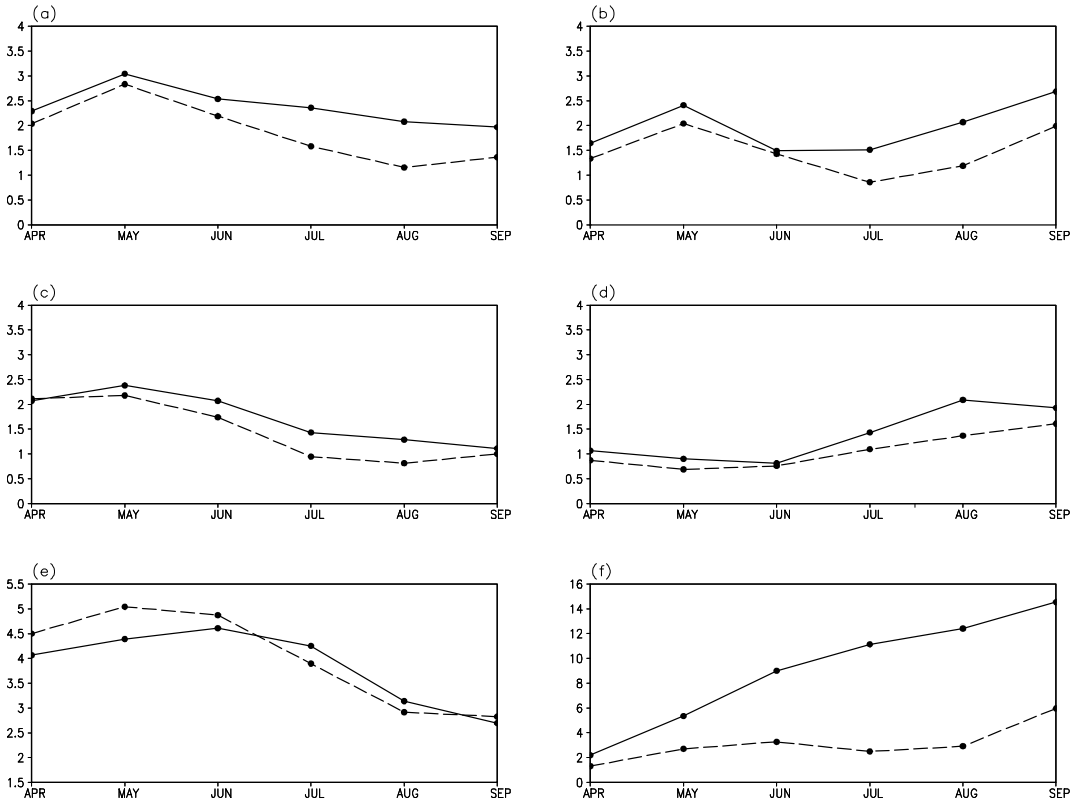

Figure 3.5 Regional averaged precipitation (mm day^{-1}) from the control (black solid lines) and shutdown (black dashed lines) simulations in the (a) north central, (b) south central, (c) northwestern, (d) southwestern, and (e) eastern U.S., and (f) the eastern Mexico.

Over the south central U.S. (Fig. 3.5b), in the shutdown simulation, precipitation also decreases in every month from April to September, with a minimal anomaly of -0.1 mm day^{-1} (about -5%) in June and a maximal anomaly of -0.9 mm day^{-1} (-41%) in August. Two-tailed t-test at the 80% confidence level shows that rainfall anomalies are significant in July, August, and September and not significant in April, May, and June.

In the shutdown simulation, precipitation decreases from May to September, with the largest decrease of -0.5 mm day $^{-1}$ in July and August (-35% to -38%) over the northwestern U.S. (Fig. 3.5c). Rainfall anomalies in June, July and August are

significant at the 80% confidence level, while anomalies in April, May and September are not.

Over the southwestern U.S. (Fig. 3.5d), precipitation decreases from April to September, with the largest decrease of -0.7 mm day $^{-1}$ in August (-35%). Rainfall anomalies are significant at the 80% confidence level from April to September except in June.

Over the eastern U.S.(Fig. 3.5e), in the shutdown simulation, precipitation in April-June and September is greater than that in the control run with a maximum increase of about 0.7 mm day^{-1} (15%) in May. In July and August, precipitation decreases up to 0.3 mm day^{-1} (-8%). Rainfall anomalies are significant at the 80% confidence level in April and May.

Precipitation over the eastern Mexico (Fig. 3.5f) decreases from April to September in the shutdown simulation, with a maximum decrease of 9.5 mm day^{-1} in August (about -78%). The rainfall anomalies are significant at the 80% confidence level from April to September.

In short, as shown in Fig. 3.5, in the shutdown simulation, precipitation over the most part of the U.S. and the eastern Mexico decrease from April to September, with a maximum decrease in August. Rainfall over the eastern U.S. also decreases in July and August, but increases in other months.

The vertically-integrated column moisture balance is examined to understand the precipitation anomalies. Changes in precipitation in the vertical column is contributed from the local evaporation and moisture convergence,

$$P = E - \frac{1}{g}\int_{Ps}^{Ptop} \nabla \cdot (q\vec{V})dp \,, \tag{3.1}$$

where P is precipitaoin, E is evaporation, q is specific humidity, P_s is surface pressure, P_{top} is the pressure at the top of the atmosphere, and $\vec{V}$ is horizontal wind. The second

term on the right of Eq.3.1 is the vertically-integrated moisture convergence. Here this term is calculated as the differences between the precipitation and evaporation (P-E).

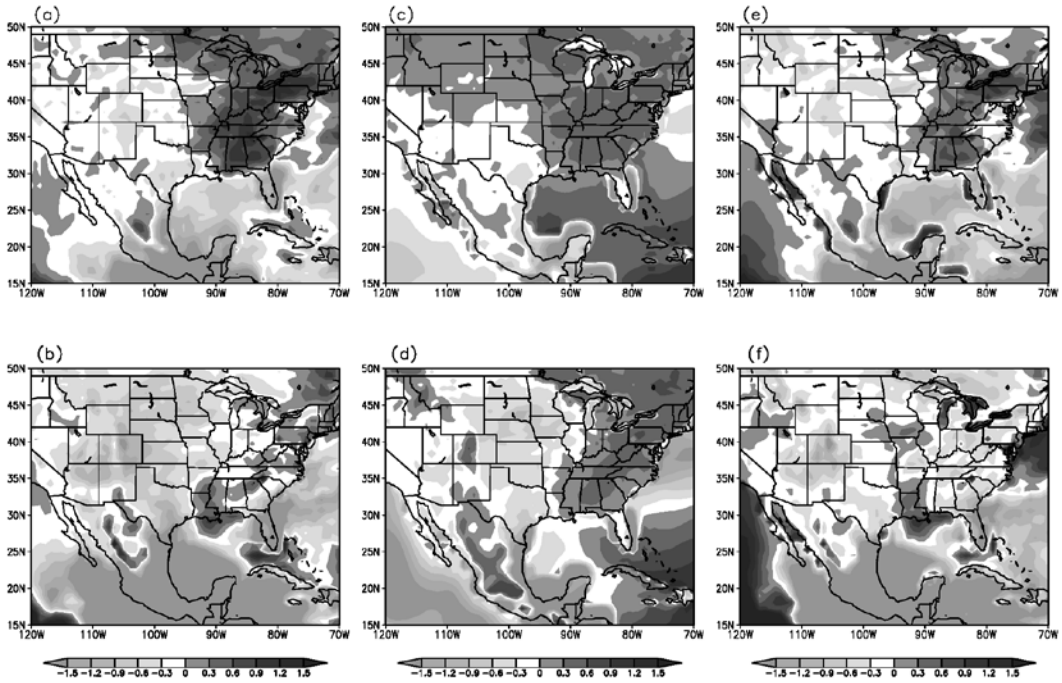

Figure 3.6 Anomalies of (a)-(b) precipitation (c)-(d) evaporation, and (e)-(f) (P-E) between the shutdown and control simulations for (a), (c), (e) AMJ and (b), (d), (f) JAS. Units: mm day^{-1}.

Figures 3.6a-f show the anomalies of precipitation, evaporation and vertically-integrated moisture convergence for AMJ and JAS between the shutdown and control simulations. In the shutdown simulation, precipitation increases over the eastern U.S and the central Mexico and decreases over the central and western U.S. in AMJ (3.6a). Evaporation plays an important role in precipitation anomalies, contributing up to two fifths of precipitation increases over the eastern U.S. (Fig. 3.6c). Decreases in evaporation over the south central U.S. also contribute to about one half of the anomalies. Patterns of moisture convergence anomalies are very similar to the precipitation anomalies in general (Fig. 3.6e). Over the western and north central U.S.,

decreases in precipitation are mainly related to the anomalous moisture divergence in this region, while over the eastern U.S. between 75°W and 90°W the anomalous moisture convergence contributes to about two fifths of the precipitation increase.

In JAS, precipitation decreases in most part of the U.S. except over a narrow region near the east coast (Fig. 3.6b). The drought is most severe over the central U.S., with precipitation decrease up to 1.3 mm day^{-1} (-40%). Over Mexico, precipitation decreases more in the south than in the north. Along the eastern and southern coast, precipitation anomalies are up to -80%. Evaporation decreases over the central and the western U.S., contributing about one half to the total rainfall anomalies, while over the eastern U.S. between 75°W and 90°W and the central Mexico, evaporation increases (Fig. 3.6d). Anomalous moisture divergence occurs over the western and west central U.S. with a center over Colorado (Fig. 3.6f). Moisture convergence is enhanced over the east central U.S. in Louisiana, southern Arkansas and Iowa. Over the eastern U.S., anomalous moisture divergence reduces the moisture content contributed by the enhanced evaporation. Over the southern Mexico and Gulf of Mexico, anomalous moisture divergence is the main contributor to the rainfall decrease.

As revealed in Fig. 3.6, variations of large-scale moisture convergence contribute significantly to the precipitation anomalies, while evaporation plays an important role in rainfall changes in JAS. Further examination of the evaporation anomalies in JAS found that they are very similar to the soil moisture anomalies in AMJ, which is closely related to AMJ precipitation anomalies (not shown). Considering the large contribution from the moisture convergence, we focus on understanding the variations in moisture convergence and how those are related to the large-scale circulation changes.

To reveal the association between moisture convergence (Eq. 3.1) and circulation changes, the vertically-integrated, mass-weighted moisture transport (flux),

M, is examined,

$$M = -\frac{1}{g}\int_{Ps}^{Ptop}(q\vec{V})dp \approx -\frac{1}{g}\sum_{p=Ps}^{p=125}(q\vec{V})\Delta p\,, \tag{3.2}$$

where q is specific humidity and $\vec{V}$ is the horizontal wind. The integration is from the surface (P_s) to P_{top}=125 hPa, and calculated as a finite sum shown on the right hand side of the equation.

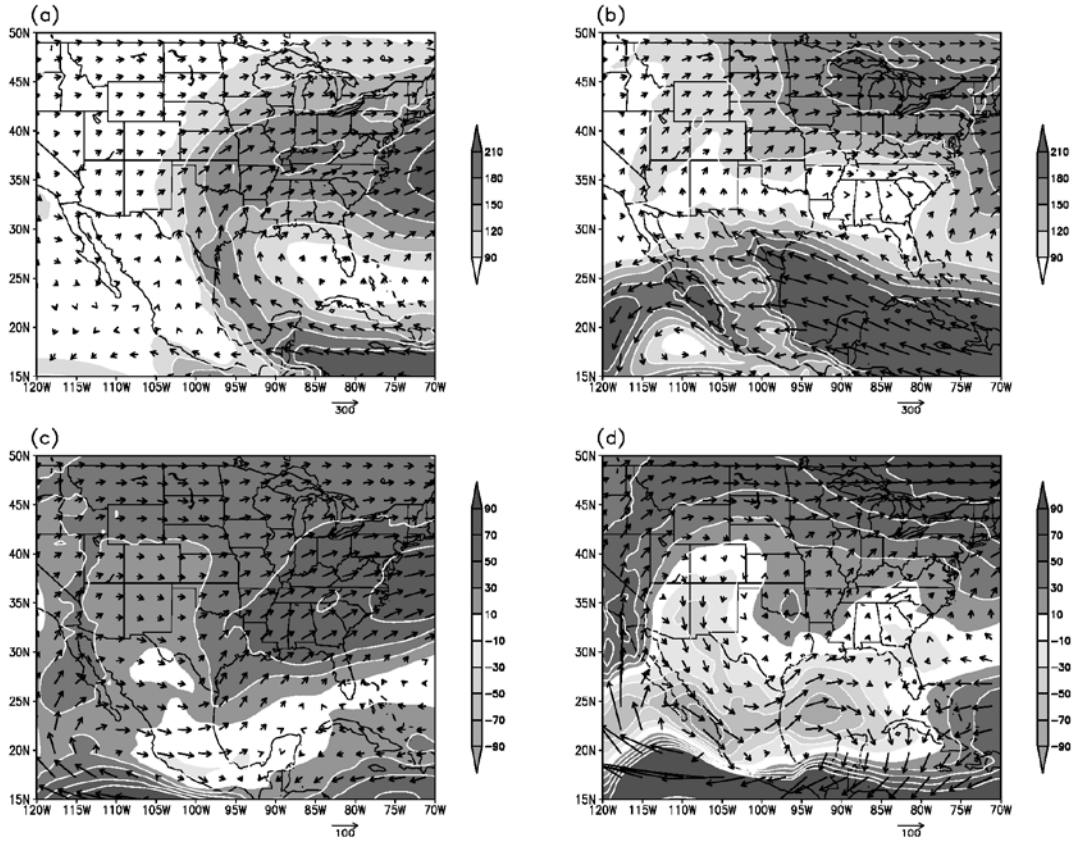

Figure 3.7 Vertically-integrated mass-weighted moisture transport (vectors; kg $m^{-1}s^{-1}$) for (a)-(b) the control simulation and (c)-(d) the anomalies between the shutdown and control simulations for (a), (c) AMJ and (b), (d) JAS. Magnitude of moisture transport greater than 90 kg $m^{-1}s^{-1}$ is shaded in (a), (b); for the anomaly fields (c), (d), shading denotes the magnitude differences between the shutdown and control simulations with intervals of 20 kg $m^{-1}s^{-1}$.

Figures 3.7a and b show M in the control simulation for AMJ and JAS, respectively. In AMJ, a southeasterly flux transports moisture from the Caribbean Sea and the Gulf of Mexico northward onto the North American continent (Fig. 3.7a). Over the central U.S., the southwesterly flow associated with the Great Plains low-level jet (GPLLJ) transports moisture northward. Between the 70°W and 90°W, the westerly flux brings moisture to the eastern U.S. In JAS, the magnitude of the easterly moisture flux from the Caribbean Sea and the Gulf of Mexico is greater compared to that in the spring, bringing more moisture to Mexico and southern Texas, while over the central U.S, the meridional moisture transport associated with the GPLLJ is weaker (Fig. 3.7b). Between 38° and 45°N northwesterly moisture flux transports moisture to from the central U.S. to the northeastern, while over the southeastern U.S. westerly moisture flux is relatively weak.

Figs. 3.7c and d show the moisture transport (M) differences between the shutdown and control simulations for AMJ and JAS, respectively. As shown in Fig. 3.7c, anomalous southwesterly moisture fluxes are located over the eastern U.S. between 75°W and 95°W, enhancing the moisture transport from the Gulf of Mexico onto the continent. This is consistent with the enhanced moisture convergence in Fig. 3.6e and precipitation increase in Fig. 3.6a. Between 85°-105°W and 17°-23°N southeasterly moisture transport is weaker than that in the control simulation. Over the Pacific Ocean, an anomalous southerly moisture flux transports more moisture to the Baja California peninsula and the southwestern U.S.

In JAS, anomalous westerly moisture fluxes over Mexico and the western Gulf of Mexico between 20°N and 30°N strongly decrease the southeasterly moisture transport onto Mexico and the south central U.S. (Fig. 3.7d). Between 80°-90°W and 15°-25°N, anomalous northeasterly flux also decreases the moisture supply from the eastern Gulf of Mexico and Caribbean Sea. At 117°W, a narrow southerly flux brings

moisture onto southern California. Between 100°W and 112°W, anomalous northerly flux transports moisture from the U.S. to the northern Mexico and merges with the westerly flux over the eastern Mexico. Between 90°W and 100°W, northward moisture transport is enhanced, while over the southeast coast moisture transport is decreased. The decreased moisture transport over the southern Rocky Mountains, Mexico, the southwestern U.S., and the Gulf of Mexico and the enhanced moisture transport in the west and north U.S. and the southern Mexico set up strong gradient of moisture transport, which is consistent with the anomalous moisture divergence (Fig. 3.6f) and precipitation anomalies (Fig. 3.6b).

To examine the relationship between the wind anomalies and moisture transport anomalies and how the moisture is transported from the coastal region to inland region, the height-longitude cross-section of wind (shading) and moisture transport (contours) anomalies (shutdown minus control) averaged between 30°N and 35°N are shown in Figure 3.8. Figs. 3.8a and b show the meridional wind and moisture transport anomalies from the surface to 300 hPa for AMJ and JAS, respectively, while Figs. 3.8c and d show wind and moisture transport in the zonal direction. In AMJ, southerly wind anomalies are located between 70°W and 102°W, relatively strong between 1000 hPa and 850 hPa and at high-level above 400 hPa (Fig. 3.8a). The Great Plains low-level jet (located between 90°W and 105°W in the control run, not shown) is enhanced about 25%. Above the Rocky Mountains between 102°W and 110°W, wind anomalies are northerly with a center at 750 hPa. At higher levels between 100°W and 115°W, northerly wind anomalies are located around 300 hPa. Over the west coast, wind anomalies are southerly.

Anomalous moisture fluxes are centered at lower levels and generally co-located with the wind anomaly centers (Fig. 3.8a). Southerly moisture transport anomalies are located between 70°W and 95°W, with maxima at 95°W in the GPLLJ

region and at 75°W over the western Pacific. Anomalous northerly moisture transport is centered at 103°W over the Rocky Mountains, while anomalous southerly moisture flux is located between 110°W and 120°W.

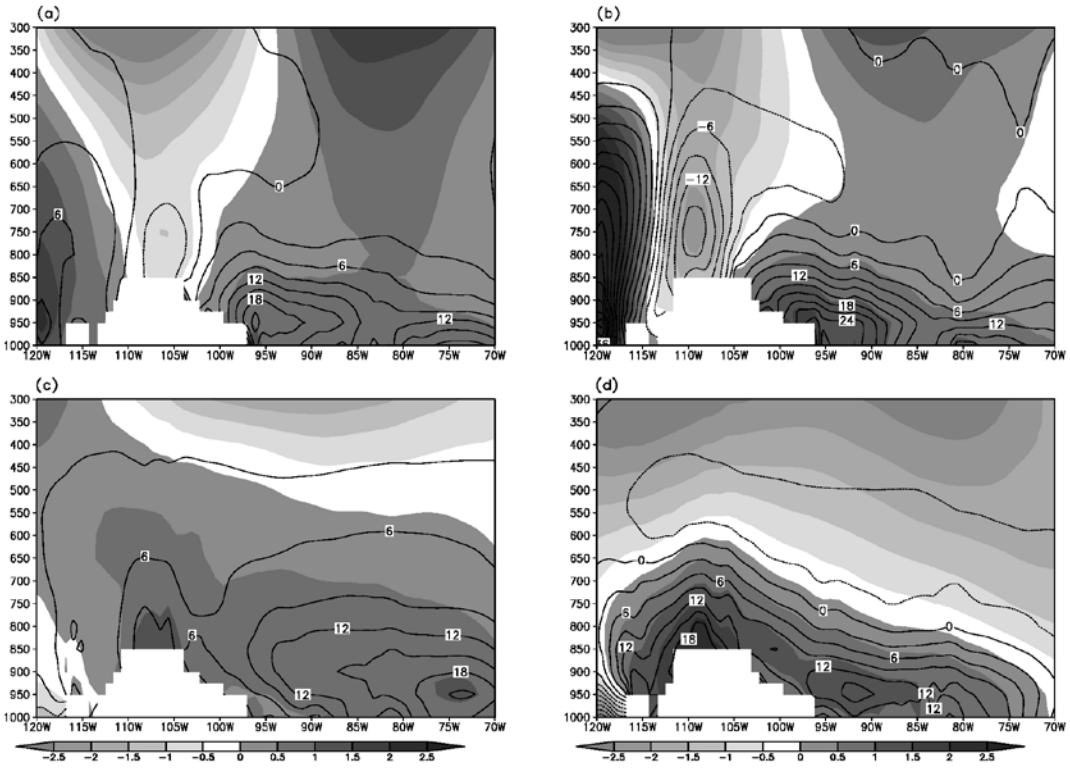

Figure 3.8 Anomalies of the wind (shading; m s^{-1}) and moisture transport (contours; m s^{-1}) in the (a)-(b) meridional and (c)-(d) zonal directions for (a), (c) AMJ and (b), (d) JAS. Positive (negative) values denote westerly (easterly) and southerly (northerly) wind and moisture transport anomalies. Topography is masked out.

In the zonal direction (Fig. 3.8c), the westerly wind anomalies between 70°W and 120°W extend from the surface to about 400 hPa, with maxima at 107°W and 74°W. The westerly moisture transport anomalies are concentrated at low levels, with two maxima co-located with the wind anomaly maxima.

In JAS, southerly wind anomalies are located between 70°W and 105°W, with maxima at 80°W and 98°W (Fig. 3.8b). The GPLLJ is enhanced by more than 30%.

Over the Rocky Mountains, anomalous northerly winds are centered at 110°W. Between 115°W and 120°W, the southerly wind anomalies are relatively strong, extending from the surface to 450 hPa. Consistent with wind anomalies, anomalous southerly moisture fluxes are located between 70°W and 105°W, while over the Rocky Mountains anomalous northerly moisture flux peaks at 110°W. In the west, the anomalous northward moisture flux is located at 115°-120°W.

In the zonal direction (Fig. 3.8d), westerly wind anomalies are located from 70°W to 117°W, extending from the surface to about 800 hPa over the eastern U.S. and to about 650 hPa over the Rocky Mountains. Easterly wind anomalies are located above the westerly anomalies with a maximum around 300 hPa. Anomalous westerly moisture fluxes are located at low-level, while anomalous easterly fluxes are located at higher levels, with maximum between 800 hPa and 400 hPa.

In short, Fig. 3.8 demonstrates that moisture transport anomalies are dominated by the wind anomalies. In AMJ, enhanced southwesterly moisture fluxes are associated with the southwesterly wind anomalies. In JAS, anomalous northerly moisture fluxes over the Rocky Mountains associated with northerly wind anomalies decrease the northward moisture transport, while anomalous easterly winds and moisture fluxes above 650 hPa decrease the eastward moisture transport from the central U.S. to the eastern U.S. Thus, the vertically-integrated moisture transport over the Rocky Mountains and the eastern U.S. is much weaker compared to that in the control run (Fig. 3.7d).

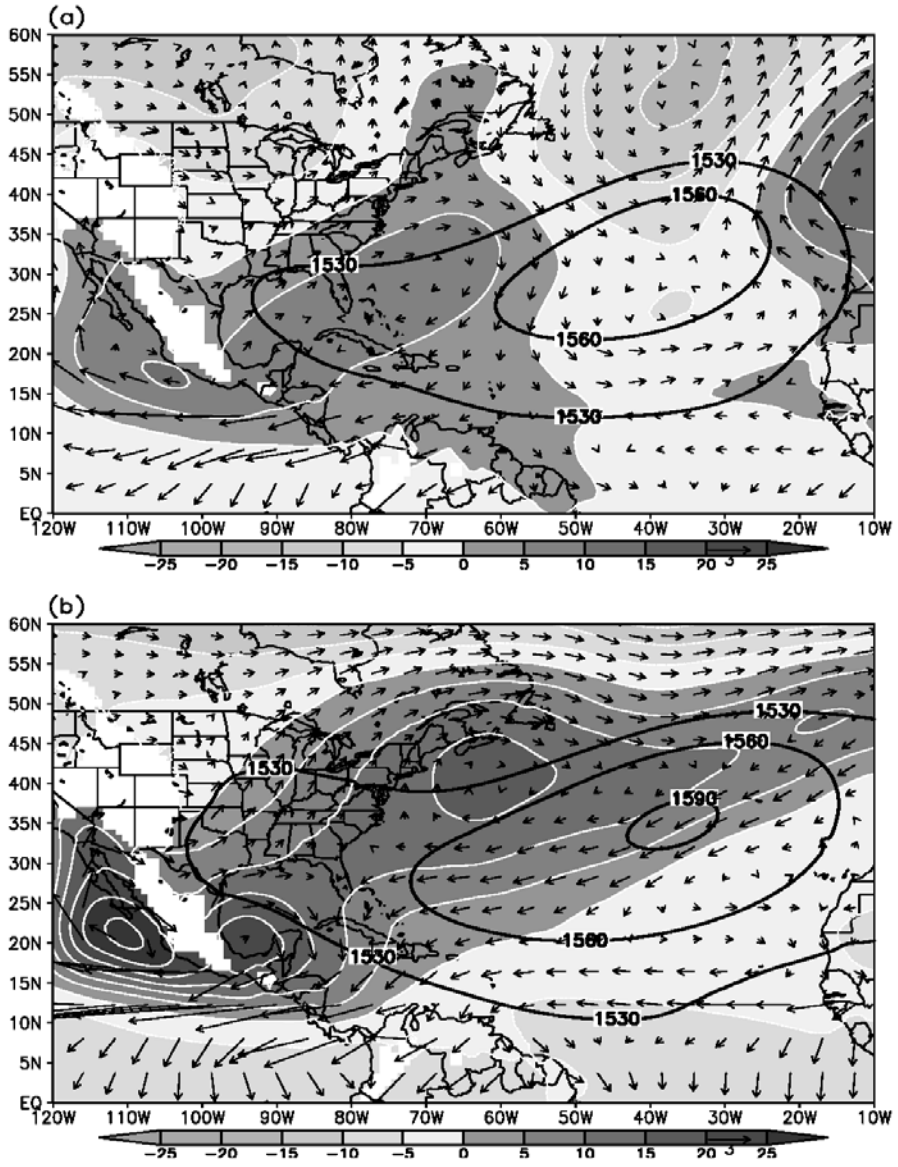

Figure 3.9 850 hPa wind (vectors; m s^{-1}) and geopotential height (shading; gpm) anomalies for (a) AMJ and (b) JAS. Location of the North Atlantic subtropical high in the control simulation is denoted by the thick black contours.

Figures 3.9a and b show the 850 hPa geopotential height (shading) and wind (vectors) anomalies for AMJ and JAS, respectively. The black thick contours indicate the location of the Atlantic subtropical high in the control simulation. Since geopotential heights increase in the whole domain in the shutdown simulation, to

emphasize the structure of the anomalies, domain averaged geopotential height difference between the shutdown and control simulations is subtracted from the anomaly field, following Cook et al. (2008). As shown in Fig. 3.9a, in AMJ the geopotential height is higher over the West Atlantic, the east and south coast of the U.S., Mexico and the Gulf of Mexico. Between 20°W and 50°W over the northern Atlantic, a negative anomaly is centered at 35°W and 50°N, while in the south at 0-10°N and 10°-45°W, the geopotential height anomaly is also negative. Over the eastern Atlantic a positive geopotential height anomaly is centered near 40°W. The distribution of the geopotential heights over the Atlantic is similar to the "quadrupole" identified by Cook et al. (2008) in their study of the springtime intensification of the GPLLJ in GCM simulations during 2079-2099 under the IPCC SRES A2 scenario, when the simulated AMOC is slowed. They found that the strengthened zonal geopotential height gradient enhances the GPLLJ and rainfall in the north central U.S.

Different from the GCM output shown by Cook et al. (2008), in the shutdown simulation the westward extension of the subtropical high is confined over the coastal region, but has greater northward and southward extensions. The geopotential height gradient over the eastern and south central U.S. and the east Gulf of Mexico is enhanced toward the southeast direction, accompanied with anomalous southwesterly wind anomalies. This is consistent with the enhanced southwesterly moisture transport (Fig. 3.7c) over the eastern U.S. in AMJ.

In JAS, the positive height anomalies are located at 10°-55°N over the northwestern Atlantic, the central and eastern U.S., the Gulf of Mexico, and the eastern Pacific near the Gulf of California (Fig. 3.9b). Compared to the geopotential height and wind anomaly field in AMJ (Fig. 3.9a), the Atlantic subtropical high extends further west and north in JAS. Over the central U.S. southwesterly wind anomalies accompanied with the southeastward geopotential height gradients enhance

the GPLLJ and the southerly moisture transport (Fig. 3.8b).

Over the Pacific between 10°N and 30°N, the anomalous high is much stronger than that in AMJ, extending from 80°W to 120°W, with two anomalous centers located near the west and east coast of Mexico. This anomalous high develops from near surface and extends up to 400 hPa (not shown). Examination of higher levels (above 750 hPa) found that the anomalous high is centered over the eastern Pacific. The formation of this anomalous high is associated with the variations of the land-sea surface temperature gradient. In the control run, in the north of 20°N, influenced by cold California current, SST is colder than skin temperature over land, while in the south of 20°N, land surface temperature is colder than that of the ocean. In the shutdown simulation, as the land surface temperature increases greater than that over the ocean, the land-sea temperature gradient increases in the north and decreases in the south. The low at 107°W and 17°N in the control run (Fig. 3.2) weakens, while in the north at 27°N a high forms over the ocean in the shutdown simulation (not shown). Anomalous subsidence associated with the southward shift of the Pacific ITCZ also contributes to the positive geopotential height anomalies between 10°N and 15°N (not shown).

The strong geopotential height gradients caused by this anomalous high are associated with large-scale anticyclonic flow between 10°- 35°N and 80°-120°N. The anomalous northerly flow over the Rocky Mountains and the southerly flow in the west shown in Figs. 3.8a and b are part of the anticyclonic flows related to this anomalous high. Over the Gulf of Mexico, the anomalous anticyclonic moisture fluxes are also associated with this anomalous high.

To examine the vertical circulation changes, Figures 3.10a-d show the streamlines of the zonal and vertical winds averaged between 30°N and 35°N for the control run and the differences of the shutdown run minus control run for AMJ and

JAS, respectively. Results are very similar if averaged between 30° and 40°N. Vertical wind speeds are shaded. As shown in Fig. 3.10a, in AMJ over the U.S. the flow are westerly in general. There is rising motion over the Rocky Mountains between 95°W and 115°W, with maxima over the west slope and ridge. In the east between 92°W and 102°W, subsidence occurs over the east slope of the Rocky Mountains in the mid-level. Over the eastern U.S., rising motion at low-level is relatively weak and stronger at 200 hPa.

In JAS (Fig. 3.10b), the rising motion over the Rocky Mountains is greater than that in AMJ, with strong sinking motion located between 85°W and 102°W, which has an easterly returning flow at lower levels. Rising motion is located over the eastern U.S. with a maximum between 500 hPa and 200 hPa. To the west between 115°W and 120°W the sinking motion is weaker compared to that in AMJ.

Figures 3.10c and d show the anomalies (shutdown minus control) of the streamlines and vertical wind speeds for AMJ and JAS, respectively. As shown in Fig. 3.10c, over the eastern U.S. between 80°W and 95°W rising motion is enhanced between the surface and 200 hPa. The rising motion over the Rocky Mountains and the sinking branch over the east slope weaken. Anomalous sinking motion is located over the east coast between 70°W and 80°W, while over the west coast there is anomalous rising motion.

In JAS, there is anomalous rising motion over the east coast between 80°W and 95°W, decreasing the sinking flow, while between 95°W and 105°W the sinking motion is enhanced (Fig. 3.10d). Over the Rocky Mountains, the rising motion is weakened over the ridge but enhanced over the west slope. Over the western U.S. the subsidence is weakened between 118°W and 120°W and enhanced between 115°W and 118°W.

As shown in Fig. 3.10, the enhanced rising motions at 80°-90°W over the

eastern U.S. in AMJ and over the south coast around 90°-95°W in JAS are consistent with anomalous moisture convergence (Figs. 3.6e and f) and the precipitation increase (Figs. 3.6a and b), while the anomalous subsidence over the central U.S. is also consistent with the enhanced moisture divergence.

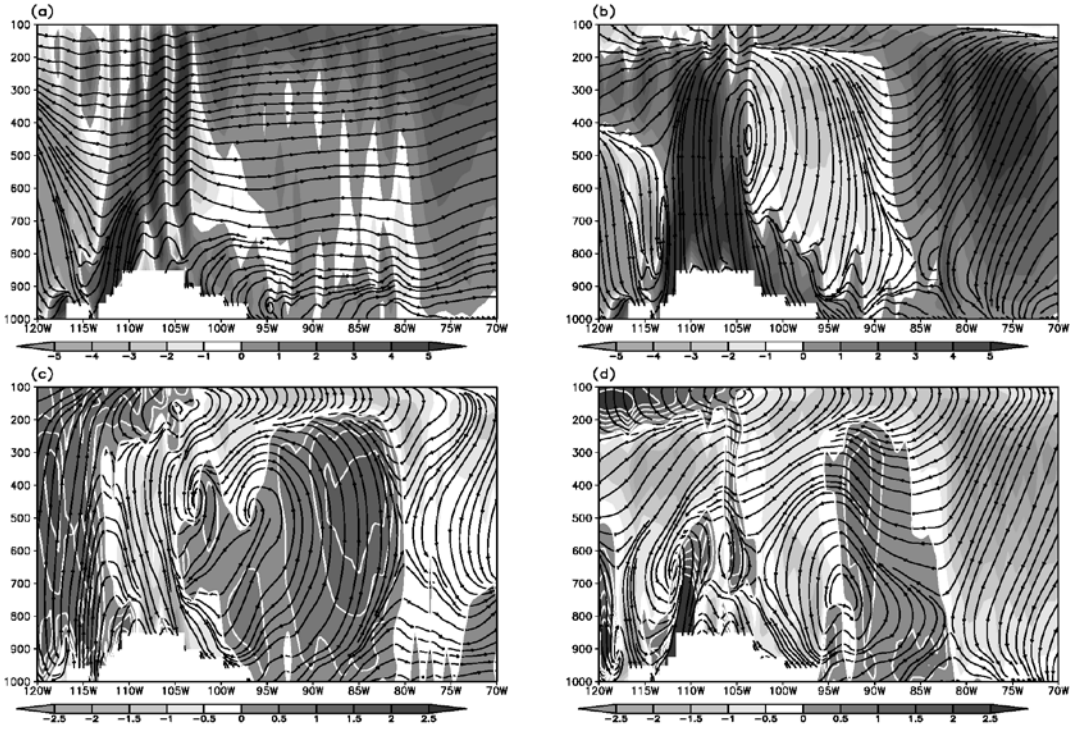

Figure 3.10 Streamline of zonal and vertical winds (scaled by 10^3; m s^{-1}) averaged between 30°N and 35°N in (a)-(b) the control simulation and (c)-(d) the anomalies between the shutdown and the control simulations for (a), (c) AMJ and (b), (d) JAS. Vertical wind velocity is shaded.

The moist static energy (MSE) is the sum of the sensible, latent and geopotential energy according to

$$MSE = c_p T + Lq + gz, \tag{3.3}$$

where c_p is the specific heat of air at constant pressure, T is air temperature, L is the latent heat of vaporization of water, q is specific humidity, g is the acceleration due to gravity, and z is height. MSE increasing with altitude denotes a stable atmosphere, so

increases in low-level MSE destabilize the vertical column and promote convection. MSE budget analysis helps to examine the how variations in the stability of the atmosphere are associated with variations in vertical temperature and moisture content profiles.

Figures 3.11a-b show the MSE anomalies over the eastern (80°-95°W, 30°-35°N) U.S. for AMJ and JAS, respectively. In AMJ, MSE increases at low-level between the surface and 500 hPa, and the stability of the atmosphere decreases (Fig. 3.11a). While the temperature profile contributes little to the MSE anomalies, increases in moisture content at low-level, which are associated with the enhanced southwesterly moisture transport (Fig. 3.7c), enhance the instability of the air column. Between 300 hPa and 100 hPa, variations in temperature and the moisture content nearly balance each other, and the stability of the atmosphere changes little.

In JAS, the MSE profile has a negative slope between 1000 hPa and 450 hPa (Fig. 3.11b). Decreases in stability are associated with increases in moisture content, which are associated with the anomalous southerly moisture transport (Fig. 3.8b). The temperature anomaly is nearly constant at low-level and contributes little to the structure of the MSE anomaly profile. Between 400 hPa and 100 hPa, the negative slope of the MSE is contributed by the temperature profile, which has a higher value at 200 hPa and a lower value at 500 hPa. The stability of the atmosphere is enhanced. This is consistent with the vertical wind anomalies at 80°-95°W (Fig. 3.10d). In JAS, with enhanced stability at higher levels, the anomalous rising flow is much weaker compared to that in AMJ and is confined in a smaller region.

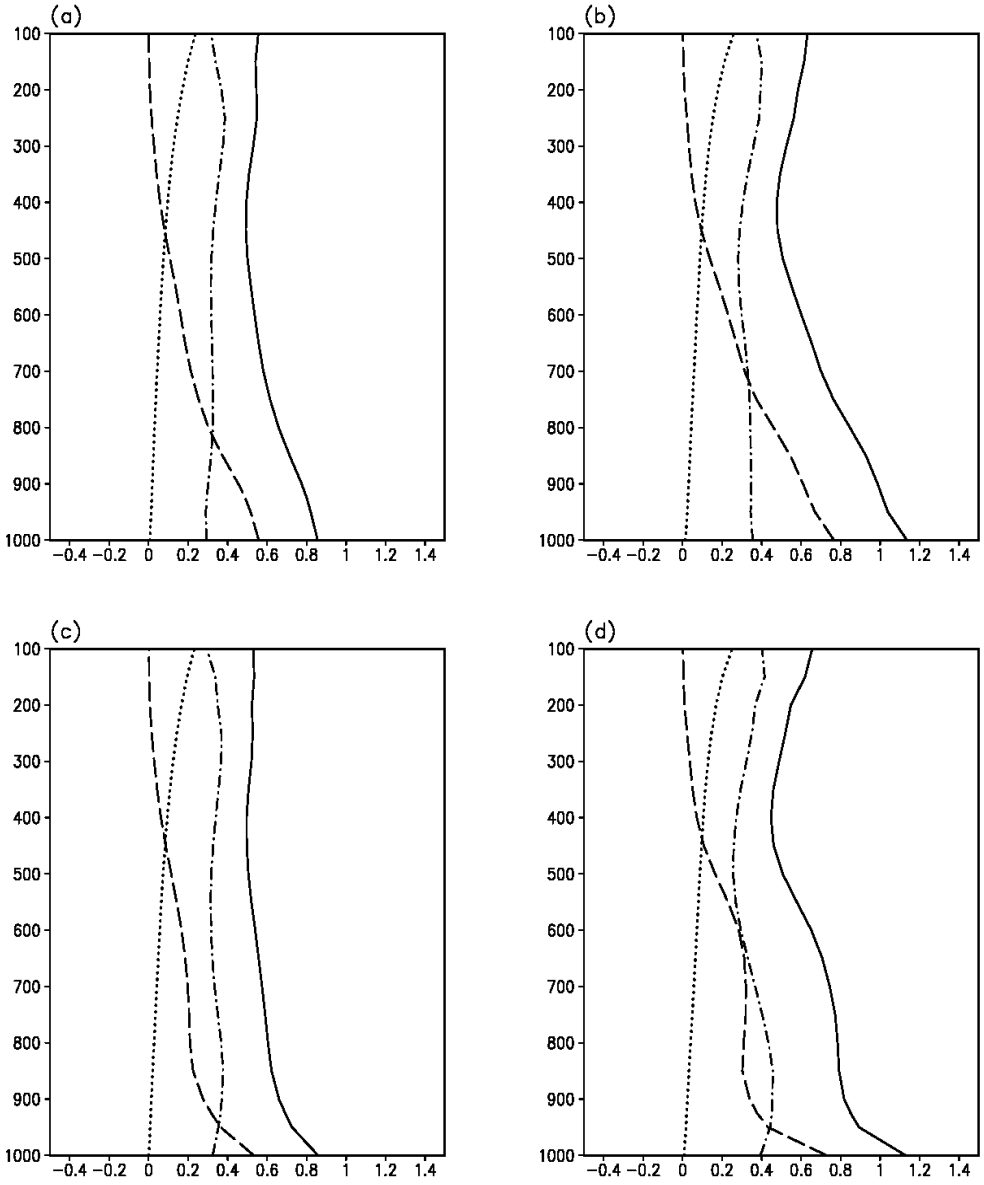

Figure 3.11 Anomalies of moist static energy (MSE) terms (Eq.3.3) over (a)-(b) the eastern and (c)-(d) central U.S. for (a), (c) AMJ and (b), (d) JAS. Sold lines denote the total MSE, dashed (dot-dash) lines denote the moisture (temperature) term, and dotted lines denote the geopotential term (units: 10^3 m^2 s^{-2}).

Figures 3.11c and d show the MSE anomalies averaged over the central (95°-105°W, 30°-35°N) U.S. for AMJ and JAS, respectively. In AMJ, increases in MSE anomalies between the surface and 500 hPa is mainly due to enhanced low-level moisture content (Fig. 3.11c), which is related to increases in southerly moisture transport due to the enhanced GPLLJ (Fig. 3.8a). The enhanced instability at low levels is consistent with the enhanced rising motion (Fig. 3.10c).

In JAS, the slope of MSE profile show that the instability of the atmosphere increases below 900 hPa, changes little between the 950 hPa and 700 hPa, and increases between 700 hPa and 500 hPa. Above 500 hPa, the atmosphere again is relatively stable (Fig. 3.11d). Below 950 hPa, changes of the MSE profile is dominated by the increases of moisture content, which are associated with enhanced southerly moisture transport by the GPLLJ (Fig. 3.8b). While changes in temperature profile tend to destabilize the atmosphere between 850 hPa and 500 hPa, the enhanced stability related to the high moisture content at 700 hPa partially counteracts this effect, and the atmosphere is relatively stable between the 950 hPa and 700 hPa. At higher levels between 400 hPa and 100 hPa, despite the decrease in moisture content, the atmosphere is relatively stable due to a larger temperature anomaly at 150 hPa and a smaller temperature anomaly at 500 hPa.

In short, large-scale circulation changes are consistent with the precipitation changes. Westward extension of the North Atlantic subtropical high and the formation of the anomalous high over the eastern Pacific and Gulf of the Mexico changes moisture transport onto the U.S. and Mexico. Both the variations in low-level moisture content and the temperature profile associated with circulation changes modify the vertical stability of the atmosphere. Over the eastern U.S., deep convection develops in AMJ due to enhanced moisture content, while in JAS changes in vertical temperature profile discourages deep convection.

b. Surface temperature changes

Figure 3.12 shows temperature anomalies for the shutdown minus control run (solid lines) and slowdown minus the control run (dashed lines) in different regions over the U.S. and Mexico. In both shutdown and slowdown simulations, the surface skin temperature increases, suggesting the dominant influence of global warming. In the shutdown simulation, over the north central U.S., the temperate anomaly is about 3 K in April, increase from May through August, with a maximum of about 7.5 K in August, then decreases to 6.5 K (Fig. 3.12a). In the south central U.S., positive temperature anomalies have a minimum of 3.4 K in April and a maximum of 5.6 K in September (Fig. 3.12b).

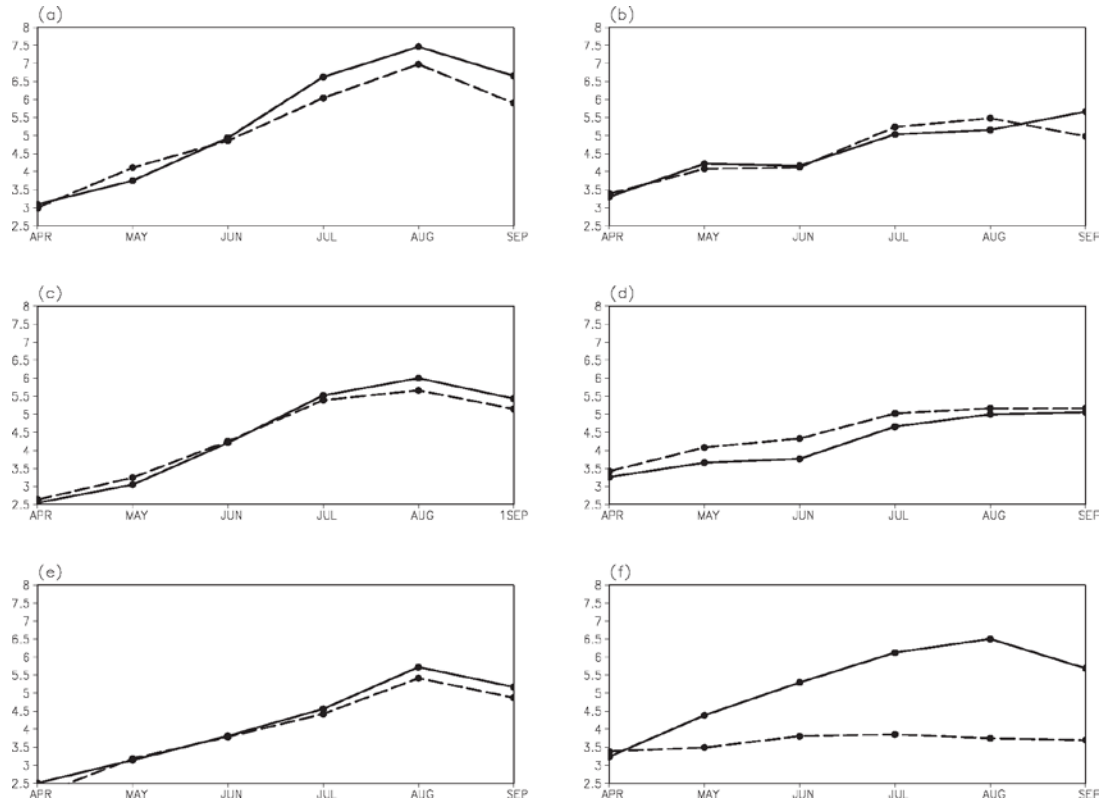

Figure 3.12 Anomalies of surface skin temperature (K) for the shutdown minus control simulations (solid lines) and for the slowdown minus the control simulations (dashed lines) for (a) the north central U.S., (b) the south central U.S., (c) the northwestern U.S., (d) the southwestern U.S., (e) the eastern U.S., and (f) the eastern Mexico.

Over the northwestern U.S., the temperature anomaly has a seasonal cycle similar to that in the north central U.S., with a maximum of 6 K in August and a minimum of 2.5 K in April (Fig. 3.12c). Over the southwestern U.S., anomalous temperature maximum of about 5 K also occurs in September (Fig. 3.12d).

Surface temperature anomalies also have maxima of about 5.5 K and 6.5 K in August over the eastern U.S. (Fig. 3.12e) and the eastern Mexico (Fig. 3.12f), respectively.

Considering the prescribed SST pattern, the slowdown simulation is not exactly comparable with the shutdown, in which the warming signal of SST is represented by uniform 2.5 K warming. Here the slowdown simulation is used to represent the signal of global warming modified by the slowdown of the AMOC, and the comparison between the two is concentrated on the seasonal cycle changes instead of quantifying the differences. Figs. 3.12a, c, and e suggest that in the north central, northwestern and eastern U.S., in early spring, e.g. May, the cooling effect associated with the AMOC shutdown tends to counteract the warming signal, while in the later summer, the nonlinear combination of the two forcing results in a warming signal. Over the southwest U.S., the global warming signal is weakened by the cooling effect of the AMOC shutdown (Fig. 3.12d), while over the eastern Mexico, the combined forcing leads to a much stronger warming (Fig. 3.12f). The situation is more complicated over the south central U.S. (Fig. 3.12b). While the warming signal is weakened by the AMOC cooling effect during July and August, in May and September, the combined forcing tends to magnify the warming signal.

Examination of the surface heat budgets in JAS reveals that warming over the central and northwestern U.S. is mainly due to decreases in latent cooling, which is associated with decreases in evaporation (Fig. 3.6d). Over the eastern U.S. the enhanced surface heating is associated with increases in net shortwave radiation and

downward longwave radiation, which are related to redistribution of cloud and moisture content (not shown).

In short, the greenhouse gas warming dominates the land surface temperature change for the first order. Variations in regional hydrological cycles and circulation further modify the temperatures through latent heat and cloud distribution.

c. Temperature extremes and dry spells

Differences of the monthly maximum temperature between the shutdown and control simulations reveal changes of extreme warm events. Figures 3.13a and b display the histogram of monthly maximum 2m temperature over the north central U.S. for AMJ and JAS, respectively. Daily mean temperature in each month is used to calculate the monthly maximum. As shown in Fig. 3.13a, in AMJ, range of monthly maximum temperature changes from 289-309K to 292-313 K. More extreme warm events above 308 K occur. In JAS (Fig. 3.13b), while the range of monthly maximum temperature shifts from 299-309 K to 305-315 K, the peak also changes from 306-307 K to 312-313 K.

Figures 3.13c and d display the histogram of monthly maximum temperature over the eastern U.S. for AMJ and JAS, respectively. In AMJ (Fig. 3.13c), occurrence of maximum temperature greater than 301K largely increases. Two peak occurrences of 294-295 K and 298-299 K shift to 296-297 K and 302-303 K. During JAS (Fig. 3.13d), the peak of 299-300 K shifts to 305-306 K in the shutdown simulation. The occurrence of warm events between 303 K and 310 K increases and decreases between 300 K and 302 K. Similar changes with more extreme warm events are found in other regions (not shown).

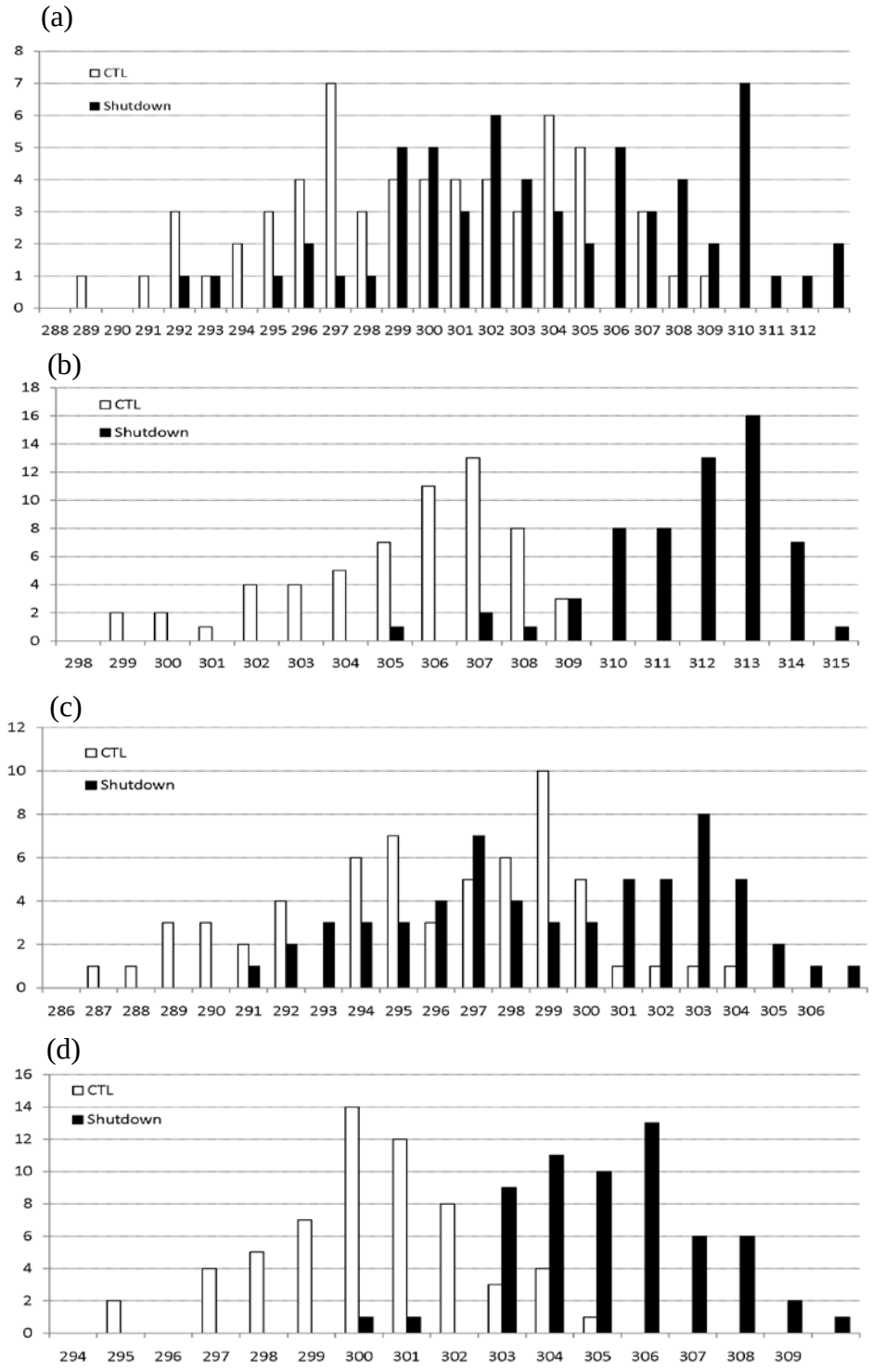

Figure 3.13 Histogram of monthly maximum 2m temperature (K) in the control (while) and shutdown (black) simulations over the (a)-(b) the north central and (c)-(d) eastern U.S. for (a), (c) AMJ and (b), (d) JAS. Y-axis denotes occurrence of the extreme temperatures within the ranges shown on the x-axis in the 20 years of the control or shutdown simulations.

Figure 3.14 shows the occurrence of dry spells in the control simulations and the anomalies (shutdown minus control) from April to September. Following Groisman and Knight (2008), a dry spell is defined as consecutive days with rainfall less than 1 mm day^{-1}. According to the length of the dry spells, 6 categories are defined, 1-10 days, e.g. equal and longer than 1 day but less than 10 days, 10-20 days, 20-30 days, 30-40 days, 40-50 days, and $\geq$ 50 days. Figure 3.14a shows the frequency of dry spells in each category in the control simulation from 1981-2000. The distribution is well validated in comparison with the NARR dry spell occurrence (not shown). For dry spell with the length of 1-10 days, the maximum occurrence is over the northeast U.S. For dry spell with the length of 10-20 and 20-30 days, maxima are over the southwestern Texas and northern Mexico, and over the western U.S. in Nevada, south California, Idaho and Utah. Most of dry spells with length of 30-50 days occur over the western U.S., while for dry spells longer than 50 days, the maximum is located along the west coast of the U.S. and Mexico.

In the shutdown simulation (Fig. 3.14b), dry spells with the length of 1-10 days decrease over the U.S. and Mexico, except over the south coast and the eastern Canada, where there are more dry spells. The occurrence of dry spells with the length of 10-20 days increases over most part of the U.S. and Mexico with a peak over the central U.S., and decreases over the south coast and the west coast in California and Nevada. Similar pattern is seen for the dry spells with the length of 20-30 days, but with a weaker magnitude. Comparing the changes of dry spells over the south coast among the categories of 1-10, 10-20, and 20-30 days suggest that decreases in the 20-30 dry spells is associated with increases in shorter dry spells of 1-10 days. This may be related to increasing occurrence of rainfall (Figs. 3.6a and b) which breaks the longer dry spells into shorter spells.

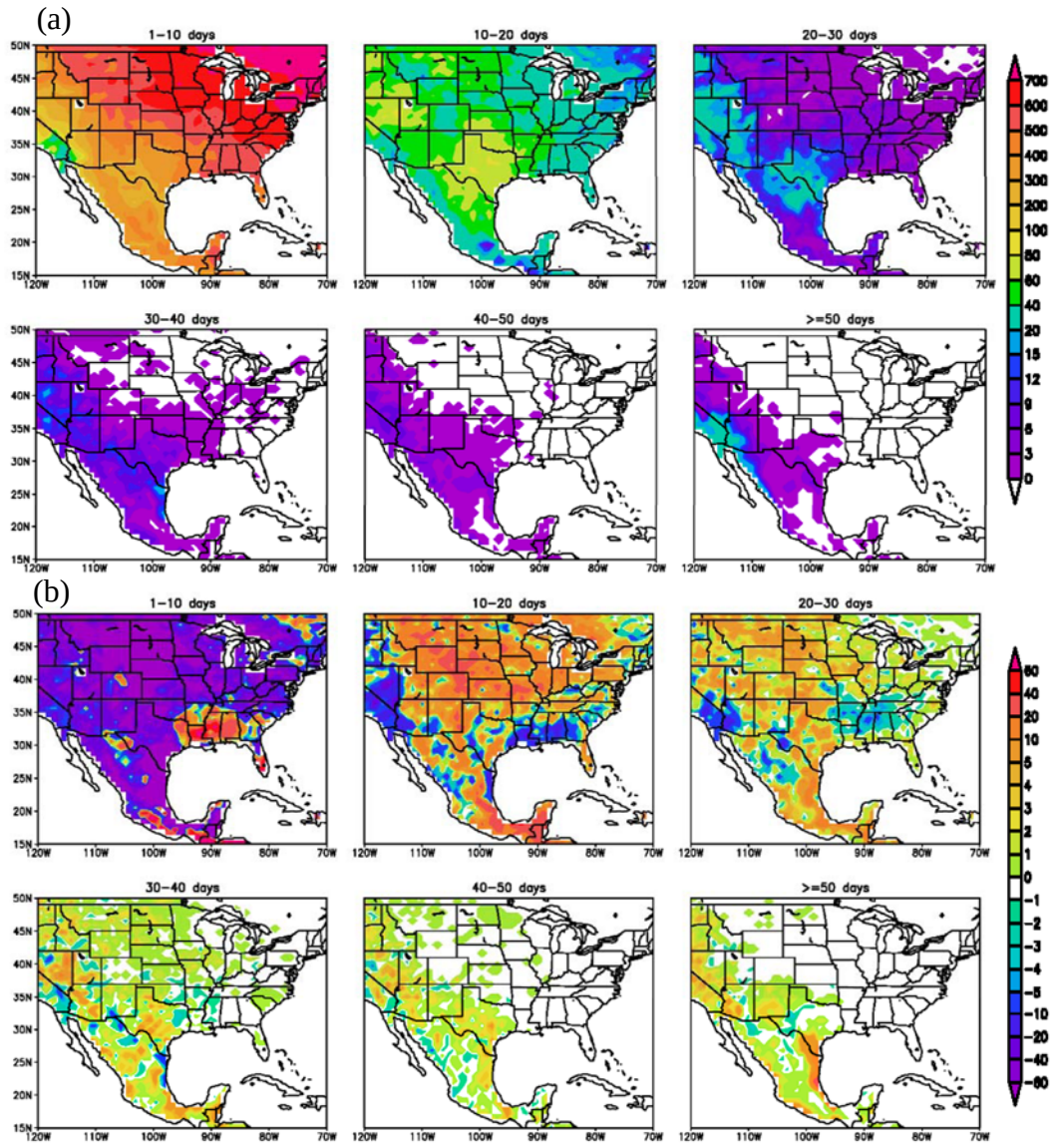

Figure 3.14 Number of dry spells (see definition in the text) with length of 1-10 days, 20-30 days, 30-40 days, 40-50 day and greater than 50 days in the (a) control simulation and (b) anomalies between the shutdown and control simulations from April to September.

Occurrence of dry spells with length greater than 30 days increases over the western and central U.S. Most of the states in the west of 85° W have at least one more dry spell with the length of 30-40 days in the 20 years. In Nevada, Arizona, Texas, and also Mexico, such dry spells occur 4 to 5 more times. In Oregon, Nevada, southern California, Utah, Arizona, Texas, and the eastern Mexico, 3-4 more dry spells with the length of 40-50 days occur. Dry spells with the length 50 day also increase in these regions. Increases of dry spells over the west coast and eastern Mexico is consistent with the decreases in the 10-30 days dry spells, suggesting that in those regions dry spells tend to become longer associated with changes of rainfall frequency.

In short, Figs. 3.13 and 3.14 demonstrate that under the scenario of AMOC shutdown and strong greenhouse gas warming, more extreme warm events and longer dry spells will occur over most of the U.S.

3.6 Conclusions

Both the paleoclimatic records and model simulations reveal that reorganization of the Atlantic meridional overturning circulation (AMOC) has far-reaching climate impacts over the Northern Hemisphere. Observations and model simulation also suggest that the strength of the AMOC is sensitive to the greenhouse gas concentration, and wakens in various extents (model dependent) with increasing CO_2. Although none of the IPCC AR4 model predicts a complete shutdown of the AMOC by the end of the 21st century under the SRES emission scenarios, the possibility cannot be excluded (IPCC AR4 2007). Model simulations suggest that while the climate responses, e.g., temperature and precipitation, to the AMOC shutdown are generally opposite to those caused by greenhouse gas warming, the two forcing may add nonlinearly and the total effects are regionally dependent (Vellinga

and Wood 2008). Here we study the climate response over the United States and Mexico to a hypothetical AMOC shutdown during the period of 2081-2100 through an atmosphere-only regional climate model (WRF). In the AMOC shutdown simulation, an idealized SSTA (Fig. 3.1) and boundary perturbations predicted by the AOGCMs for 2081-2100 are applied to the NCEP2 reanalysis (1981-2000) to drive the model, while the CO_2 concentration is fixed to the average value of 2081-2100 under the SRES A2 emission scenario.

WRF model predicts that precipitation decreases in most of the United States and Mexico from April to September, except over the eastern U.S. where rainfall increases in April, May, June, and September. Decreases in rainfall are most severe in August, with negative anomalies up to -40% over the central U.S. and -80% over the eastern Mexico.

Moisture budget analysis shows that precipitation variations are mainly due to changes in moisture convergence in Mexico, the eastern and western U.S. Decreases in evaporation contribute about one half to the precipitation anomalies over the southern central U.S. for AMJ and over the whole central U.S. for JAS, while increases in evaporation enhance rainfall over the east coast for JAS.

Moisture transport anomalies are examined and found to be consistent with precipitation and moisture convergence anomalies. In AMJ, enhanced southwesterly moisture transport brings more moisture from the Gulf of Mexico onto the eastern U.S. This is mainly due to enhanced southwesterly wind between the surface and 500 hPa, which is associated with the westward extension of the North Atlantic subtropical high. In JAS, this anomalous moisture flux is shallower due to the high-level easterly wind anomalies.

Over the central U.S., southerly moisture transport is enhanced from April to September due to a stronger Great Plains low-level jet (GPLLJ) associated with the

westward extension of the subtropical high. In JAS, anomalous southerly flux over the Rocky Mountains decreases the northward moisture transport. The moisture supply from the ocean onto Mexico and the U.S. is decreased by the anomalous anticyclonic moisture fluxes over the Gulf of Mexico.

Moisture transport anomalies are dominated by the variations of large-scale circulation. One of the most prominent features in the shutdown simulation is the strengthening and extension of the North Atlantic subtropical high, which enhances the southeastward geopotential height gradients over the northwest Gulf of Mexico and the eastern U.S. in AMJ and over the central U.S. in JAS. Another important feature is the formation of an anomalous high between 15°N and 30°N over the eastern Pacific and the Gulf of Mexico due to variations in land-sea surface temperature gradient. In JAS, it extends from the surface to about 400 hPa, decreasing the moisture transport onto the continent.

Examination of the MSE and vertical wind anomalies found that in AMJ, enhanced moisture content over the central and eastern U.S. decreases the stability of the atmosphere. Anomalous rising motion over the eastern U.S. enhances the moisture convergence, and precipitation increases. In JAS, a relative stable layer occurs between 400 hPa and 100 hPa associated with a larger temperature anomaly at 200-100 hPa and a smaller temperature anomaly at 500-400 hPa. The stability of the vertical column over the central and eastern U.S. increases. Deep convection is discouraged, and precipitation decreases.

Greenhouse gas warming dominates temperature variations over land. Variations in regional hydrological cycles and circulation further modify the temperatures through latent heat and cloud distribution. In August, temperature increases up to +7.5 K over the north central U.S., +6 K over the western U.S., +5.7 K over the eastern U.S., and +6.5 K over the eastern Mexico. Over the south central

(+5.6 K) and western (+5 K) U.S., the maximum increase occurs in September. More extreme warm events occur.

Dry spells tend to be shorter over the south coast of the U.S. Over the central U.S. dry spells with length of 10-30 days increase, while over the western U.S. and the eastern Mexico, dry spells longer than 30 days increase.

REFERENCES

Alley, R. B., and A. M. Agustsdottir, 2005: The 8k event: cause and consequences of a major Holocene abrupt climate changes. *Quaternary Science Reviews*, **24**, 1123-1149.

Barreiro, M., A. Fedorov, R. Pacanowski, and S. G. Philander, 2008: Abrupt climate changes: how freshening of the Northern Atlantic affects the thermohaline and wind-driven oceanic circulations. *Annu. Rev. Earth Planet. Sci.*, **36**, 33–58.

Broecker, W. S., 2003: Does the trigger for abrupt climate changes reside in the ocean or in the atmosphere? *Science*, **300**, 1519-1522.

Bryden, H. L., H. R. Longworth, and S. A. Cunningham, 2005: Slowing of the Atlantic meridional overturing circulation at 25°N. *Nature*, **438**, 655-657. doi:10.1038/nature04385.

Chang, P., R. zhang, W. Hazeleger, C. Wen, X, Wan, L. Ji, R. J. Haarsma, W.-P. Breugem, and H. Seidel, 2008: Oceanic link between abrupt changes in the North Atlantic Ocean and the African monsoon. *Nature Geoscience*, **1**, 444-448.

Chen, F., and J. Dudhia, 2001: Coupling an advanced land-surface/ hydrology model with the Penn State/ NCAR MM5 modeling system. Part I: Model description and implementation. *Mon. Wea. Rev.*, **129**, 569–585.

Chen, S. H,, W. Y. Sun, 2002: A one-dimensional time dependent cloud model. *J Meteorol Soc Jpn.*, **80**, 99–118.

Clark, P. U., S. J. Marshall, G. K. C. Clarke, S. W. Hostetler, J. M. Licciardi, and J, T. Teller, 2001: Freshwater forcing of abrupt climate change during the last glaciations. *Science*, **293**, 283-287.

Clarke, G., D. Leverington, J. Teller, and A. Dyke, 2003: Superlakes, megafloods, and abrupt climate change. *Science*, **301**, 922-923.

Cook, K. H., E. K. Vizy, Z. S. Launer, and C. M. Patricola, 2008: Springtime intensification of the Great Plains low-level jet and Midwest precipitation in GCM simulations in the twenty-first century. *J. Climate*, **21**, 6321-6340.

Curry, R. and C. Mauritzen, 2005: Dilution of the northern North Atlantic Ocean in recent decades. *Science*, **308**, 1772-1774.

Davis, C. A., K. W. Wanning, R. E. Carbone, S. B. Trier, and J. Tuttle, 2003: Coherence of warm-season continental rainfall in numerical weather prediction models. *Mon. Wea. Rev.*, 131, 2667-2679.

Dickson, R. R., R. Curry, and I. Yashayaev, 2003: Recent changes in the North Atlantic. *Phil. Trans. R. Soc. Lond.* A, **361**, 1817-1934.

Dixon, K. W., T. Delworth, M. Spelman, and R. J. Stouffer, 1999: The influence of transient surface fluxes on North Atlantic overturning in a coupled GCM climate change experiment. *Geophys. Res. Lett.*, **26,** 2749–2752.

Dudhia, J., 1989: Numerical study of convection observed during the winter monsoon experiment using a mesoscale two-dimensional model, *J. Atmos. Sci.*, **46**, 3077–3107.

EPICA community members, 2004: Eight glacial cycles from an Antarctic ice core. *Nature*, **429**, 623–628.

Ganachaud, A., and C. Wunsch, 2000: The oceanic meridional overturning circulation, mixing, bottom water formation, and heat transport. *Nature,* **408,** 453–457.

Ganachaud, A., and C. Wunsch, 2003: Large-scale ocean hear and freshwater transports during the World Ocean Circulation Experiment. *J. Climate*, **16**, 696-705.

Gregory, J. M., K. W. Dixon, R. J. Stouffer, A. J. Weaver, E. Driesschaert, M. Eby, T. Fichefet, H. Hasumi, A. Hu, J. H. Jungclaus, I. V. Kamenkovich, A. Levermann, M. Montoya, S. Murakami, S. Nawrath, A. Oka, A. P. Sokolov, and R. B. Thorpe,

2995: A model intercomparision of changes in the Atlantic thermohaline circulation in response to increasing atmospheric CO_2 concentration. *Geophys. Res. Lett.*, **32**, L12703, doi:10.1029/ 2005GL023209.

Groisman, P. Y., and R. W. Knight, 2008: Prolonged dry episodes over the conterminous United States: New tendencies emerging during the last 40 years. *J. Climate*, **21**, 1850-1862.

IPCC, 2007: Climate Change 2007: The Physical Science Basis. Contribution of Working Group I to the Fourth Assessment Report of the Intergovernmental Panel on Climate Change [Solomon, S., D. Qin, M. Manning, Z. Chen, M. Marquis, K.B. Averyt, M. Tignor and H.L. Miller (eds.)]. Cambridge University Press, Cambridge, United Kingdom and New York, NY, USA, 996 pp.

Janjic, Z. I., 1990: The step-mountain coordinate: physical package, *Mon. Wea. Rev.*, **118**, 1429–1443.

Janjic, Z. I., 1994: The step-mountain Eta coordinate model: further developments of the convection, viscous sublayer and turbulence closure schemes. Mon Weather Rev 122:927–945.

Janjic, Z. I., 1996: The surface layer in the NCEP Eta Model, *Eleventh Conference on Numerical Weather Prediction*, Norfolk, VA, 19–23 August; Amer. Meteor. Soc., Boston, MA, 354–355.

Janjic, Z. I., 2002: Nonsingular Implementation of the Mellor–Yamada Level 2.5 Scheme in the NCEP Meso model, *NCEP Office Note*, **No. 437**, 61 pp.

Jacob, D., H. Goettel, J, Jungclaus, M. Muskulus, R. Podzun, and J. Marotzke, 2005: Slowdown of the thermohaline circulation causes enhanced maritime climate influence and snow cover over the Europe. *Geophys. Res. Lett.*, **32**, L21711, doi:10.1029/2005GL023286.

Kain, J. S., and J. M. Fritsch, 1990: A one-dimensional entraining/ detraining plume

model and its application in convective parameterization, *J. Atmos. Sci.*, **47**, 2784–2802.

Kain, J. S., and J. M. Fritsch, 1993: Convective parameterization for mesoscale models: The Kain-Fritcsh scheme, *The representation of cumulus convection in numerical models*, K. A. Emanuel and D.J. Raymond, Eds., *Amer. Meteor. Soc.*, 246 pp.

Kain, J. S., 2004: The Kain-Fritsch convective parameterization: An update. *J. Appl. Meteor.*, **43**, 170–181.

Kanamitsu, M., W. Ebisuzaki, J. Woollen, S. Yang, J. Hnilo, M. Fiorino, and G. Potter, 2002: NCEP-DOE AMIP-II reanalysis. *Bull. Amer. Meteorol. Soc.*, **83**, 1631-1643.

Kerr, R. A., 2005: The Atlantic conveyor may have slowed, but don't panic yet. *Science*, **310,** 1403–1405.

Latif, M., C. Boning, J. Willebrand, A. Biastoch, J. Dengg, N. Keenlyside, and U. Schweckendiek, 2006: Is the thermohaline circulation change? *J. Climate*, **18**, 4631-4637.

Laurian, A., S. S. Drijfhout, W. Hazeleger, and R. van Dorland, 2009: Global surface cooling: the atmospheric fast feedback response to a collapse of the thermohaline circulation. *Geophys. Res. Lett.*, **36**, L20708, doi:10.1029/2009GL040938.

Lee, M., S. D. Schubert, M. J. Suarez, I. M. Held, N. Lau, J. J. Ploshay, A. Kumar, H. Kim, and J. E. Schemm, 2007: An analysis of the warm-season diurnal cycle over the continental United Sates and northern Mexico in general circulation models. *J. Hydrometeor.*, **8**, 344-365.

Liang, X.-Z., L. Li, A. Dai, and K. E. Kunkel (2004), Regional climate model simulation of summer precipitation diurnal cycle over the Unite States, *Geophys. Res. Lett.*, **31**, L24208, doi:10.1029/ 2004GL021054.

Lin, Y. L., R. D. Farley, H. D. Orville, 1983: Bulk parameterization of the snow field in a cloud model. *J. Appl. Meteorl.*, **22**, 1065–1092.

Manabe, S., and R. J. Stouffer, 1999: The role of thermohaline circulation in climate. *Tellus*, **51A-B**, 91-109.

Mellor, G. L., and T. Yamada, 1982: Development of a turbulence closure model for geophysical fluid problems. *Rev. Geophys. Space Phys.*, **20**, 851–875.

Mesinger, F., and Coauthors, 2006: North American regional reanalysis. *Bull. Amer. Meteor. Soc.*, **87,** 343–360.

Mlawer, E. J., S. J. Taubman, P. D. Brown, M. J. Iacono, and S. A. Clough, 1997: Radiative transfer for inhomogeneous atmosphere: RRTM, a validated correlated-k model for the longwave. *J. Geophys. Res.*, **102 (D14)**, 16663–16682.

Monin AS, Obukhov AM (1954) Basic laws of turbulent mixing in the surface layer of the atmosphere. *Contrib Geophys Inst Acad Sci*, **USSR 151**, 163–187 (in Russian).

Patricola, C. M., and K. H. Cook, 2010: Northern African climate at the end of the twenty-first century: an integrated application of regional and global climate models. *Clim. Dyn.*, **35**,193-212.

Petit, J. R., J. Jouzel, D. Raynaud, N. Barkov, J. M. Barnola, I. Basile, M. Bender, J. Chapellaz, M. Davis M, G. Delaygue, M. Delmotte, V. Kotlyakov, M. Legrand, VYLipenkov, C. Lorius, L. Pepin, C. Ritz, E. Saltzman, and M. Stievenard, 1999: Climate and atmospheric history of the past 420,000 years from the Vostok ice core, Antarctica. *Nature*, **399**, 429–436

Roche, D. M., A. P. Wiersma, and H. Renssen, 2010: A systematic study of the impact of freshwater pulses with respect to different geographical locations. *Clim. Dyn.*, **34**, 997-1013.

Renssen, H., H. Goosse, T. Fichefet, and J. M Campin, 2001a: The 8.2 kyr BP event

simulated by a global atmosphere-sea-ice-ocean model. *Geophys. Res. Lett.*, **28**, 1567–1570.

Renssen, H., R.F.B. Isarin, D. Jacob, R. Podzun, and J. Vandenberghe, 2001b: Simulation of the Younger Dryas climate in Europe using a regional climate model nested in an AGCM: preliminary results. *Global and Planetary Change*, **30**, 41–57.

Renssen, H., H. Goosse, and T. Fichefet, 2002: Modeling the effect of freshwater pulses on the early Holocene climate: the influence of high-frequency climate variability. *Paleoceanography* , **17**, Art. No. 1020.

Rutledge SA, Hobbs PV (1984) The mesoscale and microscale structure and organization of clouds and precipitation in midlatitude cyclones. XII: a diagnostic modeling study of precipitation development in narrow cold-frontal rainbands. J Atmos Sci 41(20):2949–2972.

Schmittner, A., M. Latif, and B. Schneider, 2005: Model projections of the North Atlantic thermohaline circulation for the 21st century assessed by observations, *Geophys. Res. Lett.*, 32, L23710, doi:10.1029/ 2005GL024368.

Smirnova, T. G., J. M. Brown, S.G. Benjamin, 1997: Performance of different soil model configurations in simulating ground surface temperature and surface fluxes. *Mon Weather Rev.*, **125**, 1870– 1884. doi:10.1175/1520-0493.

Smirnova, T.G., J. M. Brown, S .G. Benjamin, D. Kim, 2000: Parameterization of cold season processes in the MAPS land-surface scheme. *J Geophys Res***, 105**, 4077–4086. doi:10.1029/ 1999JD901047.

Skamarock, W. C., J. B. Klemp, J. Dudhia, D. O. Gill, D. M. Barker, M. G. Duda, X. Huang, W. Wang, and J. G. Powers, 2008: A Description of the Advanced Research WRF version 3, NCAR Tech. Note, NCAR/TN-475+STR, 125 pp.

Stammer, D., and Coauthors, 2003: Volume, heat, and freshwater transports of the

global ocean circulation 1993–2000, estimated from a general circulation model constrained by World Ocean Circulation Experiment (WOCE) data. *J. Geophys. Res.,* **108,** 3007, doi:10.1029/2001JC001115.

Stouffer, R. J., J. Yin, J. M. Gregory, K. W. Dixon, M. J. Spelman, W. Hurlin, A. J. Weaver, M. eby, G. M. Flato, H. Hasumi, A. Hu, J. H, Jungclaus, I. V. Kamenkovich, A. Levermann, M. Montoya, S. Murakami, S. Nawarath, A. Oka, W. R. Peltier, D. Y. Robitaille, A. Sokolov, G. Vettoretti, and S. L. Weber, 2006: Investigating the causes of the response of the thermohaline circulation to past and future climate changes. *J. Climate,* 19, 1365-1387.

Tao, W. K., J. Simpson, M. McCumber, 1989: An ice-water saturation adjustment. *Mon Weather Rev*., **117**, 231–235.

Thorpe, R. B., J. M. Gregory, T. C. Johns, R. A. Wood, and J. F. B. Mitchell, 2001: Mechanisms determining the Atlantic thermohaline circulation response to greenhouse gas forcing in a non-flux-adjusted coupled climate model. *J. Climate,* **14,** 3102–3116.

Uppala, S. M., et al., 2005: The ERA-40 re-analysis. *Q. J. R. Meteorol. Soc.*, **131**, 2961–3012, doi:10.1256/qj.04.176.

Vellinga, M., and R. A. Wood, 2002: Global climatic impacts of a collapse of the Atlantic thermohaline circulation. *Climate Change*, **54**, 251-267.

Vellinga, M., and R. A. Wood, 2008: Impacts of the thermohaline circulation shutdown in the twenty-first century. *Climatic Change*, **91**, 43-63.

Wood, R. A., A. B. Keen, J. F. B. Mitchell, and J. M. Gregory, 1999: Changing spatial structure of the thermohaline circulation in response to atmospheric CO2 forcing in a climate model. *Nature*, **399,** 572–575.